UNIVERSIDADE
BEIRA INTERIOR

Piezoresistive Sensing for Structural Health Monitoring: A Practical Application in Adhesive Joints

(Versão final após defesa)

Beatriz Varela Santos

Dissertação para obtenção do Grau de Mestre em
Engenharia Aeronáutica
(mestrado integrado)

Orientador: Professor Doutor Abílio Manuel Pereira da Silva
Co-orientador: Professor Doutor João Pedro Nunes Pereira

Covilhã, março de 2024

Declaração de Integridade

Eu, Beatriz Varela Santos, que abaixo assino, estudante com o número de inscrição a41863 de/o Mestrado Integrado em Engenharia Aeronáutica da Faculdade de Engenharia, declaro ter desenvolvido o presente trabalho e elaborado o presente texto em total consonância com o **Código de Integridades da Universidade da Beira Interior**.

Mais concretamente afirmo não ter incorrido em qualquer das variedades de Fraude Académica, e que aqui declaro conhecer, que em particular atendi à exigida referenciação de frases, extratos, imagens e outras formas de trabalho intelectual, e assumindo assim na íntegra as responsabilidades da autoria.

Universidade da Beira Interior, Covilhã 05/03/2024

(assinatura conforme Cartão de Cidadão ou preferencialmente
assinatura digital no documento original se naquele mesmo formato)

Assinado por: **Beatriz Varela Santos**
Num. de Identificação: 15982438
Data: 2024.03.06 15:23:08+00'00'

CHAVE MÓVEL

Acknowledgements

This dissertation is dedicated to everyone who helped me finish it, directly or indirectly, for which I will always be thankful.

My sincere appreciation goes to my advisors, Professor Abílio Silva and Professor João Pereira, for their unwavering support, knowledge, and encouragement over this dissertation process. Their commitment and expertise have greatly influenced how my research has turned out.

I also want to express my gratitude to the departments of Aerospace Sciences and Electromechanical Engineering for all of their help and resources, which were essential to my academic achievement. My deepest gratitude is extended to the Centre for Mechanical and Aerospace Sciences and Technologies (C-MAST), which has supported me with services and given me laboratory supplies, equipment, and raw materials. Their assistance was crucial to the accomplishment of this study.

I would especially like to thank Paulo Santos and João Parente for always being willing to assist me and for satisfying my curiosity in all topics. This study journey was enhanced by their assistance and openness to share their experience and insights. I also like to thank my master's classmates for their support of one another. Your friendship and the experiences you have shared have been priceless.

I am very appreciative to my family for giving me the chance to continue my education and for being there for me during these five challenging years with constant support and encouragement.

Finally, I would like to express my sincere gratitude to my friends who helped me along the way, encouraged me, and respectfully accepted my complaints about any difficulties I encountered. They know who they are, and I appreciate their companionship and empathy.

Without the combined encouragement and support of these people and organizations, this dissertation would not have been possible. I sincerely appreciate the contributions they have made to the realization of this research.

Resumo

Os compósitos desempenham um papel significativo em diversas indústrias. No entanto, o uso de sistemas mecânicos como parafusos e rebites introduz danos que podem comprometer a saúde estrutural do compósito. Como resultado, a união adesiva é cada vez mais uma técnica viável para a montagem de estruturas em compósito. Apesar de oferecer vantagens, como a redução de massa e uma distribuição uniforme das forças, a viabilidade das uniões adesivas ainda não está totalmente estabelecida e é crucial melhorar a capacidade de monitorização das estruturas onde a adesão é utilizada.

Este estudo pretende contribuir para o avanço no conhecimento com a proposta de desenvolver adesivos multifuncionais, ao incorporar nanotubos de carbono (CNTs) em nanocompósitos à base de epóxi, melhorando simultaneamente a sua resistência mecânica e a resposta sensorial piezoresistiva. Ao longo deste trabalho aplicaram-se os adesivos multifuncionais em cenários práticos de monitorização da saúde estrutural (MSE), especialmente em juntas simples. A pesquisa envolve o estudo eletromecânico de amostras com duas percentagens de CNT ($0,25$ wt.% e $0,50$ wt.%) numa matriz de epóxi em uniões adesivas de junta sobreposta simples.

Os resultados experimentais revelam que adesivos com $0,50$ wt.% de CNTs apresentam propriedades mecânicas superiores e capacidades sensoriais melhores durante os testes de flexão, demonstrando a sensibilidade piezoresistiva de deformação mais alta de $5,2$. No entanto, para juntas sobrepostas simples, a sensibilidade é mais reduzida, apresentando uma sensibilidade de deformação de $0,77$. Em testes de tração para as juntas simples, a sensibilidade de deformação é de $1,27$, evidenciando que diferentes carregamentos e danos resultam em diferentes medições piezoresistivas.

Com as sensibilidades referidas, foi possível monotorizar diferentes gamas de deformação e também detetar carregamentos cíclicos até 100 ciclos, tendo-se verificado que a histerese é quase inexistente. A funcionalização dos adesivos mostrou ser eficaz no desenvolvimento de materiais multifuncionais com capacidades mecânicas e sensoriais piezoresistivas.

Palavras-chave

Monitorização da saúde estrutural, deteção piezoresistiva, juntas de sobreposição simples, material multifuncional, adesivos estruturais, nanotubos de carbono

Abstract

Composites play a significant role in various industries. However, the use of mechanical systems such as bolts and rivets introduces damages that can compromise the structural health of the composite. As a result, adhesive bonding is increasingly becoming a viable technique for assembling composite structures. Despite offering advantages, such as mass reduction and uniform distribution of forces, the feasibility of adhesive joints is not fully established, and it is crucial to improve the monitoring capability of structures where adhesion is used.

This study aims to contribute to advancing knowledge by suggesting the development of multifunctional adhesives, incorporating carbon nanotubes (CNTs) into epoxy-based nanocomposites, simultaneously enhancing their mechanical strength and piezoresistive sensory response. Throughout this work, multifunctional adhesives were applied in practical scenarios of structural health monitoring (SHM), especially in single-lap joints. The research involves the electromechanical study of bulk adhesive samples with varied percentages of CNT loading (0.25 wt.% and 0.50 wt.%) in an epoxy matrix and adhesive joints of single-lap configuration.

Experimental results reveal that adhesives with 0.50 wt.% of CNTs exhibit superior mechanical properties and better sensing capabilities during bending tests, demonstrating a higher gauge factor (GF) of 5.2. However, for single-lap joints, the sensitivity is slightly reduced, with a GF of 0.77. In tensile tests for single-lap joints, the GF is 1.27, highlighting that different loadings and damages result in distinct piezoresistive measurements.

With the mentioned GF it was possible to monitor different ranges of deformation and detect cyclic loadings of up to 100 cycles, with almost negligible hysteresis. The functionalization of adhesives has proved its effectiveness in developing multifunctional materials with mechanical and piezoresistive sensory capabilities.

Keywords

Structural health monitoring, piezoresistive sensing, single-lap joints, multifunctional materials, structural adhesives, carbon nanotubes

Contents

List of Figures

List of Tables

Nomenclature

Acronyms and abbreviations

AC	Alternating Current
BET	Brunauer-Emmett-Teller method
CCA	Co-Curing with Adhesive
CCN	Co-Curing without Adhesive
CCVD	Catalytic Chemical Vapor Deposition
CFRP	Carbon Fiber Reinforced Polymer
CNH	Carbon Nanohorns
CNTs	Carbon Nanotubes
COB	Co-Bonding
CVD	Chemical Vapor Deposition
DC	Direct Current
DLJ	Double-Lap Joint
DWCNTs	Double-Walled Carbon Nanotubes
EPT	Electrical Percolation Threshold
FEA	Finite Element Analysis
FRP	Fiber Reinforced Polymer
GF	Gauge Factor
GNP	Graphene Nanoplatelets
HRTEM	High Resolution Transmission Electron Microscopy
ICP-MS	Inductively Coupled Plasma Mass Spectrometry
JLJ	Joggle Lap Joint
LSJ	L-Section Joint
MWCNTs	Multi-Walled Carbon Nanotubes
NDI	Nondestructive Inpection
PLA	Polylactic Acid

PVDF	Polyvinylidenefluoride
SDGs	Sustainable Development Goals
SEB	Secondary Bonding
SHM	Structural Health Monitoring
SLJ	Single-Lap Joint
SWCNTs	Single-Walled Carbon Nanotubes
TEM	Transmission Electron Microscopy
TGA	Thermogravimetric Analysis

Latin Symbols

$\bar{h}$	Average sample thickness	mm
ΔR	Normalized change of electrical resistance	–
Δt	Time interval for load/unload condition in bending	s
A_0	Adhesive area	mm^2
b	Sample width	mm
d_i	Relative distance between consecutive CNTs	–
E_f	Flexural modulus	MPa
F	Flexural force	N
F_f	Volume fraction of the filler	–
F_m	Volume fraction of the matrix	–
L	Overlap length	mm
l	Sample length	mm
L_0	Original distance between gage marks	mm
L_s	Span length	mm
L_t	Distance between gage marks at any time	mm
L_u	Distance between gage marks at moment of rupture	mm
M	Bending moment	$\mathrm{N} \cdot \mathrm{m}$
P	Tensile force	N

R	Electrical resistance	kΩ
R^2	Coefficient of determination	–
R^C	Contact resistance	kΩ
R^T	Tunneling resistance	kΩ
R^{CNT}	Intrinsic CNT resistance	kΩ
R_0	Electrical resistance in resting state	kΩ
s	Sample deflection	mm
t	Critical exponent relating to the dimensionality of conductive networks	–
T_g	Glass transition temperature	°C

Greek Symbols

ϕ	Filler volume fraction	%
ϕ_c	Filler volume fraction at percolation threshold	%
σ	Electrical conductivity of the nanocomposite	S/m
σ_c	Compression stress	MPa
σ_f	Flexural stress	MPa
σ_m	Electrical conductivity of the matrix	S/m
σ_r	Electrical conductivity of the filler	S/m
σ_t	Tensile stress	MPa
σ_{f1}	Flexural stress for a deflection s_1	MPa
σ_{f2}	Flexural stress at a deflection s_2	MPa
τ	Shear stress	MPa
ε	Mechanical strain	mm/mm
ε_f	Flexural strain	mm/mm
ε_t	Tensile strain	mm/mm
ε_ν	Transverse strain	mm/mm
ε_{f1}	Flexural strain for a deflection s_1	mm/mm
ε_{f2}	Flexural strain for a deflection s_2	mm/mm

Chemichal Symbols

$\gamma - Al_2O_3$	Gamma crystaline phase of alumina
CO_2	Carbon Dioxide
C_2H_6O	Ethanol
C_3H_6O	Acetone
CH_4	Methane
COOH	Carboxylate
HNO_3	Nitric acid
NH_2	Amine
SDS	Sodium dodecyl sulfate

Chapter 1

Introduction

This Chapter provides an overview of structural adhesives and their application to bonded joints within aerospace field. With adhesives gaining increasing importance and finding versatile applications in various engineering contexts, they present a compelling alternative to mechanical assembly methods such as rivets and bolts. Multifunctional adhesives possess unique characteristics, including geometric, chemical, electrical, and thermal properties, which allow a wide range of functionalities in engineering applications. In this particular case, the focus will be on reviewing the electrical properties of adhesives for setting up multifunctional materials with sensing capability. The motivation behind this study, as well as its objectives and the structure of this dissertation, will be discussed in detail in the following sections.

1.1 Motivation

In a world increasingly concerned with climate change and the energy crises, efforts are being made to find cleaner and safer practices to reduce these problems. According to the Department of Economic and Social Affairs of the United Nations, CO_2 emissions increased 6 % in 2021, reaching the highest level ever (UN- (2022)). Sustainable Development Goals (SDGs), adopted by all United Nations Member States in 2015, aim to take action in different fields to address issues like climate change. One area of focus is the aviation industry, which is responsible for 2.1 % of global carbon emissions, according to Yusaf et al. (2022). For this reason, the aerospace sector is actively working to find cleaner methods of operation, such as developing new materials and manufacturing techniques that reduce aircraft mass, thereby facilitating a reduction of carbon emissions.

Using composites instead of traditional materials offers a promising solution in the aerospace industry, as they can reduce costs, mass, and fuel consumption while still providing exceptional mechanical performance for aircraft structures. Composite materials made of glass and carbon fibers exhibit high specific strength, fatigue resistance, high modulus, and corrosion resistance, properties desirable in aerospace industry (Giurgiutiu (2016); Irfan et al. (2021)). Consequently, a substantial portion of the principal structures in airplanes now integrate composite materials.

For instance, major aircraft manufacturers such as Boeing and Airbus have increasingly adopted composites in their aircraft designs. More than 50 % of structural components in modern aircraft like the Boeing 787 and Airbus 350 XWB are now built using composite materials, as highlighted by Sante (2015). Figure 1.1 visually illustrates this trend, showcasing how these manufacturers are progressively replacing traditional materials with composites.

Figure 1.1a showcases different sections of the Boeing 787, composed of fiberglass, carbon laminate composite, and carbon sandwich composite, constituting 50 % of the overall structure. This value surpasses the 12 % seen in the Boeing 777 model. Additionally, the trend towards adopting composite materials is evident in the latest Airbus models, depicted in Figure 1.1b. These models increasingly incorporate components made from composites as they evolve and develop. These findings emphasize the growing significance of composites in the aerospace industry.

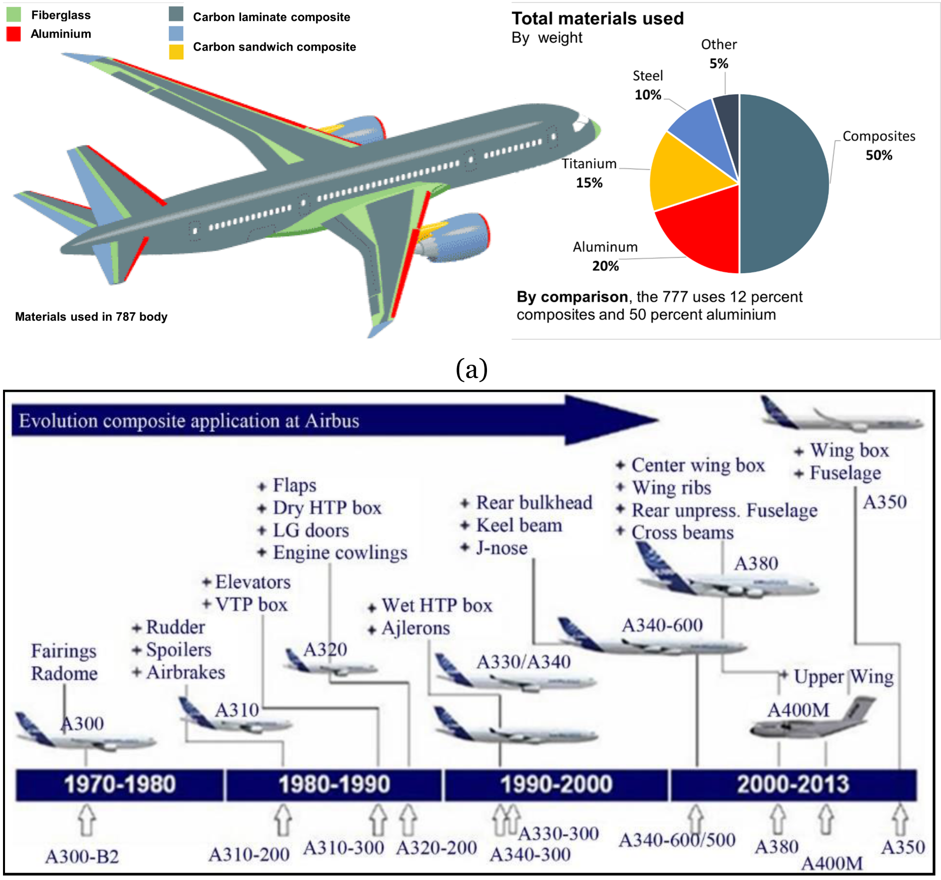

(a)

(b)

Figure 1.1: (a) Use of composite materials in the Boeing 787. (b) Evolution of the use of composites in Airbus aircraft manufacturing, from Sante (2015).

However, significant challenges are associated with assembling composites, particularly when employing mechanical joining methods such as bolts and rivets. These conventional techniques create holes in the composite structures, leading to stress concentrations around these holes. When applied to composite materials, these methods often result in fibers breaking around the holes, causing discontinuities in the composite fibers and, consequently, in the structure. As a consequence, the mechanical capabilities of composite structures are affected, resulting in a reduction of their specific strength and load-carrying capability.

Analyzing Figure 1.2, it becomes evident that the presence of a rivet caused fiber breakage and delamination in the composite structure.

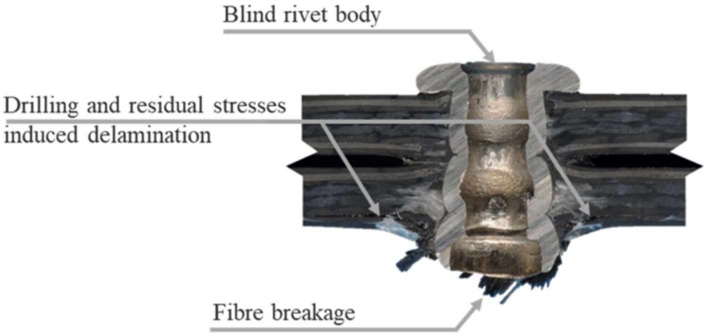

Figure 1.2: Damage in a fiber-reinforced polymer (FRP), from Omairey et al. (2021).

Taib et al. (2006) identified in their work that adhesive bonding is a viable technique for fiber-reinforced composite structures. When adhesive bonding is used instead of mechanical joining, the loads are distributed uniformly across the components, effectively avoiding the stress concentration problems related to mechanical joints. Figure 1.3 illustrates the comparison between these two methods.

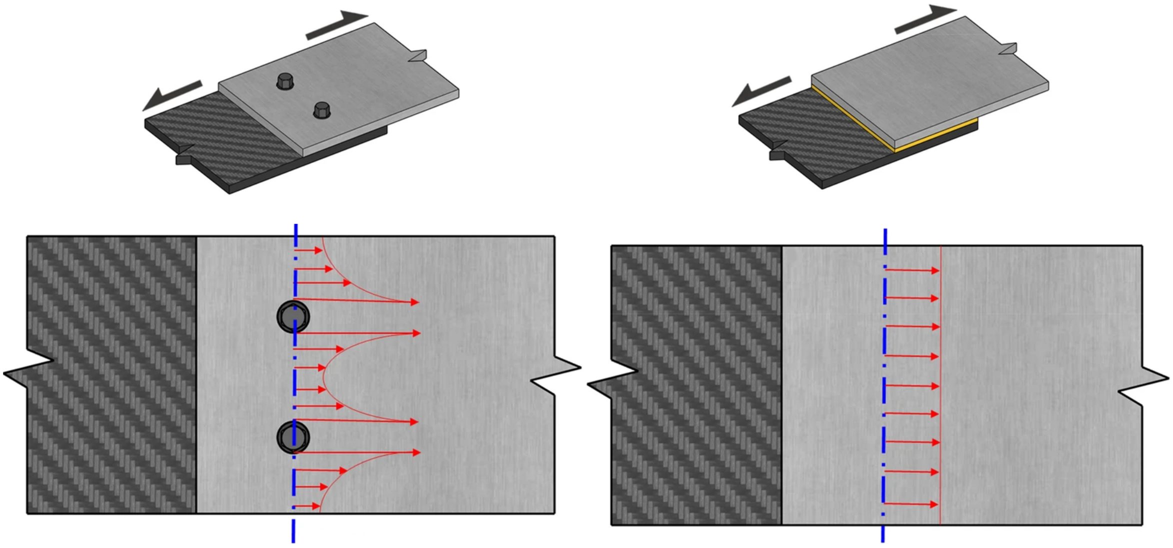

(a) Mechanical joint.

(b) Adhesive bonding joint.

Figure 1.3: Figures (a) and (b) represent mechanical and adhesive joints, respectively. The red arrows illustrates the distribution of tensile stresses applied to the joints. Adapted from Omairey et al. (2021).

In the Figure 1.3, both structures are subjected to tensile loading, with the blue dashed line representing the axis of the center of the mechanical and bonded joints. The red lines represent the stress distribution profile and have application along the blue axis. The illustration shows that the stress distribution is uniform across the structure of the adhesive joint. In contrast, the mechanical joint exhibits a considerable increase in stress around the holes, as mentioned earlier. Based on these studies, the use of adhesive bonding offers significant benefits in terms of stress distribution, ensuring an even more efficient load transfer in fiber-reinforced composite structures, and avoiding critical points of stress concentration.

Moreover, according to Markatos et al. (2013), adhesion techniques for joining aeronautical structures made of FRPs result in a substantial reduction in the fuselage airframe mass, potentially up to 15 %. Consequently, this mass reduction has a meaningful effect on the size and weight of the engines in aircraft. The lighter fuselage has direct implications for reducing fuel consumption, CO_2 emissions per passenger kilometer, and decreasing the aircraft's direct operating costs.

Based on Ejaz et al. (2022), the advantages of adhesive joints include their ability to join dissimilar materials such as composites with metals and thermosets with thermoplastics, providing a fast and cost-effective joining process, offering sealing properties, preventing galvanic corrosion, enabling uniform distribution of mechanical stress over a wider area, exhibiting better behavior in vibration damping, providing better fatigue resistance, causing minimal heat effects, having low shrinkage during curing, and offering dimensional stability. In addition, the presence of a bonded joint will reduce the propagation of high-frequency noise by absorbing the acoustic energy attached to the structure, as reported by Bishopp (2005).

Although adhesive technology has been utilized in aircraft structures for more than 80 years, its application has grown significantly in the last decade. This growth can be attributed to the development of modern aircraft like the Boeing 787, the Airbus A380, and the Airbus A350, as highlighted by Tserpes (2020).

A clear example of this application is the wing root of the McDonnell Douglas F-18 fighter aircraft. In this case, carbon/epoxy composite wings were attached to the titanium wing root using a configuration of a stepped-lap joint with FM-300 film adhesive (see Figure 1.4). Figure 1.4a presents an illustrative representation of the aircraft, including the wing spar joint. Figure 1.4b provides more detailed information about the wing spar joint, which consists of a stepped lap joint geometry of two materials: titanium (bright grey) and carbon composite (dark grey).

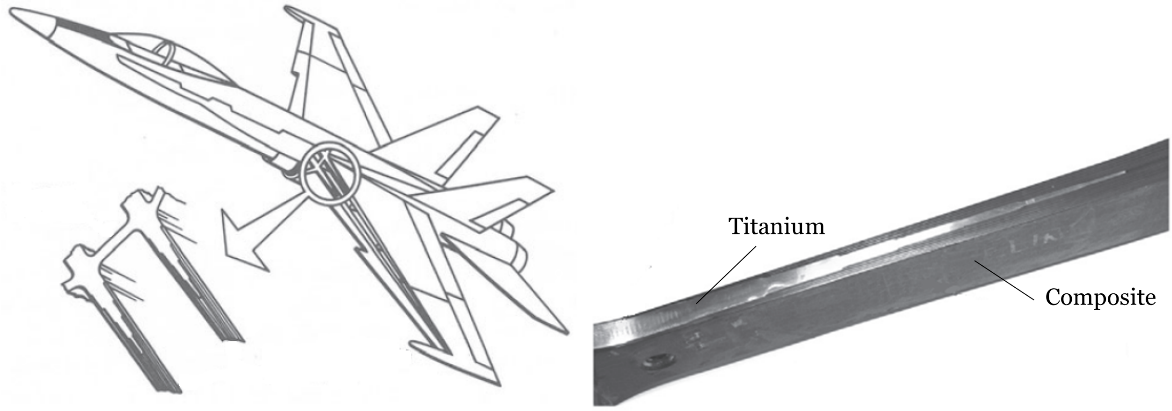

(a) (b)

Figure 1.4: Example of adhesive bonding on the F-18 aircraft. (a) Schematic representation of the composite wing to titanium fuselage bonded attachment on the F-l8 aircraft, from Driver (1995). (b) Detail of inner wing composite-to-titanium stepped-lap joint, from Seneviratne et al. (2015).

Despite the mentioned advantages of adhesive bonding over conventional mechanical joining methods, its use in primary structures is limited, currently to non-load-critical applications. Banea and da Silva (2009a) highlight the lack of reliability in adhesive joints, which prevents them from being widely implemented in aerospace application, primarily due to inadequate nondestructive inspection (NDI) techniques to identify defects and component failures. As introduced by Crane et al. (2021), without this capacity, the reliability of the structure cannot be ensured, and proof testing of the component is necessary for the certification of the flight safety of the aircraft.

Several NDI techniques can detect physical faults such as inclusions, delaminations, and porosity after an adhesive has cured. To ensure ongoing structural safety, it is also critical to identify the environmental degradation of structural materials while they are in use. Ultrasonic inspection and a stand-off technique like thermography or shearography are the NDI techniques most frequently employed to find damage in structures, as related by Crane et al. (2021). For instance, composite components may sustain severe damage that is challenging to identify. As also noted by the author, despite decades of research in NDI techniques, most of them do not detect defects efficiently, such as in the case of ultrasonic measurements, failing to detect bonding contamination or defective adhesive dispersion. Moreover, these traditional NDI systems call for heavy, costly equipment or complicated algorithms, neither of which is appealing for use in practical applications.

To surpass the disadvantage in the prediction of adhesive reliability, researchers work on new methodologies to achieve multifunctional properties for materials. This approach combines structural reliability with sensing capabilities to optimize structures for specific functional requirements. One such concept involves providing continuous diagnostic information on the condition of the constituent materials, individual components, and the entire structure throughout its service life. This concept is known as structural health monitoring (SHM), and this definition is in line with Balageas et al. (2006).

According to the author, SHM serves several crucial purposes in structural reliability:

- Replacement of scheduled maintenance: SHM aims to replace scheduled and periodic maintenance inspection with performance-based (or condition-based) maintenance (long term or at least short term) by reducing the current maintenance labor, in particular by avoiding disassembly;

- Product improvement: SHM gives the manufacturer an improvement in his products;

- Workforce impacts: SHM drastically changes the work organization of maintenance services.

According to Balageas et al. (2006), SHM is motivated by two main factors: enhancing structural reliability and addressing economic considerations. SHM minimizes accidents due to structural failures, improving overall reliability. Economically, end-users benefit from lower maintenance costs and increased reliability throughout a structure's lifespan. This relationship is depicted in Figure 1.5, where at the beginning of the structure's life, the cost of maintenance is lower, and structure quality is high. However, structures with SHM (bold lines) maintain constant reliability and incur lower maintenance costs over their lifetime compared to structures without SHM (dashed lines), which experience increased maintenance costs and decreased quality due to lower reliability during the structure's lifetime.

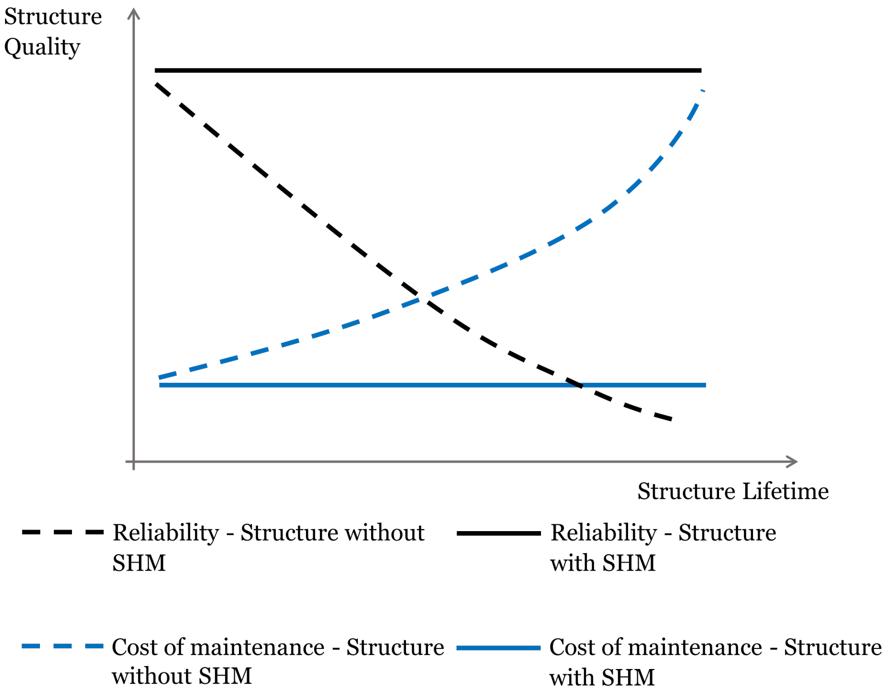

Figure 1.5: Benefit of SHM for end-users, adapted from Balageas et al. (2006).

These SHM systems can take various forms and have applications in different structures. One promising material for achieving multifunctionality is carbon nanotubes (CNTs). CNTs can act as both structural reinforcement and a sensing system due to their exceptional mechanical and electrical properties.

Thostenson and Chou (2006) demonstrated how carbon nanotube networks that conduct electricity within an epoxy polymer matrix function as sensing structures to track the beginning, nature, and progression of damage in high-tech polymer-based composites. This multifunctional material used electrical resistance measurements in direct current to monitor the internal damage accumulation in real-time and final rupture. A considerable change in the sensing curve registered the beginning of the damage and the subsequent stress accumulation by the increase in electrical resistance. Figures 1.6a and 1.6b depict these results for deformation in 0.50 wt.% CNTs-epoxy composite and glass-fiber-reinforced CNT composite, respectively, highlighting the correlation between load and electrical resistance change. These findings show promise for sensing materials based on piezoresistivity for self-sensing components, improving life prediction techniques.

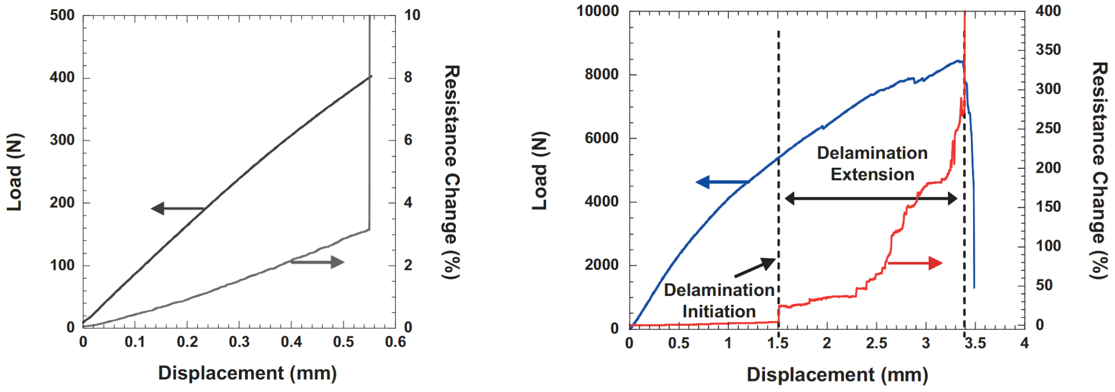

(a) (b)

Figure 1.6: (a) Resistance change in tension loading for a 0.5 wt.% carbon nanotube–epoxy composite with displacement. (b) Load-displacement and electrical resistance curves during tensile stress for a five-ply unidirectional composite specimen with a cut center ply to initiate delamination. Adapted from Thostenson and Chou (2006).

Piezoresistivity is a phenomenon that enables the correlation between mechanical stimulus (strain or stress) and changes in electrical resistance, as described by Avilés et al. (2018). The first documented report of piezoresistivity is ascribed to William Thomson (Lord Kelvin) in 1856 for metal wires. Since then, strain gauges of thin metal or semiconducting foils mounted on a backing polymeric film have applied this principle to measure strain in materials or structures. The study of piezoresistive sensors has advantages over piezoelectric sensors since it only involves electrical resistance change and not the electrical potential of the material, operating only in the mechanical-to-electrical direction, contrary to piezoelectricity that works in both ways with mechanical stimulus to the generation of electrical potential and vice versa.

In this regard, polymer composite materials offer an opportunity to integrate piezoresistive sensing by the addition of electrical conductive fillers into the matrices. Both materials combined into nanocomposites enable different sensing geometries, which result in conductive polymers with optimized electrical response, achieving better sensitivity and mechanical properties.

The exceptional properties of electrically conductive nanocomposites as structural and sensing components make them highly appealing for aeronautical applications. They find utility in various parts of aircraft, such as the fuselage, wings, and cockpit, where they need to withstand substantial loads and offer mechanical strength and structural monitoring capabilities. Aeronautical structures face several environmental challenges, including temperature fluctuations and the risk of lightning strikes, which can compromise the safety, serviceability, and reliability of components (Vertuccio et al. (2016)).

In this regard, the integration of piezoresistive capacities into adhesives to improve aircraft structures can be the next step to guarantee certification for the implementation of adhesive joints into primary aircraft and aerospace structures. Indeed, a multifunctional adhesive offers a potential solution to monitor in real-time, providing a viable joining methodology with advantages over mechanical joining methods.

When fully developed, piezoresistive sensing can create something similar to a neural network, where each structure can be monitored in real-time by integrating self-sufficient sensor networks into the aircraft to foresee risk situations and avert structural failures. These sensor networks can complement or even substitute pricey maintenance checkups.

1.2 Objectives

The main objective of this study is to explore the potential of piezoresistive sensing in adhesive joints for structural health monitoring with potential applications in aerospace structures. The study will begin with a comprehensive literature review on adhesion concepts and the piezoresistive phenomenon. Subsequently, research in epoxy-based adhesives filled with carbon nanotubes to optimize the percentages of CNTs, manufacturing processes, and analysis techniques to enhance the sensitivity of these multifunctional materials will take place. Once this optimization has been satisfied, the focus is redirected to the practical application of the adhesive with optimized detection capabilities in simple adhesive joints. By undertaking these steps, the findings of this study will contribute to the development of adhesive joints that incorporate self-sensing properties, allowing for real-time structural health monitoring. This approach utilizes epoxy adhesives reinforced with CNTs as a multifunctional system to assemble glass fiber composites.

The following tasks will be carried out to achieve the above objectives:

- The first step of this work involves obtaining an overview of the global demand for structural adhesive joints, including the potential of adhesives to provide mechanical strength and electrical resistivity to include them as multifunctional components.

- Realize an extensive study and contextualization of the piezoresistive capability of polymeric matrices of epoxy and CNTs to incorporate self-sensing properties to work as multifunctional materials for structural health monitoring.

- Develop a manufacturing process that provides the dispersion of the filler into the epoxy matrix for later production of adhesive samples made of epoxy and CNTs for further study of mechanical and electrical behaviors.

- Accomplish an electromechanical study on the epoxy adhesive reinforced with different percentages of CNTs to verify piezoresistive behavior, focusing on reaching higher sensitivity and searching for a correlation between structural deformation in three-point bending tests and variation in electrical resistance.

- After identifying the best compromise between mechanical and electrical response, the studied adhesive will be applied in single-lap adhesive joints for further study.

- Build glass fiber composite panels to cut into samples for development of adherend geometry.

- Build adhesive joint samples with adhesives of pure epoxy and epoxy reinforced with CNTs.

- Investigate the mechanical and piezoresistive response of the developed adhesive joints, searching for a correlation between electrical response and mechanical strain in flexural and tensile loading conditions.

- Extensive comparison between obtained results and those reported in the literature.

- Evaluate the current and future challenges associated with structural adhesives possessing piezoresistive capabilities for monitoring structural health.

1.3 Dissertation outline

This work is composed of five distinct chapters organized as follows:

- The current Chapter 1, **Introduction**, provides the general scope of this dissertation, its motivation, and the objectives behind the research, focusing on contextualizing adhesive joints in engineering and the use of piezoresistive sensing applied in epoxy components reinforced with nanoparticles.

- Chapter 2, **State of the Art: Piezoresistive Characteristics of Reinforced Adhesives for Structural Monitoring**, consists of an objective introduction, contextualization, and analyses related to adhesives applied in engineering with a focus on aerospace domain. The Chapter has two main sections. The first is related to structural adhesives. The second describes the piezoresistive phenomenon applied in sensing components for structural health monitoring applications with the reinforcement of CNTs in an epoxy polymer.

- Chapter 3, **Experimental Procedure** is divided into three main sections and describes the used materials, the experimental procedure for sample manufacturing, and the sample analysis. The materials selection is based on the literature review, followed by a step-by-step on adhesive and single-lap joint fabrication. The applied test methodologies are described in detail.

- Chapter 4, **Results and Discussion**, presents the experimental results for mechanical and electrical tests of adhesive and single-lap joint specimens. A comprehensive study and analysis of the findings are presented through figures and tables.

- Chapter 5, **Conclusions**, summarizes the key findings of this research and offers recommendations and research directions for future work.

Chapter 2

State of the Art: Piezoresistive Characteristics of Reinforced Adhesives for Structural Monitoring

This chapter overviews adhesive technology and its application in adhesive joints. It will include a brief discussion on materials, especially epoxy matrix as adhesives, different geometries, and methodologies for adhesive implementation in engineering. Electrical properties are essential to enable a multifunctional material. This chapter will, therefore, introduce piezoresistive sensing for structural monitoring through reinforcement with carbon nanotubes.

The main objective is to build a solid theoretical foundation for incorporating sensing capabilities into adhesive joints to ensure proper inspection and increase the overall reliability of structures. As a result, this chapter presents two parts. The first part will cover the concepts of structural adhesives, while the second will focus on piezoresistive phenomena and their application in sensing structures using carbon nanotubes.

2.1 Introduction to adhesive bonding

Adhesive bonding is present in almost every aspect of our existence, from basic applications to advanced space technology. Banea and da Silva (2009a) reported that the use and production of adhesive materials date back hundreds of thousands of years and have played a significant role in various industries and technologies that dominate our daily lives, such as aeronautics, aerospace, electronics, automotive, construction, and traditional industries such as packaging.

In particular, the aviation industry has witnessed numerous examples of adhesive usage in structural components. Bishopp (2005) compiled some of these cases, ranging from the Wright brothers' use of a protein-based wood-working glue to laminate spruce to modern aircraft made of aluminum, titanium, stainless steel, and fiber-reinforced composites, which have components structurally connected with synthetic adhesives, such as epoxy, phenolic, or polyimide. These adhesives bond internal structures, such as bars and stringers, to wings or sandwich components. As noted by Driver (1995), the Second World War's demands had a significant impact on the development of adhesive bonding methodology in aviation. This advancement was necessary for assembling spruce and wood components in aircraft construction.

The quest for increased performance and mass reduction in aerospace industry has replaced traditional materials for composites. Pantelakis (2020) compared aluminum alloys with carbon, glass, and kevlar fiber composites and found that the ultimate tensile strength of the composites is 47 % to 69 % higher than that of aluminum alloys, even though they have a lower density, resulting in higher specific strength. These advantageous properties justify the preference for replacing metals in structures, directly impacting aircraft mass.

The increased development and utilization of composite materials have motivated improvements in design concepts, advanced manufacturing, and assembly techniques. Omairey et al. (2021) introduced that the increasing use of composites has led to complex applications and different manufacturing methodologies, resulting in the proportional growth of joining similar and dissimilar materials. These complex systems involve joining materials with diverse mechanical behavior, surface adhesion, and thermal expansion coefficients. Although welding, mechanical fastening, and riveting are suitable for metallic elements, they are not directly applicable to composite materials.

Markatos et al. (2013) and Omairey et al. (2021) identified that load-critical carbon fiber reinforced polymer (CFRP) structures are assembled, mainly using mechanical fasteners, as thermoset composites are not thermally weldable. Drilling composites with post-manufacturing mechanical fasteners or rivets negatively affects the reinforcement and the matrix of these composites, causing delamination and initiating cracks in the matrix due to stress concentrations around the holes. Moreover, these structural unions offer a low sealing performance and add additional mass to the composite system. Furthermore, due to the limited bearing capacity of composites through thickness, an increase in thickness to support more load may result in additional mass penalties.

Adhesives have become a valuable technology for joining fiber reinforced polymer (FRP) components in structures due to their ability to overcome the challenges associated with mechanical fastening methods. In aeronautical structures, two main types of adhesive bonding are commonly employed, as described by Hart-Smith (2011). The first type, known as structural bonding, utilizes adhesives like epoxy, phenolic, or acrylic to transfer loads between structural components, ensuring the integrity of the overall structure. This type of bonding is crucial for maintaining the structural integrity and load-bearing capacity of aircraft components. The other type is sealants, whose purpose is to prevent corrosion at interfaces and protect against exposure to atmospheric agents.

In aircraft structures, especially those involving composite components, structural bonding is preferred, as emphasized by Razak and Othman (2011). The primary purpose of adhesive technology becomes evident in this context, as the effectiveness of bonded components significantly impacts structural integrity and overall safety in aircraft.

A conservative definition of adhesive joints includes the adhesion of two individual surfaces of components through an adhesive that can resist separation. This definition was proposed by Kinloch in 1987. On the other hand, a more recent description by Banea and da Silva (2009a) defines adhesive joints as complex formulations of many components with unique functions. In the aerospace industry, the predominant bonding method relies on so-called structural adhesives, based on monomer compositions that polymerize or cure to provide high modulus and strength to bonds (Bishopp (2005)). These definitions imply that an adhesive-bonded joint presents three distinct parts, which are the substrate, or adherend, the adhesive layer, and the interfaces between the substrates and adhesive. This description is represented in Figure 2.1.

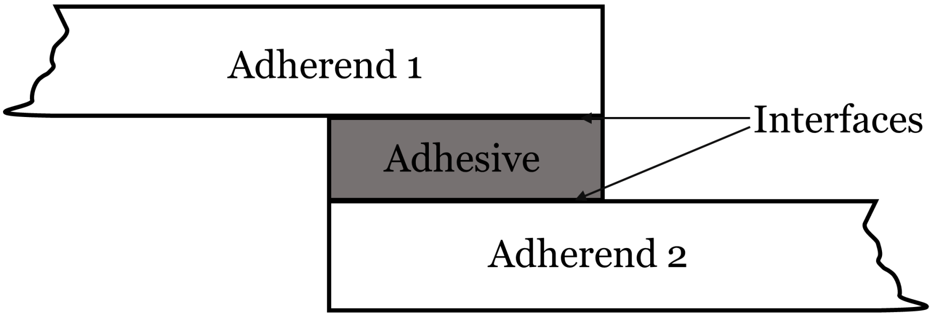

Figure 2.1: Distinct parts of an adhesive joint, adapted from da Silva et al. (2011).

Compared to other structural bonding methods for composites, adhesives offer several advantages, particularly related to efficient and uniform load transfer, which results in higher rigidity and better fatigue properties. These joints are expected to perform well under sustained and cyclical loads. The wide range of available adhesives allows for compatibility in joining different types of similar and dissimilar materials. According to Driver (1995), the bonded joint should ensure an effective transmission of loads between adherents, and to accomplish this, it should have a larger bond area, guaranteeing a uniform, thin, and continuous bond line.

However, Markatos et al. (2013) and Omairey et al. (2021) identified an inherent difficulty in adhesive joints' inspection, since they are difficult to disassemble, despite the many advantages over other mechanical joining methods. Proper monitoring is essential during the manufacturing process to ensure the quality of the adhesive joint, since the adhesion process results from several variables, including surface preparation, adhesive type, filling, fixture, curing, and environmental conditions during manufacturing. However, adhesive joints also have problems related to their in-service life and the sensitivity of bond line integrity to environmental factors. Conditions such as moisture absorption, service temperature, and loading can affect the bonding strength of adhesive joints. In this regard, Song et al. (2010) emphasized the importance of using appropriate manufacturing methods and implementing monitoring techniques for adhesive joints to guarantee a proper bond.

In summary, adhesively bonded joints offer numerous benefits despite having challenges in inspection, durability, and sensitivity to environmental conditions. Table 2.1 reviews the advantages and disadvantages of mechanical and adhesive bonded joints.

Table 2.1: Advantages and disadvantages of mechanical and adhesive joints in composites, based on the considerations made in the works of Bishopp (2005), Tserpes (2020) and Omairey et al. (2021).

	Adhesive bonding	**Mechanical joining**
Advantages	Low stress concentrations in adherends Higher stiffness joint Considered to be a lightweight joining solution Excellent fatigue and corrosion performance External surfaces remain unaffected Surface preparation do not damage adherend reinforcement Ability to join dissimilar materials	Easy to disassemble Easy to recycle joining material Easy to inspect and require a lower level of quality control
Disadvantages	Hard to disassemble Poor material recyclability opportunity Hard to inspect and require a high level of quality control	High stress concentrations in adherends Lower stiffness compared with adhesively bonded joint Fasteners and bolts add considerable mass Fasteners protrude to external surface Prone to fatigue and corrosion Drilling and bearing damages the composite adherend

The design of the adherent must ensure that the adhesive will hold even if the supporting structure is damaged and remain intact for the structure's entire lifespan. According to Driver (1995), bonded joints should be designed to exploit the unique behavior of adhesives, which differs from what is typically expected in welding and riveting processes.

Various factors influence joint performance, such as the geometry of the joint, the materials of the adherents, their surface preparation, the chemical compatibility between the adhesive and adherend, the type of adhesive used, and the surface cleaning and preparation process. To achieve higher reliability and reproducibility, a comprehensive understanding of how these factors affect joints is crucial. Additionally, effective nondestructive inspection (NDI) techniques are necessary to evaluate any contaminations and defects in the adhesives during the manufacturing process and the in-service life of the structure. This chapter aims to thoroughly review the impact of these factors on joints and enhance the understanding of adhesive bonding.

2.2 Adhesive materials

The adhesives discussed in this section are mainly for structural applications. These structures' types require specific properties such as high strength, temperature resistance, fast bonding capability for various materials, and flexibility. The selection of adhesives for each case should have as base the specific properties required for the intended application. According to Tserpes (2020), an adhesive is classified as structural if it can withstand a single-lap shear test load of at least $6.9\ \mathrm{MPa}$.

The success and performance of adhesive joints largely depend on the choice of material. Different types of adhesives exhibit unique properties that make them suitable for specific uses. Factors like bonding strength, flexibility, temperature resistance, and chemical compatibility are crucial considerations and can be ensured by a proper adhesive choice. Understanding the characteristics and performance of adhesives is essential to achieve reliable and durable joints. Table 2.2 presents a comprehensive summary of various adhesive types, along with their fundamental properties, based on the work of Banea and da Silva (2009a); Ebnesajjad (2011); Tserpes (2020). The table provides essential information such as main characteristics, service temperature range, and the curing process employed.

In the context of aerospace applications, a range of adhesive types has been developed based on the previous materials to address the specific requirements of these industries. According to Smith (2021), epoxy, phenolic, and acrylic adhesives are commonly employed for structural purposes in aerospace. It is essential to note that sealants, as highlighted by this source, are typically not used for structural applications. These sealants do not bear loads but are instead applied to protect surfaces from corrosion at interfaces promoted by galvanic action or atmospheric exposure.

For aeronautical applications, adhesives are commonly available in either paste or film forms. High-viscosity paste adhesives often result in thicker bond lines, which can fill and bridge gaps between bonded surfaces and provide more elongation and impact resistance, as indicated by Tserpes (2020). On the other hand, film adhesives are more suitable for components with larger surface areas. While film adhesives are better suited for composite adherents (an aspect of increasing importance in manufacturing bonding processes), paste adhesives are preferable for metallic adherends.

In addition, adhesives must be inert systems, requiring compatibility between adherends and adhesives. In accordance with Banea and da Silva (2009a), epoxy adhesives, commonly used for composite matrices, are preferred for bonding composites based on epoxy matrices due to the compatibility between the resin and adhesive.

Applying the correct adhesive is crucial for a successful bond. However, the adhesive selection process is complex, given the absence of a universal adhesive that meets all requirements. The selection of the adhesive, therefore, involves several factors, including the type and nature of the substrates, the geometry, the curing process, the methods of adhesion, the expected environmental conditions, and the stresses that the joint will undergo in service. The latest is crucial, particularly for structural adhesives, where failures during use can have severe consequences. Adhesive properties can vary significantly, highlighting the importance of a well-informed selection process for a proper joint design.

Table 2.2: Typical adhesive key properties and manufacturing conditions, adapted from the works of Banea and da Silva (2009a); Ebnesajjad (2011); Tserpes (2020).

Adhesive	**Characteristics**	**Service temperature (°C)**	**Cure**
Epoxy	High strength and temperature resistance, relatively low cure temperatures, easy to use, great versatility, low cost, excellent for structural adhesives. Selection of different hardeners, resins, modifiers, and fillers allows desirable properties for particular applications Do not produce volatiles during curing and have low shrinkage. Low peel strength and flexibility and are brittle	−157 to +204*	One-part epoxies cure with temperature. Two-part epoxies cure at room temperature (cure can be accelerated with temperature)
Cyanoacrylates	Fast bonding capability to plastic and rubber but poor resistance to moisture and temperature No added catalyst or mixing needed No solvent to evaporate during bond formation High bond strength with thin glue line	−54 to +80	Fast cure (in the order of seconds or minutes) upon exposure to moisture at room temperature Contact pressure is sufficient
Anaerobics	Designed for fastening and sealing applications in which a tight seal must be formed without light, heat or oxygen, suitable for bonding cylindrical shapes	−55 to +232	Cure in the absence of air or oxygen at room temperature
Acrylics	Versatile adhesives with capabilities of fast curing and tolerate dirtier and less prepared surfaces Low shrinkage during cure High peel and impact strength, combined with excellent shear strength	−40 to +120	Cure through a free radical mechanism
Polyurethanes	Good flexibility at low temperatures and resistance to fadigue, impact resistance, and durability Good for bonding plastics difficult to bond Very good adhesion to many substractes and high adhesion	−200 to +80	One-part thermoplastic in solvents Two-part thermosetting products in liquid form Room temperature
Silicones	Excellent sealant for low-stress applications, high degree of flexibility and very high-temperature resistance, capability to seal or bond materials of various natures, long cure times, and low strength	−60 to +300 (350)†	Room temperature
Phenolics	Good strength retention for short periods, limited resistance to thermal shocks	−40 to +175 (260)†	Cure with temperature and high pressure
Polyimides	Thermal stability, dependent on a number of factors, difficult processability Available in liquid or film forms	−196 to +250 (300)†	Cure with temperature and high pressure
Bismaleimides	Very rigid, low peel properties	−50 to +200 (230)†	Cure with temperature and high pressure

*With different filler materials; †intermittent

2.3 Factors influencing bonded joint performance

As previously mentioned, the effectiveness of adhesive-bonded joints is influenced by a range of factors, including adhesive thickness, overlap length, stacking order, ply angle, fillet design, composite bonding techniques, surface preparation, and material properties (Cardoso et al. (2019)). It is essential to take all these aspects into account during the design phase to achieve optimal performance in bonded structures. Consequently, numerous studies have investigated the impacts of these properties and characteristics on adhesive behavior, mainly in fracture modes.

2.3.1 Effect of joint configuration

In the previous section, different adhesive materials were explored. This section aims to elucidate the impact of joint design on the reliability and performance of structures. The specific geometry of a joint is an outcome of its design, developed to meet the requirements of particular applications.

As highlighted by Banea and da Silva (2009a), the strength of a given joint type for a specific load depends on the stress distribution within the joint. This distribution is influenced directly by the joint's geometry, just as the mechanical properties of the adhesive and adherend materials. The literature presents a range of joint geometries, among which the single-lap joint (SLJ) is the most extensively studied, often in conjunction with double-lap joints (DLJ), scarf joints, and stepped-lap joints. Additionally, researchers have examined other configurations like strap joints, butt joints, corner joints, stepped-scarf joints, T-shaped joints, L-section joints (LSJ), and tubular lap joints. Figure 2.2 represents four main categories of geometries, including previously mentioned geometry types.

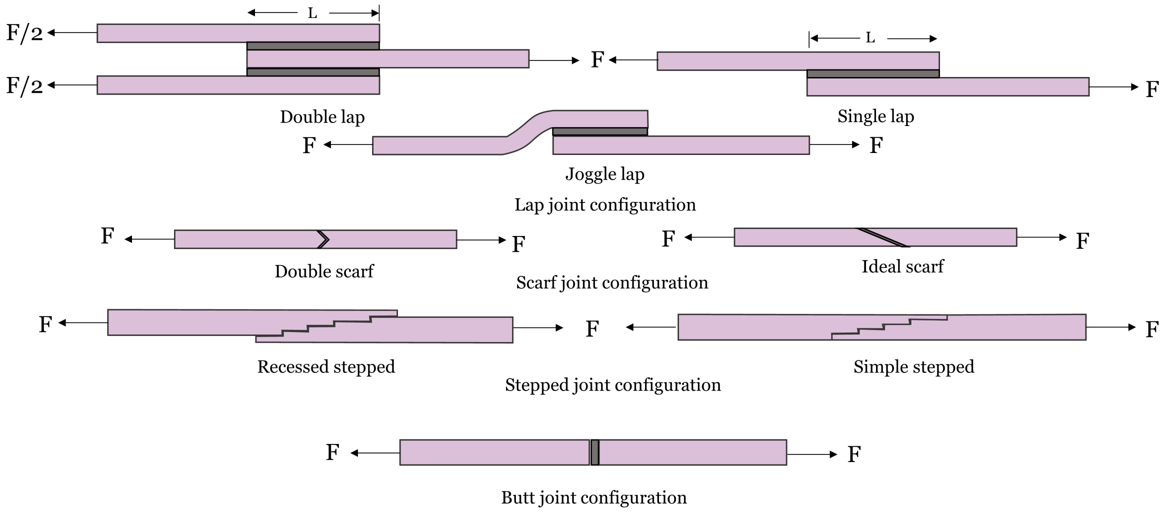

Figure 2.2: Basic joint configurations, adapted from Shishesaz and Hosseini (2018).

In the scheme, the variable L symbolizes the overlap length, while F denotes the tensile force applied to each joint structure along with the corresponding actuation direction. Notably, the adhesive and the adherend-adhesive interface are depicted in a darker shade, offering a clear visual representation.

The previous figure illustrates a crucial idea: different geometries result in distinct contact areas and force distributions, generating specific joint stresses. Several factors contribute to the stress distribution, including the overlap length, adhesive and adherent thicknesses, material properties, and stress-strain relationships in the adhesive/adherent system. These factors interact in complex ways, leading to variations in stress distribution. Notably, Shishesaz and Hosseini (2018) mentioned that even slight alterations in joint design can significantly impact peel stresses.

When analyzing the different types of joints, Banea and da Silva (2009a) observed that DLJ, scarf, and stepped joints are designed to relieve peeling stresses, in contrast to SLJs. Adhered shaping also plays a role in reducing peel stresses, especially in composite joints. To understand the degree of influence of the joint configuration on performance, Barbosa et al. (2018) undertook a comparative study involving a range of geometries and adhesives with diverse characteristics. Their investigation covered three adhesives and four joint types: SLJ, DLJ, stepped-lap, and scarf joints. The study's primary findings underscored that the optimal joint choice heavily depends on the adhesive type. Less ductile adhesives are better suited to joint geometries with pronounced stress variations, while stronger but more brittle adhesives are better suited to geometries with more uniform stresses. Interestingly, the SLJ displayed the highest stress values among all tested joints, particularly along the overlap edges.

According to Devries and Adams (2002), in SLJs, the distribution of stresses in the overlap zone is compressive in the central region but changes to tensile stresses near the overlap ends (see image (a) of Figure 2.3). At the overlap ends, these tensile stresses can become very significant. During testing, close examination of lap joint specimens often reveals initial signs of failure in the form of detachment at the ends of the overlap.

This stress distribution arises due to inherent asymmetry, leading to a rotational effect. However, this effect is mitigated for DLJs, which enables symmetry of load distribution, eliminates transverse deflections, and reduces maximum stress. This concept finds its explanation in the work of Banea and da Silva (2009a). The subsequent Figure 2.3 graphically illustrates this occurrence.

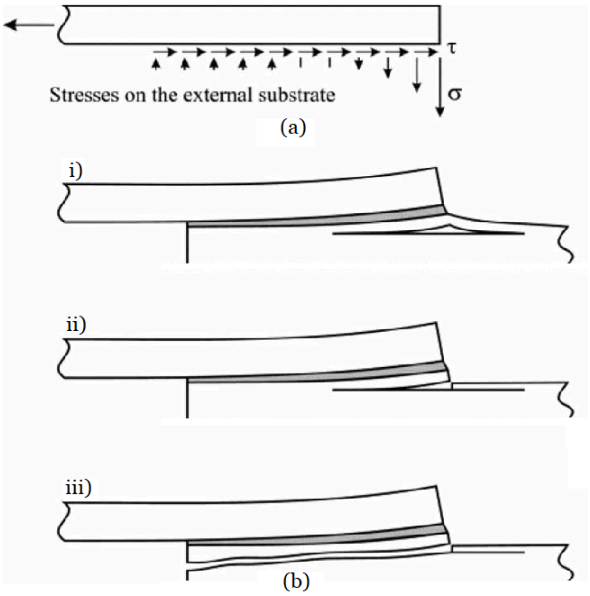

Figure 2.3: Failure of SLJ caused by transverse (through-the-thickness) stresses in composite substrates, adapted from Banea and da Silva (2009a). (a) Stress distribution across half of the adherend overlap length. (b) Sequential images depicting the progression of failure mode.

This figure explains the relatively low through-thickness strength of many composite materials, particularly in the case of FRP composite substrates. It leads to high through-thickness stresses at the ends of the overlaps. These scenarios, as explained by Banea and da Silva (2009a), often lead to failure due to transverse stresses, causing delamination of the FRP substrate. For this reason, joints designed with robust adhesives might paradoxically precipitate the early failure of joints, with the composite failing sooner than the adhesive itself. This concept is reinforced by Budhe et al. (2017), which emphasizes the necessity to minimize stress concentrations during joint design. Elevated peel and interfacial stresses, such as cleavage, should be avoided or minimized and effectively transformed into shear and compressive stresses.

Furthermore, the study by Barbosa et al. (2018) evaluated stepped-lap joints, revealing improved behavior compared to SLJ. Meanwhile, the scarf joint displayed a smoother and more evenly distributed stress profile across the overlap length, culminating in superior performance within the study. This joint takes advantage of the inherent strength of adhesives, even in the context of brittle samples, attributed to their typically uniform stress distributions.

Similarly, for a comprehensive understanding of how configuration characteristics impact mechanical properties, Barile et al. (2020) conducted a study comparing two different cases. The investigation included testing and evaluation of failure modes for both single and joggle lap joint (JLJ). The mechanical testing results reveal that single-lap specimens are stronger than joggled-lap specimens. Furthermore, these results elucidate dissimilar damage modes between the two types of specimens. In joggled lap-joint specimens, failure occurred as an adhesive-layer peeling consequence, inducing fiber/matrix debonding, eventually leading to the fracture of the lamina's fibers. Conversely, for single-lap specimens, initial adhesive failure manifested through the crack opening, propagating widthwise through the adhesive until reaching ultimate failure.

In a previous investigation, Taib et al. (2006) explored various joint configurations, SLJ, DLJ, JLJ, and LSJ. The study focused on how these four configurations influence the load-bearing capacity of the joints. Notably, the joint's geometry significantly affects its ability to withstand loads, a conclusion that continues to hold in subsequent studies.

Among these configurations, JLJ exhibited the lowest ultimate load (3935 N) and displacement (0.6 mm) capabilities despite its prevalent use in aviation applications. In contrast, DLJ displayed a higher displacement to failure (3 mm). When circumstances promote the development of cracks along the free edges, the cracks' propagation can accelerate and eventually lead to joint rupture. These results validate the relationship between geometry and load-bearing performance.

Undoubtedly, the SLJ has garnered the most attention among joint types due to its simplified fabrication process. However, its efficiency in terms of load-bearing capacity per unit of bonded length is the lowest among the mentioned configuration types. Nevertheless, there exist additional geometric parameters, as mentioned earlier, that also influence joint performance, which will be introduced in the subsequent section.

2.3.2 Manufacturing bonding process

The bonding procedure is a critical factor to consider. The bonding technique significantly affects various parameters, including the failure process, failure mode, and joint strength. According to Kim et al. (2006), there are two primary methods for joining FRP: co-curing and secondary bonding. These methods differ primarily in the number of components involved. Co-curing bonding involves fewer individual parts compared to secondary bonding.

Figure 2.4 illustrates the main manufacturing processes, depicting the concepts of co-curing without adhesive (CCN), co-curing with adhesive (CCA), secondary bonding (SEB), and co-bonding (COB).

As defined by Song et al. (2010), CCN does not require an additional adhesive because the excess resin from the prepregs forms a structural bond between the adherends, essentially acting as the adhesive itself. In the CCA method, there is the introduction of an adhesive between two uncured laminates. SEB involves bonding two cured laminates using an adhesive, following the adhesive's specific cure cycle. With the COB technique, one adherent is cured along with the adhesive. For both co-bonding and co-curing methods, the prepreg's curing time and properties dictate the overall curing process.

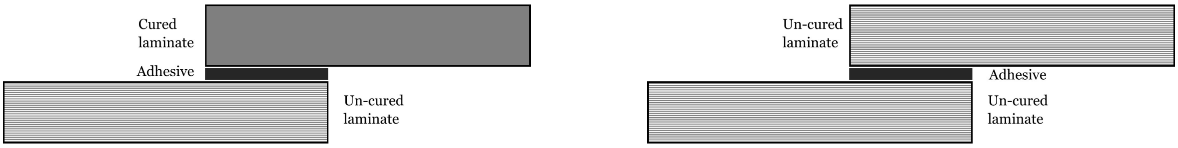

(a) Co-bonding (b) Co-curing with adhesive

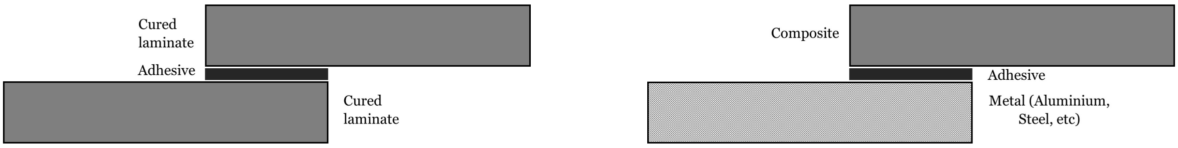

(c) Secondary bonding (d) Multi material bonding

Figure 2.4: Diagram of manufacturing bonding processes between composite components, from Budhe et al. (2017).

In addition, Budhe et al. (2017) explored the concept of multi-material bonding, similar to secondary bonding (see Figure 2.4d). However, unlike exclusively using cured composite substrates, this method involves bonding different materials, including metal substrates such as steel, aluminum, and titanium. Despite the potential for multiple materials, CCN or COB are generally preferred over SEB due to the efficiency gained from fewer components and curing cycles. Consequently, this technique finds its most common application in the repair of composite structures. The SEB process is more suited for larger and more complex components.

Moreover, Song et al. (2010) conducted a comparative study of various manufacturing methods and investigated their influence on the strength of bonded composite joints. They examined different specimens produced through the manufacturing methods described earlier. The findings revealed that secondary bonded joints exhibited higher strength (25.9 MPa) when compared to COB (12.6 MPa) and CCN (24.6 MPa) joining techniques. The SEB joint showed similarities to the non-adhesive co-curing scenario, comparing the yield strength.

In a more comprehensive approach, Park et al. (2010) aimed to investigate the impact of environmental conditions alongside manufacturing methods. To achieve this, they explored three distinct environmental factors with four different manufacturing methods, including CCN, SEB, and COB. This research focused on SLJs as the testing configuration. Notably, the results showed that CCN without adhesive was the most favorable mechanical performance observed, which exhibited the highest strength (24.2 MPa). Within the scope of this specific study, SEB joints and COB joints followed CCN in terms of mechanical response. When comparing this study with the previous one carried out by Song et al. (2010), the inconsistencies in the results become evident, with the author suggesting that these differences are the result of the material system and manufacturing method specified in his work.

On the same line, Mohan et al. (2014) conducted a comparable study to comprehend the mechanical behavior of a single CCN joint and a double SEB joint system, assessed through the double cantilever beam test. Their research revealed that the CCN process released free and bound water into the adhesive layer, which plasticized the polymer and introduced voids at the interface. On the other hand, SEB mitigated the accumulation of water at the interface by facilitating its escape from the laminate during the manufacturing process. However, the water presence in the adhesive resulted in initial defects, significantly impacting fracture toughness values. The double SEB joints primarily exhibited cohesive failure, while the CCN experienced interfacial failure.

In 2015, Mohan et al. conducted a study focused on mixed-mode fracture toughness. The findings were consistent with the earlier study's outcomes. CCN joints suffer from water retention within the joint, a problem exacerbated by its release during the curing process. This phenomenon negatively affected the adhesive joint's quality due to voids introduced at the adherend/adhesive interface. Under mode I and II loading conditions, CCN bonded joints demonstrated lower strength when compared to SEB joints. This difference in strength was primarily attributed to the higher presence of voids within the bulk adhesive and at the interface of CCN joints.

In a broader perspective, Budhe et al. (2018) conducted an in-depth examination of environmental factors that impact the durability and repair of adhesives. The author emphasized the need to explore new methods, such as vacuum-assisted curing, which produces high-quality adhesives with minimal voids in the bond line, similar to autoclave curing. Furthermore, it is recommended the production of joints using the COB method due to its lower moisture absorption compared to the co-cured methodology. The importance of further exploration in this domain is underscored, requiring additional testing to enhance the performance of composite bonded joints.

2.3.3 Effect of adhesive thickness, adherend thickness, and overlap length in joint strength

This subsection examines the significant impact of adhesive thickness, adherend thickness, and overlap length on joint strength and failure mode.

The separation between adherends defines the bond line, which directly corresponds to the adhesive thickness. This connection line is of primary importance in characterizing the joint, as it significantly affects its strength. The existing literature consistently presents that for SLJs, the lap joint strength generally increases with decreasing bond line thickness (Kim et al. (2006); da Silva et al. (2009)), with exceptions of elastomeric adhesives (Banea and da Silva (2009b)).

The literature includes many studies evaluating the influence of bond line thickness on joint strength. The main conclusion discovered in most cases is that thicker bond lines reduce joint strength. This finding is justified in Omairey et al.'s work by the trend of thicker bond lines to accommodate defects such as voids, microcracks, and higher interface stresses. On the other hand, as emphasized by Simmons et al. (2020), a thick bond line tends to serve as a potential weakening factor, attributed to the probability that the mechanical strength of thicker adhesive films is comparably lower than that of the substrates, thereby making the joint more brittle. However, the author emphasizes several advantages of thicker bond lines over thinner ones in adhesive joints. Adhesives are typically more flexible than the materials they bond, enhancing their ability to absorb energy during impacts. This impact absorption capacity is further improved with a thicker bond line, a particularly important attribute when bonding rigid materials such as metals in adhesive joints.

One part of the work of Ahmed et al. (2018) was to develop a comparison between experimental and finite element analysis (FEA) failure loads for three distinct values of bond line thickness for a SLJ. The work results showed that a bond line thickness of $0.2\ \mathrm{mm}$ has a better mechanical behavior with a higher failure load ($9.8\,\mathrm{kN}$) for SLJs tested under shear stress over the bond line thicknesses of 0.5 and $1\ \mathrm{mm}$. The evaluation of the simulation results led to the conclusion that the bond strength depends not only on the thickness of the bond line but also on the geometry, the overlap length, the stiffness of the substrate, and the many variables to which the adhesion may be subject. For the Fernández-Cañadas et al. (2019) case study, the greatest reduction in shear and peeling stresses was obtained for an adhesive $0.52\ \mathrm{mm}$ thick.

The study conducted by Jensen et al. (2019) involved a large-scale experimental investigation, where 1205 samples were tested. The primary objective of this research was to establish correlations between various processing parameters such as adhesive type, bond line thickness, adherend thickness, the presence of an overflow fillet, and the mechanical properties of bonded SLJs. The comprehensive nature of this study allowed them to draw several generally accepted conclusions. They found that the effective strength of SLJs increased when the bond line thickness decreased, the adherend thickness increased, and when an overflow fillet was present. These conclusions were supported by analyzing standard average values from their extensive dataset.

The thickness of the adherend is a critical parameter that merits investigation to understand its impact on mechanical strength. In the study conducted by da Silva et al. (2009), two key factors underline the importance of adherend thickness on joint mechanical strength. Firstly, in cases where adherends have relatively lower strength, an increase in adherend thickness can support the adherend's ability to resist plastic deformation, thereby enhancing its overall strength. Contrarily, when dealing with adherends of higher strength and thickness, it can lead to a reduction in joint overall strength due to the amplification of bending moments.

Sahin and Akpinar details this phenomenon in their research. The authors noted that in the context of structural lap joints subjected to tensile loads, increasing the adherend thickness results in two competing effects. On one hand, the increase in thickness leads to a higher bending moment, which can lead to joint failure, similar to the findings of the previous study. However, on the other hand, this increase in thickness enhances the flexural rigidity of the joints, reducing transverse deflection during loading, which ultimately has a positive effect on the failure load.

The studies reviewed provide valuable insights into the complex structural behavior of SLJs concerning adherend thickness, particularly in bending moment, flexural rigidity, and specific mechanical properties. The last reviewed parameter that can significantly impact joint strength is the overlap length. Several studies have explored this aspect with different findings.

Firstly, as noted by da Silva et al. (2009), the influence of overlap length becomes more pronounced as the adherend's strength increases. Barbosa et al. (2018) also observed that in SLJs, an increase in the overlap length corresponds to an enhanced maximum load until failure. These results are similar to those in Fernández-Cañadas et al.'s work, where they found that maximum shear and peel stresses increase with an increasing overlap length. Their research showed that for SLJs, the load is more sensitive to overlap length than adhesive thickness. Additionally, Ozel et al. (2014) and Li et al. (2015) support the idea that overlap length does not affect failure load proportionally but concluded that peel stress near the end of the adherend increases with longer overlaps, which leads to a larger delamination failure area and impacts stress distribution.

Nevertheless, a study conducted by Akpinar and Sahin (2021) found different results. They suggested that the influence of the overlap length on joint strength is relatively minor compared to adherend and adhesive thickness. Their research revealed that the adhesion failure within these joints was primarily characterized by a peeling mechanism and load transfer predominantly occurred locally at the ends of the overlap in SLJs. Consequently, they concluded that the previous findings regarding the impact of overlap length on joint strength might not be as significant as the influence of the two previously discussed geometric parameters.

In addition, the type of adhesive can also influence the strength results due to the overlap length of the adhesive joints. Banea and da Silva (2009b) suggests that ductile adhesives experienced an almost proportional increase in joint strength with longer overlap lengths, in contrast to brittle adhesives. Therefore, the nature of the adhesive should be considered when assessing the effects of overlap length on joint strength.

To further reinforce the idea that overlap length does have an impact on joint strength, Ozel et al. (2014) conducted a study exploring different fiber orientation sequences, adherend thicknesses, and overlap lengths and their influence on SLJs' mechanical behavior. They found that the load-carrying capability increased with longer overlap lengths. It is essential to note that in the case of composite adherends, overlap length had a more substantial impact on the joint's load-carrying capacity compared to aluminum adherends.

The results of FEA conducted by Ozel et al. align with the experimental findings. They found that the ends of the overlap length experienced the highest peel and shear stresses, consistent with previous studies, such as Banea and da Silva (2009a). These findings collectively illustrate that the influence of overlap length on joint strength is complex and depends on various factors, including the material properties of the adherends and the type of adhesive used.

A comprehensive overview of numerous studies investigating the impact of various variables on the performance of bonded joints is provided in this section. Table 2.3 provides a concise summary of each study, including their main objectives, methodology, adhesive material, adhesive thickness, adherend thickness, and overlap length, as well as their principal conclusions. This table serves as a reference for comparing the various geometric parameters examined in each work, facilitating a comprehensive understanding of the impact of these parameters on SLJs. Discriminating these parameters allows for a more in-depth analysis of each study's findings since the results may not always be consistent with each other.

Upon a meticulous examination of the reviewed studies presented in Table 2.3, it becomes evident that establishing a comprehensive, generalized relationship across the three assessed parameters is a challenging work. Instead, the outcomes highlight the complex interplay of these parameters. Furthermore, several other factors, including the material properties of the adhesive (whether it exhibits ductile or brittle behavior), the type of loading applied, and the nature of the adherend material, significantly contribute to this complex dynamic. In light of these findings, it is essential to consider all of these parameters when optimizing the geometry to maximize the joint performance. This viewpoint is notably reinforced by the study conducted by Budhe et al., which strongly emphasizes this complex system behavior.

2.3.4 Effect of surface treatment on joint strength and in fracture modes

Surface treatment stands as a fundamental parameter with the potential to exert a substantial impact on joint strength.

At the root of the mechanical strength of a joint is the establishment of chemical bonds between the atoms located on the surfaces of the adhesive and the adherend. This fundamental process is established during the polymerization phase of the adhesive. A crucial initial step in this process is to ensure a certain degree of chemical affinity between the adhesive and the adherent. This fundamental affinity confers mechanical resilience and prolongs the adhesion's lifespan. Complementing the chemical affinity are the physical interconnections that manifest across the adherent/adhesive interfaces, as detailed by Sorrentino et al. (2018) in their study.

Table 2.3: Compilation of studies investigating bonded joint performance with a focus on geometrical parameters: adhesive thickness, adherend thickness, and overlap length.

Reference	**Objective and Method**	**Adhesive**	**Adhesive Thickness (mm)**	**Adherend Thickness (mm)**	**Overlap Length (mm)**	**Key Conclusions**
Kim et al. (2006)	Study the influence of bondline thickness under tensile loading	Epoxy paste and film adhesives	0.12 and 0.13	1.55	20.0	Bondline thickness inversely proportional to joint strength; Dispersion of joint strengths greater for thinner adhesives
da Silva et al. (2009)	Quantify the effect of geometry in the strength of single-lap joints	Various ductile and brittle adhesives (epoxy and polyurethane)	1.0; 2.0; 3.0	0.5; 1.0 and 2.0	12.5; 25.0 and 50.0	Overlap increases lap shear strength; Thicker adhesive reduces lap shear strength; Thinner adherends increase lap shear strength; Higher adherend yield strength increases lap shear strength Higher adhesive toughness increases lap shear strength
Song et al. (2010)	Study the manufacturing methods and geometry impact on strength of composite bonded joints under tensile loading	Epoxy film adhesive	0.092	1.52; 4.57; 6.09 and 7.62	12.7; 19.1; 25.4; 38.1 and 50.8	Joint strength decreases with longer overlap; CCN best for lower adherend thickness; SEB better for higher thickness
Banea and da Silva (2009b)	Assess flexible adhesive performance in SLJs	One-component polyurethane hybrid adhesive High temperature thixotropic adhesive sealant	0.2 and 1 0.5 and 1	2.0 mild steel 3.0 Aluminum alloy	12.5; 25.0; and 50.0	Ductile joints with flexible adhesives increase strength linearly with overlap; Thicker bondlines reduce strength; Stiffness increases with overlap; Failure loads increase with overlap;
Ozel et al. (2014)	Examine the mechanical properties of joints with different adherends configurations (aluminum and carbon/epoxy composite)	Two-part paste epoxy adhesive	0.1	1.6; 3.2 and 4.4	12.5; 25.0 and 37.5	Stacking sequence affects failure mode; Longer overlap increases load capacity; Maximum stresses at overlap ends; Thicker adhesive leads to more severe nonlinear behavior
Akpinar and Sahin (2021)	Investigate static and fatigue strengths of SLJs of varying thicknesses in bending test	Structural epoxy adhesive with hardener	0.18	2.0; 3.0; 4.0; 5.0 and 6.0	7.5	Increase in adherend thickness increases damage load; Both adherends' thickness affects cohesion failure; Static bending load ratio increases with adherend thickness

Indeed, surface treatment of adherends plays a crucial role in achieving a robust and long-lasting adhesive joint. The optimum adhesion is in function on the following steps fulfillment:

- Thorough cleaning: removing all impurities like dust, lubricants, loose corrosion layers, and microorganisms is essential to create a clean bonding surface.

- Improving wettability: preparing a surface with favorable wettability and surface energy ensures the adhesive can spread evenly, which is crucial for a strong bond.

- Materials activation: ensuring the proper surface activation of the materials to be bonded.

As highlighted by Davies (2021), these steps not only ensure better adhesion but can also increase surface roughness, further enhancing the bond.

Designing an effective surface preparation strategy requires a thorough understanding of how the adherend, the adhesive surface, and the adhesive interact. Surface treatment stands out as a crucial parameter that can significantly affect joint strength and failure modes. Existing literature elucidates the interconnection between these two parameters.

To improve structural integrity, Davies (2021) emphasizes the imperative for interface/interphase stability to endure throughout the service life of the bonded structure. The increase of surface energy, facilitated through elevated roughness and chemical reactivity, directly extends the longevity and potency of bonded joints. However, it is important to highlight that the effectiveness of these surface treatments depends on the intrinsic attributes of the adhesive and adherend materials, along with their mechanical properties.

Literature has investigated the mechanical and microstructural properties, surface treatments, durability, and fatigue behavior of adhesive-bonded joints. Notably, Sorrentino et al. (2018) highlights that because they are so easy to apply, abrasive methods are frequently chosen for adherend surface treatment, particularly when it comes to repairing unbonded joints. Additionally, Cardoso et al. (2019) observed that abrasive techniques surpass alternatives like peel-ply in increasing the maximum load during tensile stress.

Among mechanical surface treatments, such as grit blasting, sanding, and peel-ply application, the research of Sorrentino et al. has presented their positive impact on enhancing the strength and toughness of adhesive joints. This investigation delved into the effects of these three specific surface treatments when applied to CFRP materials. The study involved the fabrication of SLJ specimens, utilizing film and paste adhesives. The results demonstrated that various adhesive types exhibited distinct responses to abrasive techniques.

For instance, in the case of film adhesives, peel-ply treatment demonstrated superior results for the lap shear test (10.14 MPa), leading to failure characterized by light-fiber tearing. On the other hand, paste adhesives performed better when sandblasted (6.57 MPa and 9.21 MPa), with the film adhesives producing less favorable results compared to the previous treatment (9.11 MPa). Notably, peel-ply treatment in the context of paste adhesives resulted in adhesive failures, in contrast to the prevalent light-fiber tear failures observed in other cases.

In addition, a recent study by Bechikh et al. (2022) explored composite surface treatments for adhesion purposes. This investigation focused on assessing the efficacy of sanding and sandblasting techniques in enhancing the adhesion quality of composites, with comparisons to peel-ply treatment. The study elucidated how these treatments impact surface properties. Notably, sandblasting creates higher surface roughness, wettability, and surface free energy. As a result, it significantly elevates the strength of bonded composite joints compared to the effects of peel-ply treatment. Similarly, sanding helps to increase the strength of the joint, although to a lesser extent compared to the impacts of sandblasting and peel-ply. It is important to note that the effectiveness of sanding introduces challenges, manifesting as fiber breakage and residual sand. These aspects introduce defects into the adhesive bond lines, necessitating a more rigorous cleaning process. These findings align with the outcomes of the previously discussed study.

On the other hand, Yang et al. (2019) provides a different viewpoint by investigating how adhesive tensile strength is affected by the direction of sanding. The findings show that random direction ablation of the specimens yields the best tensile strength. These results proved a strong correlation between the failure mode and the particular joint types and the effect of surface treatment on bonding strength. In specific, the failure mode seen in SLJs was a cohesion failure. In addition, it was found that the characteristics of the substrate surface were decisive for the results related to tensile strength.

As previously mentioned, regardless of factors such as adhesive loading, geometry, surface treatment, or the thickness of bonding and adherends, different failure modes in SLJ can occur. The specimen geometry, loading, and bond quality at each interface define the failure modes. To fully comprehend the characteristics of the adhesive and the joint under investigation, they must be described (Banea and da Silva (2009a)). When composites serve as adherends, these failures are documented and explained in ASTM D5573-99 standard (b). This source delineates and characterizes the various fracture modes observed in adhesive joints. Figure 2.5 summarises and illustrates the different failure modes.

The optimal fracture mode involves cohesion or adhesion occurring predominantly within one of the adherends. Such a scenario signifies the attainment of the highest joint strength. By analyzing the failure mode, it becomes possible to deduce whether the rupture occurred due to a weakness in the adhesive, the integrity of the adherend, or poor adhesion between the adherend and the adhesive layer.

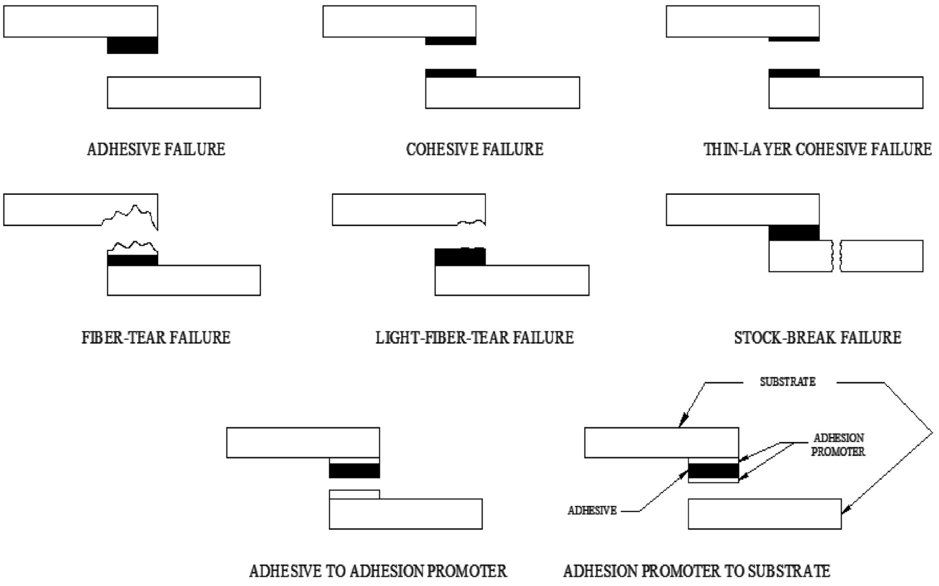

Figure 2.5: Representation of failure modes in composite to composite adhesive joints, from ASTM D5573-99 standard (b).

2.4 Fillers in epoxy resin systems

The geometrical parameters affecting adhesive joints were examined, particularly SLJs utilizing epoxy resin adhesives. These structural adhesives are recognized for their higher strength and are designed to bear substantial loads (Taib et al. (2006)). These epoxy adhesives can withstand fatigue cycles, influence damping mitigation, and have low electrical conductivity and chemical reactivity, offering a distinct advantage, avoiding galvanic corrosion when dissimilar materials are combined in an adhesive joint (Ebnesajjad (2011)).

Nonetheless, a notable drawback resides in the inherent rigidity of these cured resins, associated with their susceptibility to cracks. Their structural behavior depends significantly on factors including adhesive and adherend thickness, joint geometry, surface treatments, manufacturing processes and environmental conditions. Despite the optimization efforts, a comprehensive understanding is still not possible due to the unique nature of each adhesion system.

Recent studies have explored the properties of modifying the host resin by introducing additives to improve the mechanical properties of the adhesive joint, especially strength. This strategic improvement of a non-geometric parameter seeks to elevate the overall mechanical performance of adhesives. Consequently, the filler inclusion within an adhesive typically yields alterations in joint characteristics such as tensile or shear strength, elongation potential, electrical or thermal conductivity, and peel resistance, as reviewed by Taheri (2020). The final system combines the advantages of epoxy and filler material, as is the case with a composite.

In the study conducted by Gonçalves et al. (2022), they concluded that the selection and quantity of fillers within a system exercise a profound influence on the properties of the resulting epoxy composite. Fillers play a pivotal role in enhancing various aspects, including mechanical strength, resistance to corrosion, thermal stability, abrasion resistance, and electrical conductivity. In this context, the authors highlight nanomaterials, carbon fibers, metal particles, and ceramic materials as types of filler with the potential to be used to improve the properties of adhesives.

Carbon nanoparticles, in particular, have a distinct advantage over alternative nanofillers, as referred by Gu et al. (2013), making them the preferred choice for producing high-performance epoxy nanocomposites. The uniqueness of carbon nanotubes (CNTs) lies in their exceptional physical characteristics, such as high tensile strength, modulus, specific surface area, electrical and thermal conductivity, and lightweight.

Therefore, the present study focuses on carbon fillers to apply their potential to transform epoxy systems and, in turn, adhesive systems.

2.4.1 Effect of carbon nanomaterials in epoxy resins

Carbon nanomaterials have obtained significant attention due to their advantageous properties in mechanical and thermal domains. These advantages encompass thermal conductivity, flame retardancy, mechanical stability, electrical conductivity, and biocompatibility.

In the comprehensive study by Gonçalves et al. (2022), various crystalline allotropes of carbon are highlighted. These include graphene, graphite, CNTs, fullerene, and diamond. Carbon’s unique ability to form covalent bonds with itself results in diverse structural arrangements, each possessing distinct physical properties.

Graphene is a carbon allotrope characterized by an arrangement of carbon atoms in a monolayer honeycomb crystal mesh with exceptional attributes such as high aspect ratio, specific surface area, Young’s modulus, fracture strength, thermal conductivity, and electron mobility. Graphene and its derivatives are particularly promising for applications such as sensors, transparent conductive films, batteries, supercapacitors, solar cells, and polymer nanocomposites. In contrast, graphite consists of interconnected graphene layers, forming expanded graphite or graphene oxide. Another configuration of carbon is fullerene, a carbon molecule that adopts hollow spherical, ellipsoidal, and tubular shapes, as described in Liu et al. (2018).

One example of fullerene are CNTs, which correspond to cylindrical fullerenes, sharing structural similarities with graphite. They are composed of stacked hexagonal graphene sheets, occasionally incorporating pentagonal (or heptagonal) rings within their structure. CNTs are classified into single-walled carbon nanotubes (SWCNT) and multi-walled carbon nanotubes (MWCNT), with the latter further subdivided into double-walled carbon nanotubes (DWCNT) based on the number of graphene hollow cylinders in their composition. According to Liu et al. (2018), MWCNTs exhibit stiffness and rigidity due to their complex geometry, resembling rod-like structures, while SWCNTs demonstrate flexibility due to their one-wall layer. Figure 2.6 represents a visual description of the crystalline mesh of the various carbon nanomaterial geometries previously discussed.

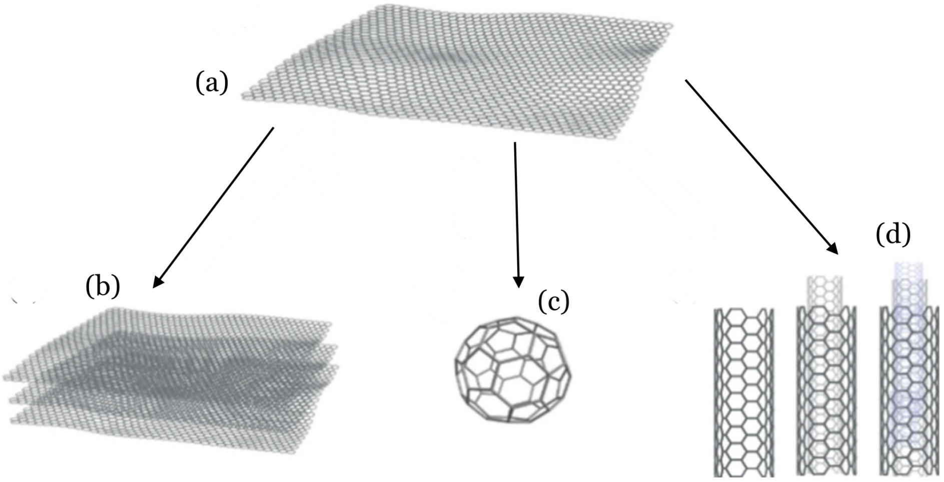

Figure 2.6: Graphene and derivate allotropic forms. (a) Graphene. (b) Graphite; (c) Buckyballs. (d) Carbon nanotubes (SWCNT, DWCNT, and MWCNT, from left to right). From Gonçalves et al.'s work.

Table 2.4 overviews the main properties of carbon nanomaterials. This compilation was done based on the extensive studies conducted by Liu et al. (2018) and Khan et al. (2021).

Table 2.4: The properties of typical carbon nanomaterials, from Liu et al. (2018); Khan et al. (2021).

Filler	**Typical diameter** (nm)	**Density** (g/cm^3)	**Specific surface area** (m^2/g)	**Electrical conductivity** (S/m)	**Thermal conductivity at room temperature** ($W/m \cdot K$)
Fullerene	0.7	1.7	42 - 85	10^{-3}	0.4
SWCNT	0.4 - 6.0	1.3 - 1.5	10 - 20	10^6	6000
DWCNT	5	1.5	10 -20	10^6	3000
MWCNT	2 - 20	1.8 - 2.0	10 - 20	10^6	2000
Graphene		2.2	2675	6×10^5	5000

CNTs are widely acknowledged for their profound influence on enhancing both mechanical and electrical properties in a range of materials (Zhao and Barrera (2010)). This enhancement primarily arises from their higher conductivity and aspect ratio, which improve the overall material characteristics. A comparison of CNTs with graphene, based on the values presented in Table 2.4, reveals their superior electrical conductivity and lower density.

As pointed out by Aradhana et al. (2020), CNTs are exceptional nanofillers for improving the properties of polymers, adhesives, and composites. The CNTs have outstanding strength, which exceeds that of steel by around 100 times, and an impressive modulus (in the TPa range). They also have a high surface-to-volume ratio (around 1000), excellent thermal conductivity (ranging from 3000 to 3500 $\mathrm{W/m \cdot K}$), extraordinary electric current-carrying capacities (approximately 1000 times greater than copper) and remarkable thermal stability (with a melting point of 3073 K in vacuum). These conclusions are also supported by Santamaria et al..

However, obtaining the desired mechanical properties requires careful consideration of various factors. These factors include the selection of the epoxy resin, the optimal combination of fillers, and precise manufacturing procedures. Manufacturing procedures are of paramount importance due to the unique characteristics of CNTs. These carbon fillers have a larger surface area and are predisposed to strong Van der Waals forces, leading to particle agglomerations. Therefore, achieving a well-dispersed CNT distribution is crucial. This dispersion can be accomplished through various methods, including high shear mixing, ultrasonication, the utilization of surfactants, acid oxidation of CNTs, and other chemical techniques, as reviewed in Aradhana et al.'s work. Several methodologies will be discussed in detail later in this section.

2.4.2 Effect of CNTs in mechanical properties of epoxy materials

One highly effective approach to enhance the mechanical properties of epoxy materials, covering factors like toughness, strength, impact resistance, brittleness, and stress to failure, is the incorporation of carbon nanofillers into epoxy composites. This subsection reviews a few methods reported in the literature to understand how CNT reinforcement affects the mechanical response of epoxy materials.

In a study to improve adhesive reinforcement, May et al. (2010) investigated a composite system involving gamma-alumina ($\gamma - Al_2O_3$) and MWCNTs to bond aluminum adherends. The objective was to enhance adhesive lap shear strength. With 0.05 wt% MWCNTs and 0.71 wt% of $\gamma - Al_2O_3$, promising results were achieved. The reinforcement increased adhesive lap shear strength from 10 MPa to 24 MPa, compared to pure epoxy. Furthermore, the thermal stability increased, suggesting the potential use of this adhesive in more demanding environments.

The promising results of the prior study, which highlighted improvements in mechanical and thermal characteristics, prompted further research into reinforcing epoxy systems. One study conducted by Gkikas et al. (2012) focused on formulating an MWCNT/epoxy nanocomposite with varying ratios of CNTs. Compared to previous work, this study increased the reinforcement load, exploring cases with 0.5 wt.% and 1 wt.% CNTs. When comparing neat epoxy films in SLJ specimens incorporating 0.5 wt.% CNTs, they observed a remarkable 50 % enhancement in adhesion efficiency. Similarly, a study by Wernik and Meguid (2014) aimed to optimize the loading reinforcement to identify the values that would optimize the epoxy system. Their experimental results revealed the existence of a critical CNT concentration, typically around 1.0–1.5 wt.%, which yielded the most substantial improvements in mechanical properties. However, concentrations surpassing this critical value led to property degradation, decreasing below the levels of pure epoxy.

This phenomenon is attributed to CNT agglomeration, which limits the CNT concentration in epoxy systems and results in property degradation. Notably, tensile adhesive tests demonstrated an impressive 54 % improvement compared to pure epoxy cases.

Jojibabu et al. (2016) carried out a more comprehensive investigation into the reinforcement of epoxy adhesive joints. Their study delved into the rheological properties, thermal stability, and lap shear strength of epoxy adhesive joints reinforced with various carbon nano-fillers, including MWCNTs, graphene nanoplatelets (GNP), and single-walled carbon nanohorns (CNH). Their research unveiled a significant improvement in lap shear strength, with a remarkable 53 % increase achieved through the addition of just 1 wt.% of CNTs when compared to pure epoxy. However, it is noteworthy that the strength of joints with high filler content, exceeding 1 wt.%, experienced a limitation. At these elevated filler fractions, a mixed mode (cohesive and adhesive) failure mechanism became prevalent, leading to a decrease in lap shear strength, even falling below the strength of pure epoxy joints. These findings align with prior studies, particularly the research conducted by Wernik and Meguid (2014).

In the study conducted by Aradhana et al. (2018), the researchers developed an epoxy-based adhesive that incorporated CNTs and nano clay. Their goal was to create structural adhesives with improved properties. When compared to pure epoxy samples, they discovered that the optimal shear strength was achieved with a CNT loading of 1 wt.%, leading to a significant 48.2 % improvement. However, they observed that mechanical properties started to degrade at CNT loadings beyond this concentration. The authors propose that the enhancement in shear strength (8.21 MPa) at the 1 wt.% loading is primarily due to the improved interaction between CNTs and the epoxy resin, driven by the high aspect ratio of CNTs. In contrast, the degradation observed at higher loadings is attributed to filler agglomeration. When the fillers clump together, it restricts the effective transfer of load, initiates cracks, and leads to damage propagation. Similar findings of degradation due to particle aggregation were observed in a study by Ayatollahi et al. (2016). In their research, they found that the aggregation of particles, which included CNTs, led to a reduction in shear strength and a decrease in elongation at the point of failure. These aggregations acted as local stress concentrations, ultimately functioning as defects rather than reinforcements.

In both works, the optimal adhesive reinforcement levels were found at 1 % and 0.5 % of CNTs, respectively. Test results consistently demonstrate that introducing various nanomaterials into epoxy resin enhances the shear strength of the final product. For instance, neat epoxy exhibited a shear strength of 5.54 MPa in Aradhana et al. (2018)'s work. Moreover, Ayatollahi et al. (2016) also mentioned an increase in the energy joint absorption and a 20.1 % improvement in elongation to failure compared to unreinforced adhesive. The addition of 1 wt.% CNTs to the epoxy increased shear strength by 48 %, primarily due to improved adhesion resulting from CNT bridging between epoxy matrices, facilitated by their high aspect ratio.

The impact of MWCNTs on the fatigue characteristics of peel-loaded adhesive joints in epoxy-based adhesives was examined in a study by Zielecki et al. (2017). This research aimed to assess how the reinforcement affected the fatigue performance of these adhesive joints under various loads. The fatigue strength tests demonstrated a notable enhancement in the fatigue lifetime of adhesive joints when MWCNTs were introduced as fillers in epoxy adhesives in a weight ratio of 1 %. Epoxy resins exhibited an increase in fatigue strength of approximately 12.6 % and revealed a substantial increase in fatigue lifetime. One resin case tested experienced a 106.8 % increase from 362500 to 749600 cycles. Another case reported a 69.3 % increase. The enhancement in mechanical properties is attributed to the reinforcement effect of MWCNTs at a molecular level. This reinforcement improves contact between the fillers and the epoxy resin, resulting in better bonding within the adhesive material. Consequently, this phenomenon effectively limits the propagation path of cracks within the adhesive, contributing to the increased mechanical performance of the material.

The studies previously reviewed consistently found that concentrations of around 0.5 % and 1 % of CNTs tend to yield optimal results, with higher concentrations resulting in the aggregation of CNTs (Wernik and Meguid; Jojibabu et al.; Ayatollahi et al.; Aradhana et al.). These CNT agglomerates can introduce defects within the epoxy system, acting as weaknesses. As reported by Jojibabu et al. (2016), if these agglomerations form in the epoxy system, the lap shear strength of an adhesive joint can decrease to a level even lower than that of pure epoxy samples.

Indeed, the dispersion methodology is a crucial factor that can significantly impact the mechanical properties of epoxy systems. As described by Wernik and Meguid (2014), carbon nanotubes aggregate into ropes or bundles due to intermolecular Van der Waals interactions. These relations can lead to the formation of entangled CNT networks or agglomerates, which do not contribute to the desired mechanical performance in CNT-based systems. Proper dispersion techniques are essential to overcome these issues and fully utilize the mechanical potential of carbon nanotubes in epoxy composites.

Various solutions have been documented in the literature to ensure a satisfactory dispersion and avoid the fillers' agglomerations in the resin. Hence, the mixing of MWCNTs into the adhesive material is a critical step in the overall process. Chong et al. (2016) highlighted in their work the substantial dependence of Young's modulus on dispersion quality. However, the fracture energy is independent of the degree of dispersion.

Numerous studies have employed techniques to de-agglomerate CNT particles, with variations of the sonication technique being the most common. In the study conducted by Romate et al. (2018), they explored the addition of CNTs in adhesive films alongside a dispersion procedure involving sonication in an aqueous media using sodium dodecyl sulfate (SDS) as a surfactant in varying concentrations to achieve effective dispersion. A sonication frequency of 1 kHz for 20 minutes yielded an effective CNT dispersion, and the surfactant proved its efficacy in disaggregation. The CNT dispersion was in water at a fraction of 0.1 wt.%. Subsequently, this dispersion was sprayed onto the surface of the adhesive film. When investigating surfactant impact on lap shear strength, they verified that the value remained largely unaffected at low SDS concentrations (0.1 and 0.25 wt.%). However, at the highest SDS content (1 wt.%), lap shear strength decreased due to the surfactant's activity. Consequently, the surfactant exhibited characteristics that introduced defects into the adhesive. Similarly, Aradhana et al. (2018) employed direct sonication in epoxy with CNTs. In another approach, Ejaz et al. (2022) employed acetone for de-agglomeration and subsequently subjected the mixture to sonication for 30 minutes at a frequency of 40 kHz.

Given their findings, Wernik and Meguid (2014) concluded that the ultrasonication dispersion technique is effective only up to a CNT concentration of 1.5 wt.%. Beyond this concentration, the viscosity of the base resin becomes saturated by the presence of CNTs, leading to significant processing challenges. The increasing amount of CNTs and their intermolecular interactions restrict the mobility of polymer chains, rendering it more difficult for the ultrasonication probe to apply the necessary shear stresses.

Moreover, the dispersion mechanism is significantly influenced by whether it occurs within the resin or with the hardener, as studied by Shokrian et al. (2019). This research underscores the differences in tensile and shear strengths observed in structural lap joints with adhesives manufactured using these two distinct dispersion methods. The study concluded that the resin dispersion method increased shear strength and offered a more effective dispersion mechanism. These findings justify the prevalence of resin-phase dispersion methods in the reviewed methodologies.

Ejaz et al. (2022) experienced a different methodology for improving mechanical properties in their study, which consists of the functionalization of CNTs. By comparing non-functionalized and functionalized MWCNTs, they concluded that the first case results in lower values of elastic and tensile strength compared to functionalized MWCNT reinforcement in epoxy adhesive systems. The insertion of MWCNTs in epoxy contributed to an enhanced plastic response within the modified adhesive compared to pure epoxy samples, consequently elevating its toughness characteristics to around 71 %. For this case, the functionalization was realized with carboxylate (COOH) and amine (NH_2) at MWCNTs loadings of 0.25, 0.5, 0.75, and 1 wt.%. The filler's addition into the epoxy system resulted in an improvement in the joint's strength around 60 % for SLJ and 31 % for DLJ for a reinforcement of 1 wt.% CNTs.

Upon reviewing these studies, it becomes evident that MWCNTs at lower filler concentrations directly correlate with increased strength and lifespan of adhesive joints. However, at concentrations above 1 wt.%, especially with functionalized MWCNTs, originate agglomerates, leading to a strength reduction, sometimes lower than pure epoxy resin. These aggregates can act as stress concentration points that promote crack growth. Hence, achieving the desired mechanical properties necessitates meticulous consideration of proper carbon particle dispersion.

2.5 Electrical conducticity properties of CNTs in epoxy materials

In general, adhesives behave as electrical insulators. Conductive adhesives are composite materials of solid conductive fillers dispersed within a non-conductive polymer matrix. As referred in Anderson and Macon's work, adhesives can become conductive by adding electrically conductive fillers like carbon materials, nickel, and silver. Conductive adhesives offer a straightforward and environmentally friendly solution for various electrical applications, offering a good response in the electronics and microelectronics industries. Aradhana et al. (2020) categorizes conductive fillers into four distinct material types: metal fillers (Sancaktar and Bai (2011)), carbon-based fillers, ceramic fillers, and metal-coated fillers.

Epoxy resins typically exhibit low electrical conductivity. However, this property can be significantly improved by establishing a three-dimensional conductive network inside the material. This network forms when conductive fillers reach a critical concentration in the matrix called the electrical percolation threshold (EPT). In the EPT, the fillers establish interconnected pathways within the matrix, enabling efficient electron transport. Remarkably, even at relatively low concentrations, the addition of carbon nanoparticles, with their low EPT, can substantially improve the electrical conductivity of epoxy matrix (Santamaria et al. (2013); Aradhana et al. (2020); Gonçalves et al. (2022)).

To improve the adhesives' electrical conductivity, current research efforts are mainly centered on reducing the EPT in CNTs' nanocomposites. These studies aim to reach an optimum balance by achieving a lower filler concentration that can produce an electrical response without compromising mechanical properties.

In a study by Gu et al. (2013), they created high-performance epoxy nanocomposites by incorporating polyaniline (PANI)-stabilized MWCNTs at varying loadings. Notably, when they used a loading of 1.0 wt.% of functionalized MWCNTs, the resulting epoxy polymer nanocomposite displayed a remarkable increase in electrical conductivity of approximately 5.5 orders of magnitude when compared to pure epoxy case. This study also established the EPT at a filler loading of 1.0 wt.%.

Table 2.4 presents the conductivity properties of commonly utilized electrically conductive carbon nanofillers, which include SWCNTs, MWCNTs, and graphene. It is evident from the table that CNTs exhibit higher conductivity values in comparison to graphene and fullerene fillers. This characteristic positions CNTs as a favorable choice as fillers for electrically conductive adhesives.

2.5.1 Percolation theory and electrical percolation threshold

The concentration, form, size, purity, and structure of conductive nanoparticles, as well as their interactions with the polymer matrix, all affect the electrical conductivity of polymer nanocomposites. A significant phenomenon in these materials is the transition from insulating to conducting behavior at a certain filler ratio. This fundamental change is rooted in the principles of percolation theory and EPT, which play a vital role in understanding the conductivity of composite materials.

Percolation theory elucidates how electrical conductivity changes in three distinct stages as conventional conductive filler particles are progressively incorporated into insulating polymers, as elucidated in the works by Alamusi et al.; Taherian; Khan et al.. Initially, at low filler concentrations, the composite's electrical conductivity closely mirrors that of the polymer matrix (Figure 2.7, **Part 1**), owing to the considerable distance between particles. As clusters form and inter-particle connections emerge due to interactions among conductive fillers, conductivity gradually increases until a critical filler concentration corresponds to the EPT. This filler concentration marks the beginning of a percolation network or conductive path.

With the establishment of these pathways, the composite becomes conducive to electric charge flow, effectively behaving as a conductor. Beyond the percolation threshold, electrical conductivity escalates rapidly, driven by the creation of threshold-conducting bridges (Figure 2.7, **Part 2**). This results in a fast increase in conductivity.

Continuing further, the conductivity levels at a value lower than that of individual filler particles. This plateau presents the formation of multiple conductive paths within a network structure (Figure 2.7, **Part 3**). This description and Figure 2.7 summarise the relationship between percolation theory and EPT in the conductivity evolution in polymer composites with the representation of the filling ratio in the circles for each part of the curve.

Taherian (2014) mentioned that the electrical conductivity of a nanocomposite material (σ) in its initial stage (**Part 1**) can be estimated using the mixture rule. This rule, as presented in Equation 2.1, takes into account the volume fraction of the filler (F_f) and the matrix (F_m), as well as their respective electrical conductivity (σ_r and σ_m). This equation is valid before the percolation threshold point, as illustrated in Figure 2.7.

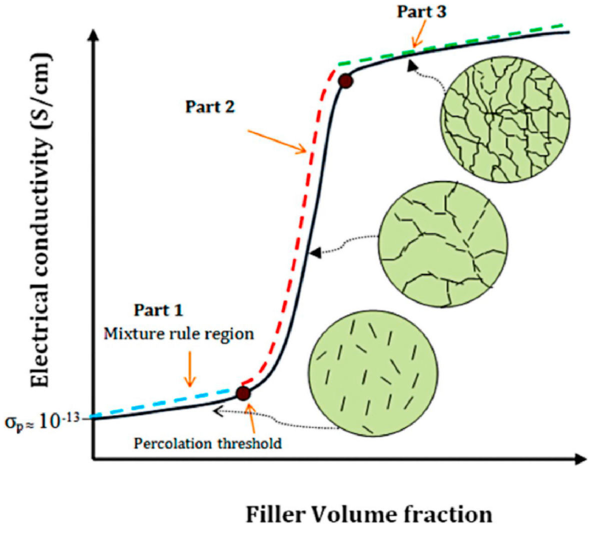

Figure 2.7: Three-part description of the composite conductivity curve versus filler volume fraction, from Taherian (2014).

$$\sigma = F_f \cdot \sigma_r + F_m \cdot \sigma_m \quad (2.1)$$

Another relationship appears beyond the EPT, as documented in the study of Khan et al.. Equation 2.2, which represents the scaling law of percolation theory, describes the relation:

$$\sigma \propto (\phi - \phi_c)^t \quad (2.2)$$

This equation incorporates various parameters, including ϕ_c, which represents the filler amount at the percolation threshold, ϕ, the volume fraction of the filler, σ, the electrical conductivity of the composite, and t, the critical exponent related to the dimensionality of conductive networks (Vertuccio et al. (2016); Spinelli et al. (2020)). In this equation, the polymer conductivity is proportional to the relationship between the EPT and the filler loading. Nan et al. (2010) and Khan et al. (2021) identified that the critical exponent t takes values approximately 1.1 - 1.3 for two-dimensional (2D) and 1.6 - 2.0 for three-dimensional (3D) conductive networks, respectively, and is generally applicable only near the percolation threshold.

Bauhofer and Kovacs (2009) conducted a significant study by reviewing experimental and theoretical research on the EPT of CNTs in polymer composites. Based on the summary provided by the aforementioned authors, Table 2.5 presents various methodologies related to dispersion, treatment, aspect ratio, and de-agglomeration solutions, offering an overall perspective on how these parameters influence the EPT and conductivity of nanocomposites of CNTs and epoxy resin. Some studies include the critical exponent related to the dimensionality of conductive networks.

An extensive summary of the different aspect ratios, dispersion techniques, and production processes is provided in the Table 2.5. Notably, the results for the EPT exhibit significant variability, ranging from 0.0021 to 3.5 wt.%. Furthermore, the electrical conductivity for the nanocomposites demonstrates values between 1×10^{-5} to 5×10^{-1} $\mathrm{S/m}$. According to the authors' suggestions, the aspect ratio is a determining factor in the final electrical conductivity of the nanocomposite. In particular, the aspect ratio seems to have a more pronounced influence on the final electrical properties compared to the possible effect of the dispersion method. One question raised by Bauhofer and Kovacs (2009) is that well-optimized dispersion techniques can lead to an effective reduction in EPT for epoxy resin/CNTs nanocomposites. However, it is essential to recognize that while dispersion optimization is important, it may not be the central factor that predominantly shapes the electrical properties of nanocomposites. This observation should not reduce the importance of studying and applying optimal dispersion methods. Achieving a well-balanced compromise between electrical and mechanical properties remains a critical consideration.

2.5.2 Electrical conduction mechanisms in CNTs nanocomposites

The electrical conduction mechanism within CNT pathways is crucial for understanding the conductivity of polymer composites reinforced with conductive fillers. Figure 2.7 illustrates the evolution of conductivity, with green circles representing additional fillers in darker colors, symbolizing the formation of electrical paths at increasing filler contents in polymeric matrices.

The enhanced conductivity in polymeric materials, aided by conductive particles, establishes electrical paths that allow the flow of electric current. This conductivity phenomenon in CNTs is governed by two distinct electrical mechanisms, as explained in the work of Obitayo and Liu (2012): direct contact between CNTs and the tunneling effect. These mechanisms facilitate electrical conduction between adjacent CNTs within polymeric matrices.

In the tunneling effect, as described by Wang and Chung (2013), adjacent conductive particles must be separated by small distances, typically on the order of 10^{-1} nm. This separation enables what is known as percolative conduction, where electrons can tunnel from one particle to another, facilitating the overall flow of electric current. Conversely, direct contact permits an electric charge to go directly between successive CNTs. Figure 2.8 illustrates these two phenomena. An insulating matrix can be converted into an electrically conductive system using an efficient network of CNTs. This mechanism shows how important is a good particle distribution within the polymeric matrix.

Table 2.5: Summary of the experimental parameters of epoxy matrices filled with MWCNT, adapted from Bauhofer and Kovacs (2009).

Matrix	**Filler**	**Treatment**	**Aspect Ratio**	**Solution**	**Dispersion**	ϕ_C **(wt.%)**	**t**	σ_{max} **@ Filler loading** (S/m) | **(wt.%)**	**Reference**
Epoxy	MWCNT (CVD)	-	200	-	Heat sheared	0.0021	1.78	1×10^{-4} | 0.01	Martin et al. (2004)
Epoxy	MWCNT (CVD)	-	1000	-	Stirred, heat sheared (slowly)	0.011	1.7	5×10^{-1} | 1	Kovacs et al. (2007)
Epoxy	MWCNT (CVD)	-	100	C_2H_6O	Sonicated, stirred	0.04	-	5×10^{-1} | 0.15	Sandler et al. (1999)
Epoxy	MWCNT (CVD)	-	1000	-	Stirred	0.40		2×10^{-2} | 1	Li et al. (2007)
Epoxy	MWCNT (CVD)	-	400	CH_4	Stirred	0.50	-	5×10^{-2} | 3	Bai and Allaoui (2003)
Epoxy	MWCNT (CVD)	HNO_3	20	C_3H_6O	Sonicated, stirred	3.5	-	1×10^{-5} | 8	Cui et al. (2003)
Epoxy	MWCNT (CVD)	-	715		Sonicated, stirred	0.25	-	1×10^{-5} | 1	Ayatollahi et al. (2011)

CVD - Chemical vapor deposition; C_2H_6O - Ethanol; HNO_3 - Nitric acid ; CH_4 - Methane; C_3H_6O - Acetone

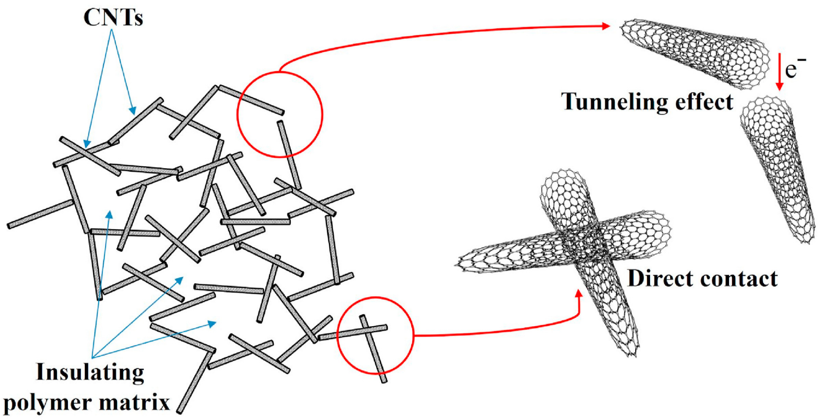

Figure 2.8: Schematic illustration of direct contact and tunneling effect in an electrically conductive nanocomposite reinforced with CNTs, from Khan et al. (2021).

Understanding the electrical conduction mechanisms in these CNT-reinforced nanocomposites reveals their potential for sensing in mechanical applications. This electrical property could facilitate the development of piezoresistive sensing structures capable of detecting stress and strain deformations, making them highly suitable for structural health monitoring (SHM) applications.

2.6 Introduction to piezoresistive sensing for structural health monitoring

Structural health monitoring (SHM), as introduced by Balageas et al. (2006) in his work, aims to provide continuous diagnostic information about the ”health” of a structure’s materials, components, and overall assembly throughout its operational life. It involves assessing the structure condition in relation to its original design parameters, which can evolve due to variable factors such as wear and tear induced by use, environmental influences and unexpected events.

Completing the historical record of the structure by integrating the temporal dimension of monitoring makes it feasible to forecast the behaviour of individual components, including the development of damage and remaining lifespan. As mentioned by Rana and Fangueiro (2016), these diagnostic methods are especially interesting for use in aerospace composite materials and structures. This technology makes it possible to monitor structural degradation online, enabling immediate maintenance actions that reduce maintenance costs and increase the safety of aerospace structures.

This concept takes inspiration from the human body, which relies on a network of sensors to provide continuous information about its health in response to environmental stimuli. SHM involves deploying a network of sensors across a structure and subsequently processing the acquired data to inform future decisions and actions, similar to the central nervous system in living organisms, which processes this sensory input and initiates appropriate responses (Kang et al. (2006)). An intelligent structure is needed to achieve this goal of continuous monitoring that can interact with its environment by collecting information, including load conditions (Nauman (2021)).

The core objective of SHM is to establish an integrated diagnostic system, utilizing a sensor array to monitor structural conditions and detect any signs of damage while the structure is in operation. Qing et al. (2006) detail how this diagnostic system incorporates a sensor network, portable diagnostic hardware, and data analysis software. The software uses diagnostic algorithms that distinguish between electrical signals that indicate damage or safe operation. In addition, as mentioned by Balageas et al. (2006), prognostic algorithms can predict the remaining lifetime of a structure based on the diagnostic analysis. Given its inherent complexity, any SHM system encompasses a multidisciplinary approach in terms of both its objective and implementation.

Currently, Spinelli et al. (2020) has highlighted that structural monitoring predominantly relies on non-destructive inspection (NDI) and periodic reviews within the aeronautical domain. Despite the effectiveness of various NDI techniques for aircraft inspection - such as visual inspection, ultrasonic inspection, eddy current, acoustic emission radiography, thermography, and shearography - many of these methods are manual, requiring the aircraft to be on the ground, resulting in time-consuming and costly procedures. Consequently, there is a pressing need to reduce the flight hours spent on inspections, which presents a challenge for aviation operators.

On the other hand, Wang and Chung (2006) found that although techniques like ultrasonic testing and acoustic emission allow damage detection, they cannot detect stress or strain. Hence, a combination of various NDI methods is often necessary to monitor structural integrity and ensure reliability.

The conclusions drawn by Vertuccio et al. (2016) and Spinelli et al. (2020) emphasize that the existing methods require suitable internal systems integration. When coupled with analytical methodologies applied to mechanical tests, these systems enable the estimation of fatigue-induced damage. The strain sensing integration into composite structures is a promising solution to these problems, offering better monitoring of the structure's health, enhanced durability, higher reliability, and reduced costs associated with inspections and maintenance for composite structures.

In this context, unlike conventional non-destructive testing approaches that require planned interventions and offline periods for the structure, Nauman (2021) highlighted the capability of SHM to be performed while the structure is still in service. This capacity enables continuous monitoring of structures during their operational use, eliminating the need for downtime.

To meet the demand for real-time structural assessment and damage identification, the specific enhancements integration into composites can offer additional functionalities, resulting in intelligent composites sensing capacities. These multifunctional composite structures can sense or actuate, making them sensitive to variations in their structural integrity. The adoption of intelligent structures and materials has introduced a new way of monitoring structural health, namely CNTs and graphene as nanofillers, which have self-sensing properties.

A comprehensive review undertaken by Rocha et al. (2021) has provided a comprehensive overview of the various sensor types employed in structural health monitoring. This review delves into fiber optic, piezoelectric, and piezoresistive sensors, elucidating their attributes, operational principles, embedding techniques, and interactions with host materials. The development of SHM systems tailored for aerospace composites are explored, underscoring the significance of compact sensors, lightweight, durable, energy-efficient, cost-effective, and reliable. The essential parameters that sensors utilized in SHM should contain are emphasized, including accurate tracking of structural damage regardless of environmental changes, dependable signal transmission, minimal impact on the host structure, longevity throughout the structure's operational life, and ease of handling, attachment, integration, and operation.

As highlighted by Avilés et al. (2018), piezoresistive sensors offer several advantages over piezoelectric sensors. They are particularly sensitive to changes in electrical resistance when subjected to mechanical effects, making them valuable for SHM applications. In contrast, Wang and Chung (2006) emphasized that electrical resistance measurements can enable the simultaneous sensing of stress and strain, and these factors can have distinct effects on electrical resistance.

Based on the prior section, where CNTs incorporation into polymers results in conductive nanocomposites, the significance of this electrical property for investigating piezoresistivity in such materials, especially in the context of SHM applications is appreciated. According to a detailed description by Duan et al. (2020), strain sensors based on CNTs can be made by dispersing CNTs in a polymer matrix, directly depositing CNT films or transferring CNT matrices with specific designs to substrates. The sensitivity can be adjusted through control aspects such as the filler load, the functionalization of the filler, the quality of the dispersion, the manufacturing processes, the interaction between the CNTs and the polymers, and the configuration of the network.

The concept of EPT, mentioned earlier, can vary depending on the specific polymeric matrix used and the reinforcing filler. This concept underscores the importance of considering different matrices when determining percolation thresholds. Additionally, achieving effective filler dispersion within the matrix is crucial to ensure improved electrical properties for sensing applications.

In this section, piezoresistive sensing is discussed in detail, with an emphasis on how epoxy-CNT nanocomposite systems function as multifunctional materials with sensing properties in a range of structures, such as adhesive joints, to anticipate damage and react to cyclical stress and strain stimuli.

2.7 Piezoresistive effect for application in sensing structures

Rana and Fangueiro (2016) identified that self-sensing composites usually work on the piezoresistive principle, which results in the variation of electrical resistance with strain or damage. Studying the piezoresistive phenomenon in polymers necessitates ensuring a certain level of conductivity, which is essential for creating functional strain sensors. The primary objective of piezoresistive sensors is to establish a correlation between changes in electrical resistance induced by mechanical stresses and the resulting structural deformations. This correlation is achieved by utilizing the material itself as a sensor. As highlighted by Georgousis et al. (2015), this approach offers significant advantages, including cost-effectiveness, applicability to different structural materials, and mechanical properties conservation. The central concept revolves around utilizing changes in electrical resistance due to a reduction in electrical contact points between the conductive fibers, particles, or nanotubes for tensile loading to identify the initiation, nature, and progression of potentially damaging levels of deformation. The opposite is when the composite is subjected to compressive loading, increasing the contact points between reinforcing particles.

The concepts introduced in section 2.5, such as the EPT, tunneling effect, and direct contact between CNT particles, play a crucial role in understanding how nanocomposites with electrical properties can work as strain sensing structures. These notions are important in comprehending the working principles of piezoresistive sensing and their application in predicting strain deformations in various structures.

The piezoresistive properties of materials arise from the reconfiguration of the conductive network embedded within the polymeric matrix. As discussed earlier, different filler fractions in nanocomposites result in varying electrical networks. Obitayo and Liu (2012) delved deeper into the phenomenon of CNT networks and described two main resistance mechanisms in more detail. The first is intrinsic resistance, denoted as R^{CNT}, and the second is intertube resistance. The intertube resistance is related to the previously mentioned electrical conduction phenomena: contact resistance, R^{C} (the electrical resistance between CNTs that are physically in contact), and tunneling resistance, R^{T} (the electrical resistance between CNTs that are separated by a small gap). Variations in the intertube resistance are the primary factors affecting the piezoresistive effects of the CNT network.

Hu et al. (2008) described both intertube resistance behaviors affecting the piezoresistivity of a nanocomposite system. The first phenomenon concerns the rupture of the conductive network or the loss of contact between these fillers. When deformation occurs, the arrangement of the particles changes, and the contact of neighboring CNTs changes, leading to interruptions in the conductive paths. The second phenomenon involves the tunneling effect, which is influenced by the distances between these conductive fillers. The research presents that even an increase of $10\ \mathrm{nm}$ in the average distance between two CNTs can lead to a substantial decrease in the tunneling current, which increases the electrical resistance exponentially. As Spinelli et al. (2020) highlights, if plastic deformation leads to an increased separation between neighboring CNT aggregates, typically above $2\ \mathrm{nm}$, the tunneling effect becomes less effective. This situation reduces the effectiveness and results in an overall increase in electrical resistance. This effect is particularly significant because it enables the detection of structural damage in materials that might otherwise go unnoticed.

These changes in the electrical network result in variations in conductivity, which, in turn, modify the inherent piezoresistive characteristics of the nanocomposite material, as exemplified in the research conducted by Vertuccio et al. (2016). Consequently, these variations in conductivity can work as sensing mechanisms to detect deformations in nanocomposites. The increase in the overall electrical resistance of the sample is in line with the expected behavior of conductor-filled polymer subjected to tensile stress.

Figure 2.9 illustrates the evolution of contacts between fillers for different loading conditions. In tension, the particles are separated, increasing the electrical resistance. The opposite scenario is observed for compression, where particles are getting closer. The contacts' number increases, improving electrical conductivity. The $0\ \%$ strain case represents an expected reinforcement distribution within the matrix.

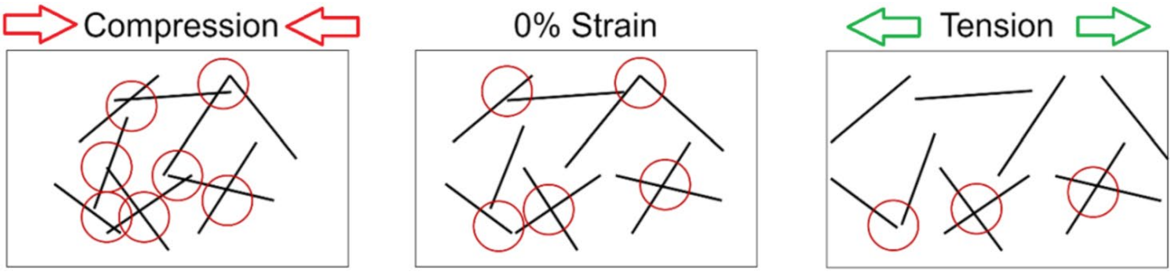

Figure 2.9: Evolution of the number of conductive pathways (circles) between CNTs (solid lines) in a polymer under mechanical load (compression and tension), adapted from Bregar et al. (2020).

The gauge factor (GF) is a critical parameter to assess the sensitivity of the piezoresistive sensor. This factor quantifies the linear piezoresistive sensitivity, considering the linear relationship between the relative change in electrical resistance and the applied strain. It provides a quantitative measure of how responsive the system is to alterations in strain. The GF calcule is presented in Equation 2.3. This value is essential for assessing and determining how sensitive sensor's systems respond to different strain levels. There is a discussion on this sensitivity parameter in the works of Vertuccio et al. (2016), Spinelli et al. (2020) and Irfan et al. (2021).

$$GF = \frac{\Delta R}{\varepsilon R_0} \quad (2.3)$$

In this equation, $\Delta R = R - R_0$ denotes the variation in electrical resistance concerning the electrical resistance measured in a resting state, indicated as R_0. The term ε stands for the measured strain. Duan et al. (2020) highlights the necessity to specify the strain range for which the GF is determined to avoid unclear interpretations.

Nanocomposites of epoxy reinforced with CNTs show a decreasing trend in literature for GF as the percentage of fillers increases. In Spinelli et al.'s work, they found a higher value of GF (3.9) for low reinforcement concentrations, close to the percolation threshold. In their specific case, this value is reported to be 0.3 wt.% CNTs.

However, it is important to consider the practical implications of operating close to the EPT. As highlighted by Avilés et al. (2018), working near the EPT can result in a noisy electrical signal and present challenges in terms of instrumentation. To overcome this limitation, researchers in the piezoresistive polymer composites field have predominantly chosen to work with filler concentrations significantly above the EPT. This approach enables them to achieve electrical resistances in the range of $\mathrm{k\Omega}$-$\mathrm{M\Omega}$, which are more practical and easier to manage.

In comparison, traditional metallic strain gauges frequently used in materials testing have GFs that typically range from 2.1 to 2.3, as highlighted in Avilés et al.'s work. In contrast, carbon nanostructures inherently exhibit higher sensitivity, as explored in more detail in this study.

Strain is a fundamental parameter that can profoundly influence the behavior of structures. In the elastic regime, strain and stress are linked through the modulus of elasticity. Thus, strain sensing enables stress sensing when deformation occurs within this elastic range, where strain is reversible. However, elastic strain can introduce complex geometric effects, such as changes in the contact interactions among the fillers within the composite, as previously studied. This microstructural change in the contact interactions between fillers is irreversible and serves as an early indicator before real damage occurs in the material, although it may not necessarily result in the immediate degradation of mechanical properties.

In the pursuit of establishing effective strain sensing structures, the subsequent phase involves a meticulous examination of the complex relationship between stress, strain, and alterations in electrical resistance. This study is fundamental to take advantage of the piezoresistive effect and its potential for creating robust strain-sensing mechanisms.

2.7.1 Advancements in piezoresistive sensing within nanocomposites

The field of piezoresistive sensing has seen an increase in academic interest, driven by their attractive attributes for structural health monitoring applications. The researchers have been working on nanocomposite materials with inherent electrical conductivity subjected to mechanical load. This concerted effort aims to unravel the intricate relationship between mechanical stress and the resulting electrical response.

The nature of mechanical stress, such as tension or compression, can lead to unique electrical responses that are crucial for accurate and reliable deformation detection. A key factor that significantly influences the behavior of these strain sensing structures is the loading percentage of conductive fillers. The concentration of fillers in the matrix has a significant impact on the linear and nonlinear sensing responses. Moreover, this filler loading shapes the GF, an essential parameter that characterizes the sensitivity to mechanical changes.

For the study of piezoresistivity within nanocomposite materials, most researchers opt for a direct current (DC) resistance measurement approach, employing a two-probe method to gauge alterations in electrical resistance. A number of studies, such as Wang et al. (2018), Spinelli et al. (2018), Lim et al. (2011), and Bregar et al. (2020), have effectively utilized the two-probe methodology. This method involves the attachment of two electrodes connected to a digital multimeter, enabling precise recording of electrical resistance changes over time. In particular, Wang et al. (2018) emphasizes that the two-probe method has superior viability in terms of practical implementation compared to a four-probe method (Wang and Chung (2006)). Conversely, the accuracy of the four-probe method is underlined. It utilizes four separate probes - two for applying a known current and two for measuring voltage. This approach eliminates contact resistance issues by physically isolating the voltage-measuring and current-carrying probes. These measurements allow for more accurate and reliable results, especially for low-resistance materials. Ultimately, the choice between the two methods depends on the specific needs of the experiment or application. If precision is paramount, the four-probe method is the method of choice. On the other hand, for practical purposes and ease of use, the two-probe methodology may be appropriate.

In the research conducted by Spinelli et al. (2018), the epoxy resin reinforced with 0.3 wt.% of CNTs configuration has two copper wires affixed to the sample via silver paint. The electrical resistance measured for the specimens was in the order of several kΩ. As stated by the author, these values indicate that contact resistance is negligible in electrical resistance measurements. Therefore, it has no significant impact on electrical resistance measurements under stress.

In contrast, Lim et al. (2011) studied SLJs, where the placement of electrodes warranted a distinct approach. In this specific scenario, the electrodes were placed on the conductive section of the composite, and the metal adherends. To ensure accurate measurement, electrical wires were fixed in position using copper tape at a distance of 1.27 cm away from the substrate bond.

In a separate study by Bregar et al. (2020), which focused on SLJs with aluminum adherends, the measurement strategy differed from the previous examples. The electrical resistance was determined by assessing the joint between the adherends themselves. This approach was possible due to the negligible strain experienced by the adherends, compared to the adhesive bond and respective effect in electrical resistance measurement. This discrepancy was crucial since the change in resistivity generated by deformation changes in the adhesive was markedly different from the minimal changes induced by deformation in the aluminum components.

Georgousis et al. (2015) explored an alternative measurement approach, incorporating four gold stripe electrodes placed perpendicular to the loading direction within the samples of polyvinylidenefluoride (PVDF) matrix reinforced with CNTs. These gold stripes, each measuring 4 mm in length, had a width of 2 mm and a thickness of 60 nm. Notably, the separation distance between successive stripes was 7 mm. The experimental aim of this configuration was to analyze the changes in electrical resistance in three different regions during the tensile tests. This innovative approach was specifically designed to serve the purpose of the study, allowing a more comprehensive assessment of the changes in electrical resistance in different areas of the specimens subjected to tensile loads.

The study conducted by Wang and Chung in 2006 involved measuring the electrical resistance in DC for carbon fiber polymer-matrix composites subjected to flexural (three-point bending) and tensile tests. The results of this study showed promise for the self-detection of flexural strain and damage. The bending test results in a non-uniform distribution of stress/strain, and electrical measurements are more challenging to predict and understand than the uniaxial tension test. In bending testing, one material surface is subjected to compression while the other surface experiences tension. Consequently, it is essential to measure either the volume resistance or the surface resistance for bending tests on both surfaces. In contrast, uniaxial tension tests typically only require measuring the volume resistance. In bending tests, distinct deformations and damages occur on opposing surfaces due to compression and tension forces. To independently assess these effects, surface resistance measurements can be conducted on both the compression and tension sides. The bending mechanism is visually represented and elucidated in Figure 2.10.

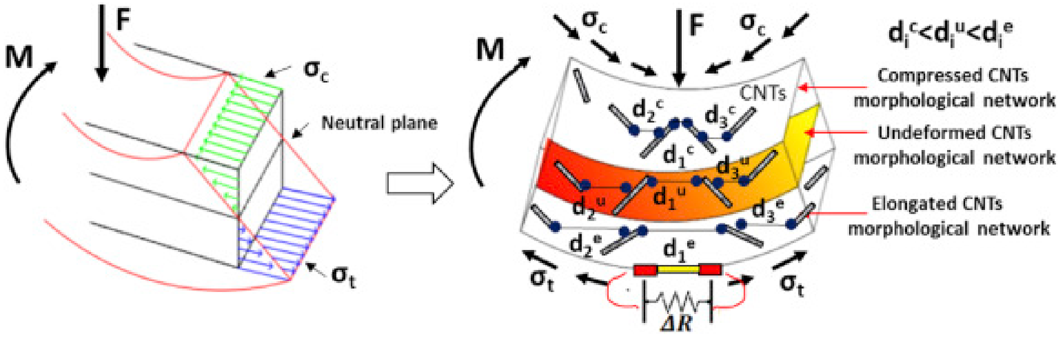

Figure 2.10: Dynamic deformation in the case of bending stress (left) and the geometrical effect on the CNT electrical network (right), adapted from Vertuccio et al. (2016). In the figure: M - bending moment; σ_c - compression stress; σ_t - tensile stress; d_i - relative distance between consecutive CNTs; and F - flexural force.

Figure 2.10 illustrates the particle behavior within the matrix. For the surface subjected to compression, the distance between consecutive nanotubes decreases, resulting in a more conductive nanocomposite. Thus, the electrical resistance decreases. For the surface subjected to tensile stress, the particle distance increases, conductivity decreases, and the electrical resistance increases.

For the elastic regime, changes in surface resistance due to strain are negative for compression and oblique resistance measurements and increase with tension, as demonstrated in Wang and Chung's work. The oblique resistance is the volume resistance in a direction at an angle ($<90°$) to the surface, measured by using two electrical contacts on each of the compression and tension surfaces, such that the contacts on the two surfaces are not directly opposite one another. The results indicated that a strain increase led to a corresponding increase in surface resistance for a tension load condition. Compression exhibited a reversible behavior, resulting in a reduction of surface resistance (negative piezoresistivity). In the case of oblique resistance, bending strain demonstrated a reversible response. Since surface tension/compression resistance is more sensitive to small deflections and depends directly on deflection, it is a better indicator of deformation than oblique resistance. For oblique resistance measurements, the recorded value is the sum of resistance changes attributed to particles approaching the compression side and moving away on the tension side. Although the final result resembles that of the compression side, it is not as pronounced.

An investigation in sensing structures for structural health monitoring in aeronautical components, utilizing epoxy composites loaded with 0.3 wt.% carbon nanotubes, was carried out by Vertuccio et al. (2016). The outcomes of this study align with the previously mentioned observations. The increase in the electrical resistance of the sample is a consequence of an increase in tensile stress. The author justifies these findings by attributing them to the conductive percolation network rearrangement formed by MWCNTs induced by material deformation caused by applied stresses. These results are consistent with the theory that the tunneling effect is the primary electrical conduction mechanism, requiring filler particles to be near to allow for electron flow under tensile stress.

The tensile stress results showed a distinct zone of elastic deformation for lower stress values ($\varepsilon = 2$ %), followed by a plastic zone for higher loads and strain values. The linear mechanical behavior observed in the elastic region corresponds to linear behavior in normalized electrical resistance measurements. In contrast, the plastic region reveals nonlinear behavior, characterized by abrupt changes coinciding with the nano-cracking occurrence within the nanocomposite material.

In contrast to the piezoresistive behavior observed during tensile tests, the normalized change in electrical resistance $(\Delta R/R_0)$ plotted as a function of strain exhibits a nonlinear relationship across the entire strain range (Bregar et al. (2020)), being the electrodes two bolts fixed in each aluminum adherend. Rather than following a linear trend, this behavior follows an exponential law, as documented by Vertuccio et al. (2016). The electrical response of the material explains this behavior, as it is influenced by the tunneling effect between the carbon nanotubes. This nonlinearity is attributed to the reduction in conductive CNT paths and tunneling as the fillers start to separate under shear and tensile strain. This tunneling resistance is particularly sensitive to distance fluctuations, leading to the exponential dependence of $\Delta R/R_0$ on the deformation. This phenomenon arises for flexural mode because specimen curvature predominantly induces elongation rather than compression.

The previous phenomenon explains the simultaneous behavior observed in the mechanical and piezoresistive tests. In the study conducted by Vertuccio et al., it was evident that the changes in electrical resistance varied with the intensity of strain, and the maximum value achieved for each level of deformation remained consistent across consecutive cycles (similar to the results of Figure 2.11b). On the other hand, the elastic and plastic regimes identification relies on correlating the mechanical strain with the temporal change in electrical resistance. The transition from linearity, indicative of the elastic regime, was measured at 2.06 % strain and was characterized by a change in the normalized electrical resistance at approximately 1 %. The sensitivity was measured at 0.43.

A similar conclusion was also drawn by Spinelli et al. (2020). The strain value of 0.5 % marked the boundary between the elastic and plastic regimes in tensile stress. Consequently, the mechanical and piezoresistive plots remained linear up to 0.5 % strain, becoming nonlinear beyond this point. The GF found was 4.0 for a CNT concentration of 0.5 wt.%. Figure 2.11a resumes the previous results.

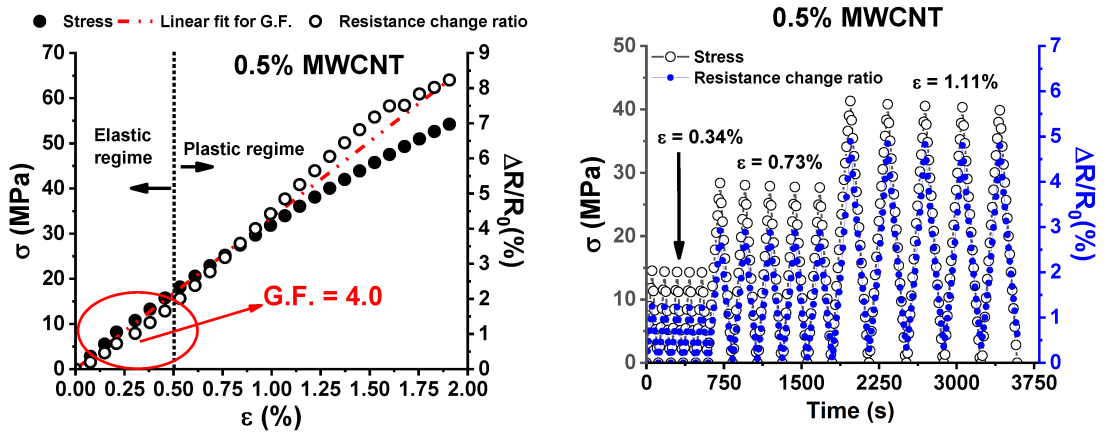

(a) (b)

Figure 2.11: (a) Mechanical response and electrical resistance change ratio observed in tensile stress as a function of the axial strain. (b) Mechanical response and corresponding resistance change ratio versus time under a progressively increasing maximum strain, adapted from Spinelli et al.'s work.

The slope of the $\Delta R/R_0$ curve's interpolating line from experimental data points inside the elastic zone corresponds to the GF. In Figure 2.11b, a synchronic measurement for electrical resistance is observed for a specimen subjected to cyclic tensile loading-unloading. The results, summarized in Figure 2.11, indicated that for linear deformation (0.34 %) in unloaded conditions, the electrical resistance value was null. In contrast, the normalized electrical resistance was obtained above zero, resulting in residual resistance for the plastic regime. This value increased with cycles and deformation, corresponding to effective damage in the structure. These results are promising for SHM applications.

In a related study by Spinelli et al., similar mechanical tests were conducted on epoxy resin reinforced with 0.3 wt.% CNTs for SHM applications. Tensile tests identified the breaking point at a stress of 3.5 %, with the elastic limit set at 2 %. The GF value obtained was 0.43.

For the flexural tests involving three-point bending, the relationship between the normalized change in electrical resistance ($\Delta R/R_0$) and flexural strain exhibited an exponential trend, implying a noticeable difference in the piezoresistive response depending on the type of applied strain, whether tensile or flexural.

The explanation provided by Spinelli et al. (2018) aligns with the earlier discussion. In the case of tensile stress, the material undergoes uniform stretching across the entire cross-section of the applied load, causing the percolating network to shift uniformly with the force. Consequently, the electrical response is linear. In contrast, when subjected to flexural stress, the material experiences a combination of compressive and tensile stresses due to specimen curvature. For both tests, the electrodes were around the sample, measuring the volumetric electrical resistance variation. The material's electrical response is more significantly impacted by these outcomes, mostly because of variations in the spacing between the conductive particles. Consequently, this leads to the exponential relationship observed in $\Delta R/R_0$ vs. strain.

To clarify the variations associated with tensile and flexural strain and the linear and nonlinear behaviors, Yao et al. (2017) introduced a bilinear relationship between the fractional change in electrical resistance and the tensile (or flexural) strain. For the three-point bending tests, the variation in GF values meant that the deformed specimens entered the buckling phase, while the abrupt increase in GF values during the uniaxial tensile tests indicated that the samples were stretched beyond the elastic range and began to yield. This behavior is shown in the piezoresistive curves resulting from continuous carbon fibers embedded within thermoplastic parts manufactured by fused deposition modeling printed structures.

To quantitatively measure strain within the elastic range (before the proportional limit point A) and detect damage within the yield stage (between the proportional limit point A and yield point B), the sensitivity of carbon particles relative to GF values can be utilized as a self-sensing mechanism. This relationship is illustrated in Figure 2.12, which displays linear fits of the fractional change in resistance segmented into two parts: one for tensile strain or flexural strain in the elastic regime and the other for plastic deformation. The obtained GFs for both load cases were as follows: 0.69 and 6.65 for the elastic and plastic regimes during tensile loading and 0.22 and 0.092 for the elastic and plastic regimes during flexural loading.

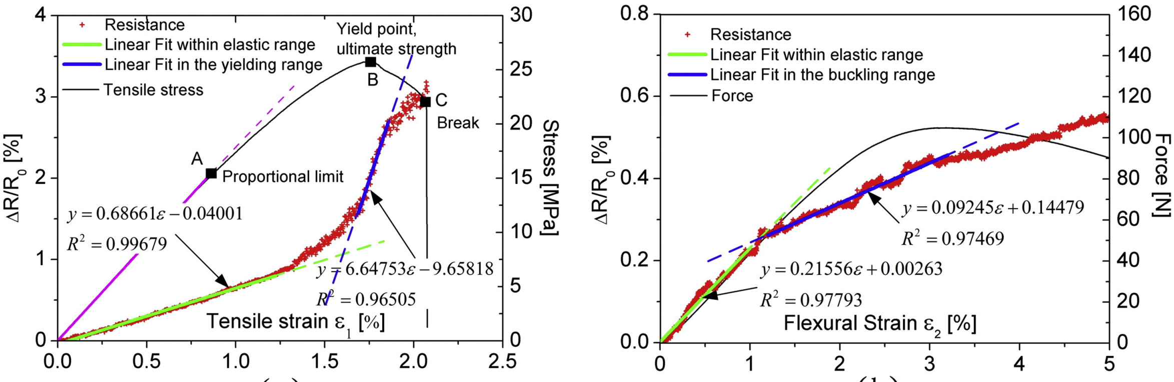

(a) (b)

Figure 2.12: Linear fit analysis of fractional change in resistance in two segments: (a) in relation to tensile strain, and (b) in relation to flexural strain, according to Yao et al. (2017).

In their study, Hu et al. (2008) explored a strain sensor based on a epoxy reinforced with MWCNTs and investigated the impact of tunneling on sensing behavior. They have developed an improved three-dimensional statistical resistance network model that incorporates the behavior of the tunneling effect between neighboring carbon nanotubes with a fiber reorientation model. Extensive numerical simulations and experimental measurements were conducted to understand the piezoresistivity in polymer/CNT nanocomposites for potential strain sensing applications. Their findings revealed that under small strain values, the resistance change was influenced primarily by the tunneling effect between neighboring CNTs, rather than the disruption of the conductive network. The piezoresistivity in these nanocomposites exhibited nonlinearity at low CNT loading, a phenomenon qualitatively explained by the tunneling effect. However, at higher CNT loading levels, the piezoresistivity approximated linearity.

The previous findings align with those of Sanli et al. (2016) and Sanli et al. (2017), who observed in their study that at low MWCNT concentrations (0.3 wt.%), a nonlinear piezoresistivity was apparent due to the predominant influence of tunneling, presenting a coefficient of determination (R^2) of 0.868. Conversely, materials with higher CNT concentrations exhibited improved linearity, as seen in the cases of 0.5 wt.% with an R^2 of 0.996 and 1 wt.% with an R^2 of 0.999. However, according to Georgousis et al. (2015), at a filler content of 1.25 wt.% - slightly above the percolation threshold - the sensitivity and resistance values significantly increased. Within this concentration range, the deformation of the nanocomposite induced a more pronounced alteration in the conductive network, leading to a notable change in resistance. It is important to note that in this case, linearity was sacrificed by some noise introduction in the measurements. Nevertheless, the overall trend in the curve remained observable.

To investigate the sensing application and response, Sanli et al. (2017) conducted a study using a reinforcement of 0.5 wt.% MWCNTs dispersed in an epoxy resin directly deposited on a glass-reinforced epoxy cantilever beam. This setup was designed to function as an equivalent to commercial metallic strain gauges. The primary goal was to compare the responses to loading between the two sensor options. Compared to metallic strain gauges, the MWCNTs/epoxy nanocomposite exhibited a faster response and recovery under both tensile and compressive loading conditions. This swift response was attributed to the quicker reorganization of the CNT network within the polymer matrix during tensile loading.

In contrast to the previously discussed studies where tensile loading typically resulted in a positive variation of electrical resistance and compression led to negative piezoresistivity, there can be situations where this relationship is reversed. As explained above, the electrical resistance of nanocomposites depends strongly on the CNT's interaction through the tunneling effect rather than being determined solely by the inherent resistance of the CNTs themselves. When CNTs reinforce epoxy resin matrices, they form a nanocomposite affected by the Poisson's ratio. To clarify this question, Hu et al. (2008) introduced the concept of considering the rigid-body movement, which encompasses the change in position and orientation of the CNTs under the influence of strain and Poisson's ratio. This movement can be effectively assessed using a 3D fiber reorientation model. This model helps to predict the potential intersections between CNTs and tunneling resistances between them within a specific cutoff distance. In their study, the researchers modeled these rigid-body movements to gain valuable insights into the electrical behavior of these nanocomposites.

In the case of tension applied along the main direction of the sensor, the transverse direction experiences compression. Consequently, the sensor undergoes mechanical loading in the longitudinal and transverse directions. The transverse loading is a direct result of the sample compression, while the longitudinal loading is transmitted through the tension applied to the sample, facilitated by the shear deformation of the resin matrix. This phenomenon is illustrated schematically in Figure 2.13. Considering the rigid-body movement of the CNTs, the alteration in position and orientation of the CNTs due to strain and Poisson's ratio can be contemplated in a 3D model, assuming the nanocomposite to be incompressible.

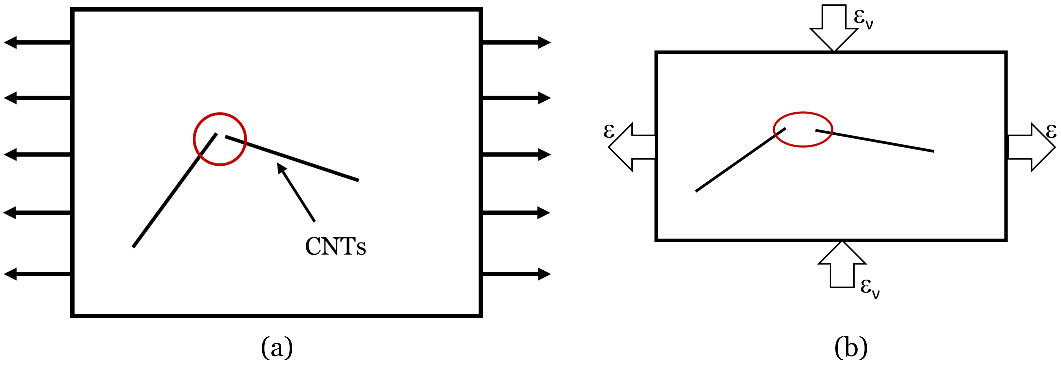

Figure 2.13: Rigid-body movements of CNTs in polymer induced by strain and Poisson's ratio. (a) Initial state before tensile strain application. (b) Deformation resulting from tensile loading along the longitudinal direction (ε) and transverse direction (ε_ν). Based on the work of Hu et al..

This configuration makes it likely that transverse compression will have a more significant impact on changing the material electrical resistance than the predicted low efficiency of load transfer in the longitudinal direction. As a result of this compression, the sensing structure exhibits a negative piezoresistivity, which coincides with a decrease in the tunneling resistance within the particle network.

To delve deeper into the impact of this mechanical phenomenon on the electrical network of CNTs within the epoxy matrix, Luo et al. (2014) conducted an extensive study by embedding SWCNTs-FibSen sensors in fiberglass prepreg laminates. The aim was to map the stress/strain states of the host composite under various deformation modes - tension, bending, compression, and failure, in different directions. Figure 2.14 summarizes the outcomes of Luo et al.'s work, illustrating the experimental setup and the piezoresistive response plotted over time for a cyclic loading-unloading state. Two sensors were positioned, one above and the other below the neutral surface, to monitor distinct piezoresistive responses under flexural stress.

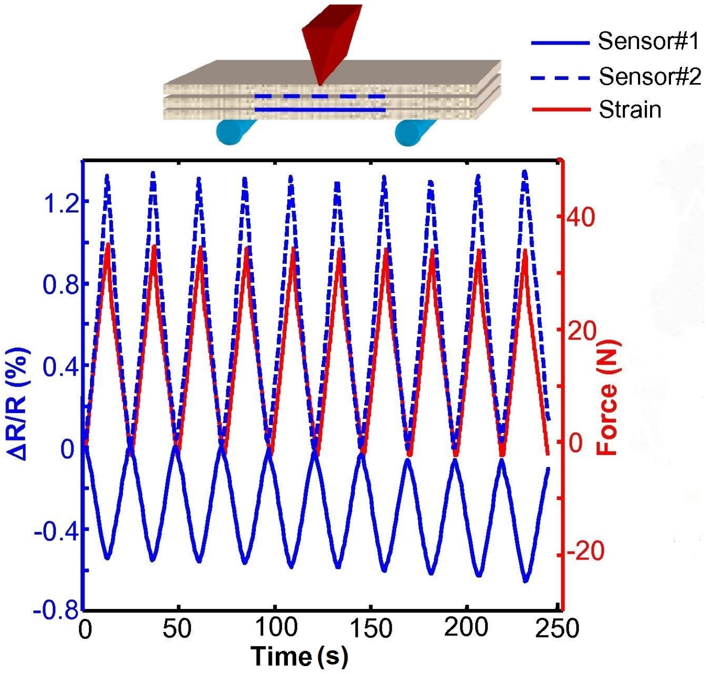

Figure 2.14: Piezoresistive response of glass SWCNT-FibSen sensor embedded in epoxy/glass fiber laminate under cyclic three-point bending test, from Luo et al. (2014).

In this arrangement, the sensor located above the neutral surface, experiencing tension in the transverse direction and compression in the longitudinal direction, demonstrates higher resistance. Conversely, the sensor beneath the neutral surface, subjected to compression in the transverse direction and tension in the longitudinal direction, exhibits lower resistance. The unexpected piezoresistive behavior observed in the structural sensor can be attributed to the Poisson's effect. This phenomenon indicates that the overall electrical response is influenced by the competition between the breakdown and reconstruction of the percolated network under different loading conditions, either on the surface or within the volume of the sample.

This theory finds further support in the following analysis. The study conducted by Doshi et al. (2020) delves deeper into this phenomenon, specifically investigating how transverse strain impacts the sensitivity of piezoresistive sensors. Their findings highlight the significant influence of the properties of the substrate on these sensors. They also emphasize that Poisson's ratio must be taken into account when calibrating sensors, especially for practical applications in the field.

2.7.2 Piezoresistive sensing approaches in structural adhesives for SHM

In the preceding section, this work delved into several scientific papers that concentrated on strain sensing for Structural Health Monitoring (SHM) applications in general structures, focusing on bulk samples of epoxy reinforced with CNTs and, in some instances, composite laminates.

The insights obtained from these studies apply to diverse structures incorporating nanocomposites. Adhesive joints stand out as a noteworthy application, and the strain sensing for health monitoring presents substantial benefits. Evaluating the structural reliability of adhesive joints can be challenging, often necessitating various non-destructive inspection methods to ensure a secure bond between components.

In the literature, numerous studies have investigated the structural reliability of adhesive joints by employing nanocomposites with piezoresistive properties for structural motorization. These studies vary in their objectives, with some focusing on strain sensing while others specifically aim to detect failure modes in adhesive systems. For instance, in a study led by Lim et al. (2011), the objective was to identify various types of damage in adhesively bonded hybrid composite-to-metal joints by taking advantage of the piezoresistive properties of the adhesive through resistance measurement. The researchers utilized a nanocomposite consisting of a 1.0 wt.% mixture of MWCNTs and epoxy resin as an adhesive, with a bond line thickness of $0.762\ \mathrm{mm}$. End-tabs were incorporated into the adherends' structure in the SLJ specimens to facilitate tensile tests. These tabs served a dual purpose: aligning the specimens in the loading fixture and providing electrical isolation.

Different surface treatments were applied to induce distinct failure mechanisms in the composite/steel hybrid joint systems. The study identified three distinct failure mechanisms: adhesive failure, composite failure, and mixed failure involving both the composite and adhesive. Interestingly, each of these failure mechanisms exhibited distinctive resistance signals. The previous observation suggests that resistance measurements alone can identify the specific failure mechanism. The sensitivity of resistance changes to damage varied among specimens experiencing adhesive failure at the steel interface. In contrast, this sensitivity was much more limited in specimens that experienced mixed adhesive/composite or pure composite failure. This difference in sensitivity was attributed to the variations in the regions formed during the adhesive debonding from the steel surface in each type of specimen.

Overall, this work by Lim et al. (2011) provided valuable insights into the failure behavior of these joints under both static and dynamic loading conditions. It also highlighted the importance of understanding how different failure mechanisms (such as steel debonding, combined debonding with composite failure, and pure composite failure) result in distinct resistance behaviors. Furthermore, the study demonstrated that deliberately manipulating the surface conductivity of a composite substrate can serve as an effective means of detecting damage within bonded joints. This approach holds promise for cost-effective composite design.

Moving on to Bregar et al. (2020), their work focused on developing a strain sensing technique using epoxy/CNT-modified adhesives between aluminum adherends. The objective was to investigate the strain-sensing capabilities of epoxy/CNT adhesive in detecting damage propagation within the adhesive layer. The study aimed to establish a correlation between deformation and normalized electrical resistance measurements to identify critical points in joint performance for thick and thin bond thicknesses. This research contributes to the field by exploring the potential of strain sensing for adhesive joint health monitoring, providing insights into the relationship between deformation and electrical resistance changes.

In the experiments of Bregar et al. (2020), the specimens were subjected to static tensile loads while simultaneously measuring their electrical resistance. Initially, was observed a negative piezoresistive response for a deformation of $0.048\,\mathrm{mm}$ and a load of $1.6\,\mathrm{kN}$. However, beyond this point, the piezoresistive response became positive, following an increasing load trend. The predominance of compressive forces in the transverse direction during the initial loading phase explains the observed behavior. As the load increased, tensile forces became dominant, causing an increase in the distance between consecutive CNT particles. Bregar et al. also mentioned that the compressive forces that develop within the thickness of the adhesive, perpendicular to the tensile load axis of the testing machine, can affect tunneling. The adhesive joint eventually failed in adhesion mode when the extension reached $0.1\ \mathrm{mm}$. As described previously, the results of the electromechanical testing until failure for SLJs are presented in Figure 2.15.

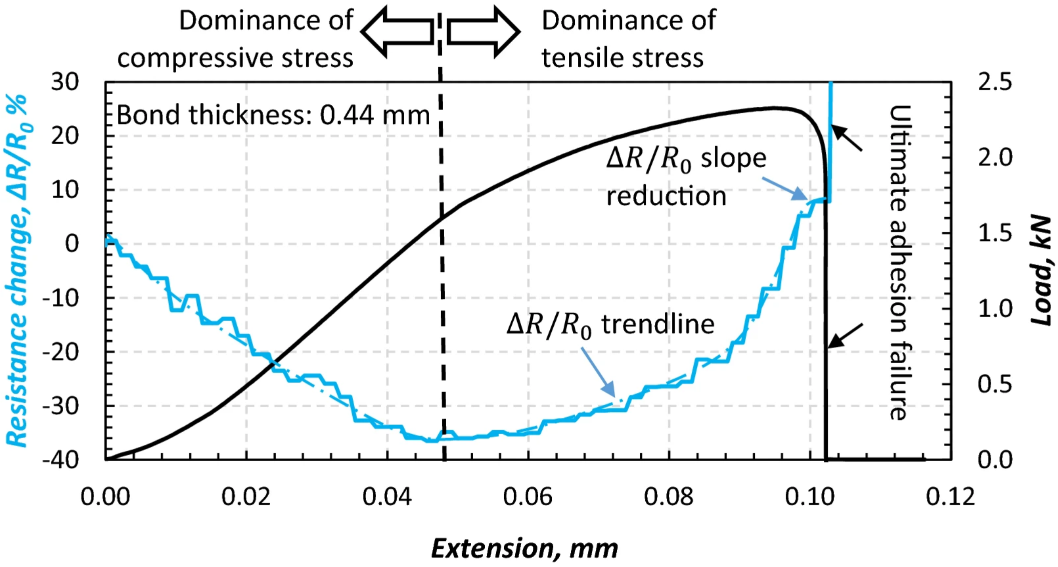

Figure 2.15: Evolution of $\Delta R/R0$ in SLJs with CNT modified adhesive during a quasi-static tension. From Bregar et al.'s work.

In cyclic testing, thinner adhesive bonds ($0.18\ \mathrm{mm}$ thickness) showed 100 times more sensitivity to varying cycle loads than thicker bonds ($0.43\ \mathrm{mm}$ thickness) while having a higher number of CNT contact points. This result implies that the sensitivity of the adhesive is highly influenced by bond line thickness. Additionally, in Figure 2.16, the initiation and propagation of damage within the adhesive joint during cyclic loading are visible before the ultimate bond failure, as indicated by the electrical resistance measurements. The residual electrical resistance begins to rise, and the linear response starts to deviate (nonlinearity increases).

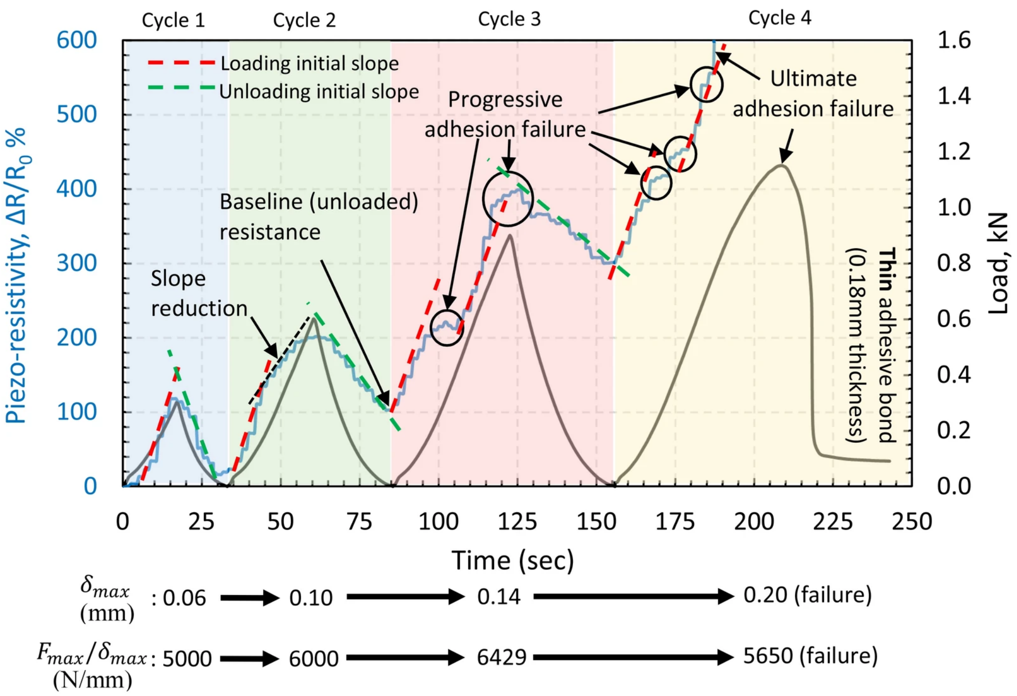

Figure 2.16: Electrical resistivity response during cyclic tensile loading of SLJ specimens with 0.18 mm bond thickness, as presented in the study by Bregar et al..

In the context of cyclic loading, the inconsistent or monotonic piezoresistive variation can be indicative of hysteresis. This phenomenon arises from a response delay in the polymer strain sensing. Duan et al. (2020) justifies this not fully explained behavior by attributing it to the competition between network breakdown and reformation during cyclic loading. The author points out that various studies are responsible for the observed hysteresis behavior, linked to the intrinsic viscoelastic nature of polymers, viscoelastic characteristics of conductive fillers, delayed reaggregation between filler-filler bonds/interactions in a relaxed state, poor interfacial adhesion, and imperfect recovery of conduction paths due to friction between the solid-state sensing element and polymeric molecules. In addition, hysteretic behavior depends on the integrity and robustness of the conductive network morphology, as well as the amplitude of the deformation.

In studies conducted by Daliri et al. (2019) and Daliri et al. (2020), alternating current (AC) has been employed to explore the piezoresistive properties of adhesive joints containing conductive nano-fillers. In the case of Daliri et al. (2019), the emphasis was on structural monitoring using SLJs made of a conductive MWCNT-epoxy adhesive under quasi-static stress conditions with an alternating current stimulus. The objective was to investigate how variations in defect sizes and shapes affect the sensing capabilities of adhesive joints. To this end, different weight percentages of MWCNTs were incorporated into the adhesive layer and then subjected to shear loads, with the impedance monitored. The reinforcement content was 2.5, 6, and 9 % by weight of CNTs.

The epoxy adhesive with 9 % MWCNTs exhibited a steeper slope on the $\Delta R/R_0$ curve during tensile loading compared to those with 2.5 % and 6 %, indicating superior sensing capabilities. The load of 9 wt.% CNT was selected for a detailed examination of damage progression. It was found that the impedance response for crack growth at a defect boundary differed from cases where the crack developed within the adhesive layer.

These findings illustrate the potential of piezoresistive adhesives for structural monitoring applications in adhesive joints. The reviewed literature showcases the ability of these adhesives to detect and characterize stress/strain relations, monitor damage progression, and, with the use of AC, enable the detection of specific defects within the overlap area. Building on the accumulated knowledge of adhesive joints and piezoresistive sensing, the subsequent focus of this work will be on the development of SLJs with sensing capabilities for strain monitoring.

Chapter 3

Materials and Experimental Procedure

As outlined in Chapter 1, the objective is to optimize the CNT filler loading in an epoxy matrix to create an electrically conductive system with piezoresistive sensing. After this optimization, this system will be applied as an adhesive in a SLJ structure and studied as a sensing structure for detecting deformations and structural damage.

3.1 Materials

As previously reviewed, adhesives must be inert systems, requiring compatibility between adherends and adhesives. In accordance with Banea and da Silva (2009a), epoxy adhesives, commonly used for composite matrices, are preferred for bonding composites based on epoxy matrices due to the compatibility between the resin and adhesive.

Thus, the polymeric matrix chosen for this study was an epoxy resin, specifically SR 8100, paired with a hardener SD 8824 provided by Sicomin. This epoxy system possesses a low viscosity, which can aid in the dispersion of CNTs within the epoxy. Additionally, this system exhibits high mechanical properties. Table 3.1 summarizes the mechanical and physical properties of the epoxy/hardener system.

Table 3.1: Main mechanical and physical properties on cast resin, listed in the data sheet Sicomin (2019).

Property	**Units**	**Sicomin SR 8100/SD 8824**
Colour		Light yellow
Viscosity @ (25 °C)	(mPa · s)	285 ± 60
Density @ (20 °C)	(g/cm^3)	-
Modulus of elasticity (tensile)	(N/mm^2)	2900
Maximum strength (tensile)	(N/mm^2)	60
Elongation @ max. load (tensile)	(%)	3.2
Elongation @ break (tensile)	(%)	3.8
Modulus of elasticity (bending)	(N/mm^2)	3000
Maximum strength (bending)	(N/mm^2)	108
Elongation @ max. load (bending)	(%)	4.9
Elongation at break (bending)	(%)	11.8
Charpy impact strength	(kJ/m^2)	52
Glass transition / DCC	(°C)	63
Water absorption 48 h/70 °C	(%)	1.2

The chosen epoxy system was reinforced with carbon nanotubes - NC7000^{TM}. The technical specifications of these nanotubes are provided in Table 3.2.

Table 3.2: Specific characterization of carbon nanotubes - NC7000$^{\text{TM}}$ supplied by NANOCYL®, based on the datasheet NANOCYL® (2016).

Property	**Unit**	**Value**	**Method of measurment**
Average diameter	nm	9.5	Transmission electron microscopy (TEM)
Average length	µm	1.5	Transmission Electron microscopy (TEM)
carbon purity	%	90	Thermogravimetric analysis (TGA)
Transition metal oxide	%	<1	Inductively coupled plasma mass Spectrometry (ICP-MS)
Amorphous carbon	-	*	High resolution transmission electron microscopy (HRTEM)
Surface area	m^2/g	250-300	BET surface area analysis
Volume resistivity	Ωcm	10^{-4}	Internal test method (resistivity on powder)

*Pyrolytically deposited carbon on the surface of the NC7000$^{\text{TM}}$

These are thin multi-walled carbon nanotubes (MWCNTs), produced through the catalytic chemical vapor deposition (CCVD) process and supplied by NANOCYL®. MWCNTs exhibit a low percolation threshold, making them desirable for this investigation due to their high electrical conductivity and ease of processing. Moreover, they have an aspect ratio of 1500, a significant factor for enhanced electrical properties and a lower percolation threshold.

As discussed in Chapter 2, CNTs aggregate into bundles or agglomerates. At the nanoscale, they exhibit a spaghetti-like structure (see Figure 3.1a), while at a macro scale, CNTs resemble black powder (see Figure 3.1b).

As for the adherent, a glass fiber fabric was employed in the manufacturing process. The technical specifications of the glass fabric used in the composite production for adherends are summarized in Table 3.3.

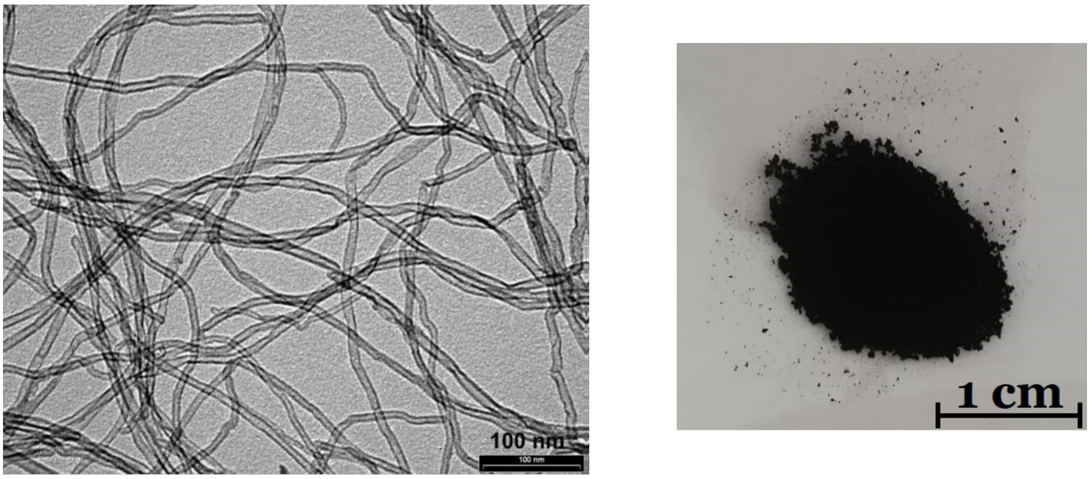

(a) (b)

Figure 3.1: (a) Illustrative nanography of the MWCNTs obtained by TEM, from NANOCYL® (2016). b) Illustrative macrograph of the MWCNT powders used.

Table 3.3: Technical specifications of glass fabric 1195 P supplied by REBELCO, derived from the Datasheet (Rebelco).

		Unit		Tolerance
Weave pattern			Plain	
Total surface mass	195	g/m^2		± 4 %
Yarn				
	warp		EC 13-136	
	weft		EC 13-136	
Fibre count				
	warp	/ cm	8	
	weft	/ cm	6	
Thickness		mm	0.17	± 15 %

3.2 Experimental procedure - manufacturing

The experimental procedure commenced with the manufacturing and optimization of bulk adhesive samples, which served as the initial step to refine adhesive production. These bulk samples were used to consider adhesive options before their application in the configuration of SLJ by studying their electrical and mechanical behavior and piezoresistive response.

3.2.1 Bulk adhesive samples - manufacture of pure epoxy samples

To fabricate the bulk adhesive samples, the work of Santos et al. (2021) influenced this experimental approach. They investigated the impact of manufacturing parameters on the mechanical properties of nano-reinforced carbon fiber reinforced polymer (CFRP) using the same epoxy resin employed in this study. They subsequently applied their findings to produce an epoxy resin with carbon nanofibers (Santos et al. (2023)).

The process began by accurately weighing the epoxy resin and hardener with a $100/22$ mixing weight ratio, as recommended by the manufacturer's datasheet (Sicomin (2019)). An epoxy weight of $50\,\mathrm{g}$ was employed for the necessary dimensions.

Subsequently, the hardener and resin were mixed manually with a stirring rod to ensure homogeneous mixing. Manual mixing, however, often introduces air into the mixture. The mixture was subjected to degassing in a vacuum chamber (Bacoeng Vacuum Chamber) using a vacuum pump (VEVOR 3CFM) (see Figure 3.2a) to eliminate any residual air bubbles and ensure a nearly flawless system. This process lasted approximately 5 minutes and effectively removed air bubbles. The degassed mixture was poured into a cardboard mold with dimensions of $120 \times 80 \times 3\ \mathrm{mm}^3$. The final step in manufacturing the pure epoxy samples involved a curing process recommended by the technical datasheets. In the case of the SR 8100 epoxy with SD 8824 hardener system, this involved curing for 24 hours at room temperature followed by an additional 24 hours at $40\ ^\circ\mathrm{C}$.

Upon completion of the curing process, the samples were extracted from the mold and cut into specimens with dimensions of $80 \times 10 \times 3\ \mathrm{mm}^3$. These dimensions were based on EN ISO 178:2003 standard (ISO (2003)). At this stage, the pure epoxy specimens were ready for testing.

3.2.2 Bulk adhesive samples - manufacture of epoxy-CNT nanocomposites

The fabrication of bulk adhesive samples with CNTs and epoxy resin followed a process similar to that outlined in Santos et al. (2023) for carbon nanofibers.

The procedure commenced similarly to the previous section by weighing the epoxy resin and carbon nanotubes. Notably, the utensils (cups and spoons) employed for measuring epoxy resin and CNTs were thoroughly cleaned with acetone and allowed to dry to prevent any contamination from residual materials.

From the optimized process presented in Santos et al. (2021), the epoxy resin and CNT mixture were combined using a mechanical mixer (digital overhead stirrer LBX OS20 series - vertical rotation stirrer) (see Figure 3.2b) set to a shear rate of 1000 rpm and subjected to a sonication bath using an Ultrasonic Cleaner model AU-65 operating at a frequency of 40 kHz for 3 hours.

(a) (b)

Figure 3.2: (a) Bacoeng vacuum chamber and vacuum pump - VEVOR 3CFM. (b) Digital overhead stirrer LBX OS20 series - vertical rotation stirrer and sonication bath - Ultrasonic Cleaner model AU-65.

Following this process, the hardener was added to the previously mixed mixture by weighing it by the ratio specified on the manufacturer's datasheet. The two components were combined at 300 rpm for 3 minutes. The combination underwent a sonication bath at a constant frequency of 40 kHz during this process. Ice was added into the ultrasonic bath to prevent any temperature rise that would have caused the mixture to surpass the glass transition temperature (T_g) of the resin.

This mixture process incorporated air into the system, so degassing was imperative. The process took approximately 7 minutes to eliminate air from the mixture, as the viscosity of this mixture was higher compared to pure epoxy.

Subsequently, the mixture was carefully deposited into a cardboard mold similar to the one previously used, and the curing process was identical to that described earlier for the epoxy/hardener system.

However, after the curing process and removing the nanocomposite from the cardboard mold, macroscopic observation revealed visible agglomerations of CNTs within the epoxy matrix. Refer to Figure 3.3 for a visual representation of this issue. Microscopic examination allowed precise identification of these agglomerations. Concentrations of CNTs were highlighted by the use of a backlight, which improved the visibility of the dispersed agglomerates in the epoxy resin. Darker regions in the picture correspond to different-sized agglomerates scattered across a lighter background.

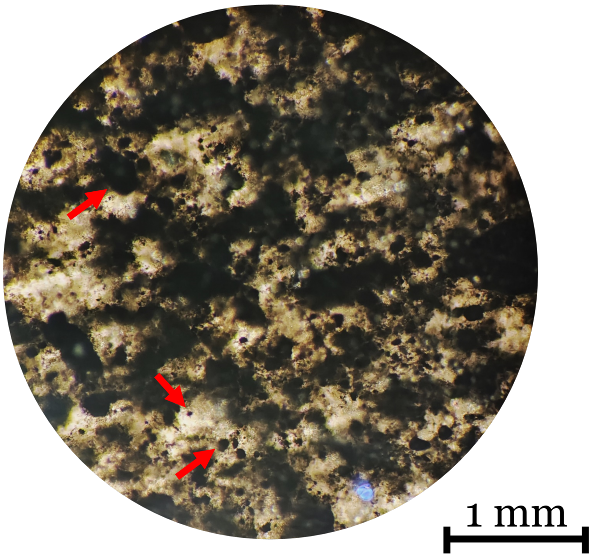

Figure 3.3: Microscopic visualization of epoxy reinforced with 0.25 wt.% of CNTs samples, with clear agglomerations dispersed in the epoxy matrix. Various cluster sizes, highlighted by red arrows, exhibit a circular shape.

Given this outcome, it was imperative to adapt the manufacturing method of CNT/epoxy bulk adhesives to mitigate these agglomerations. Existing literature suggests the utilization of a sonication probe during the mixing process. Notably, Vertuccio et al. employed a sonication probe for 20 minutes to achieve a uniform mixture of epoxy and MWCNTs, while Moriche et al. (2018) adopted a two-step dispersion method that incorporated both sonication probe and calendering processes.

These studies served as the basis for adjusting the experimental protocol. First, the appropriate ratio of epoxy and CNT weights had to be measured. After that, a mechanical mixer at a rotation speed of 1000 rpm for an hour was used to combine this system. To avoid CNT agglomerates from forming, the mixture was simultaneously placed in a sonication bath running at a frequency of 40 kHz. After this procedure, a sonication probe (Q125 Sonicator®) operating at 20 kHz applied two pulses to the mixture, each lasting 30 seconds. The process was repeated, including 1-hour mechanical mixing, sonication bath treatment, and two pulses of 30 seconds in the sonication probe.

After the initial mixing of epoxy resin and filler, the hardener was added and mixed for 3 minutes using a mechanical mixer. The mixture underwent a degassing process for approximately 15 minutes due to increased viscosity from sonication. Following this procedure, the prepared mixture was poured into a cardboard mold, initiating the curing process as outlined.

In contrast, this revised manufacturing process produced a nanocomposite with defects. While the surface of the nanocomposite appeared defect-free upon demolding and macroscopic inspection, a closer examination after cutting the nanocomposite plate into smaller sections revealed an interior with voids and areas that had not undergone proper curing.

These defects are represented in Figure 3.4, which showcases two distinct types of defects - voids and regions with incomplete curing. This outcome indicated a significant challenge in achieving uniform curing and degassing of the nanocomposite material, which can be attributed to the complexities introduced by the fillers' addition throughout the manufacturing process.

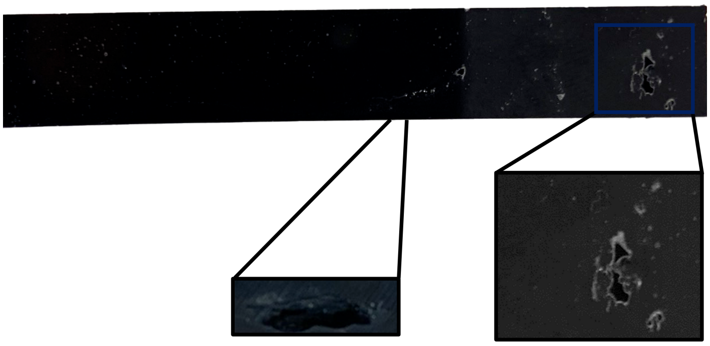

Figure 3.4: Macroscopic observation of nanocomposite defects. Two types of defects are visible - voids (on the surface) and areas with incomplete curing (through-thickness).

To meet the ongoing challenges of the manufacturing process, a new optimization phase was explored, focusing on improving the degassing process. Some studies inspired degassing for extended periods, as suggested by Spinelli et al.'s work. However, prolonged exposure to elevated temperatures during degassing, especially in the presence of the hardener, was observed to increase viscosity and the risk of premature curing of the nanocomposite. This result led to a hypothesis formulation and a new approach to the degassing process.

In this new approach, after the second cycle of mixing and the two pulses of the sonication probe as previously outlined, the mixture was subjected to degassing. At this stage, the mixture's viscosity was still manageable, making it conducive to releasing air bubbles. This initial degassing step lasted for 20 minutes. Following this, the hardener was added and mixed for 3 minutes at a speed of 300 rpm. Afterward, the mixture was subjected to another round of degassing that lasted 15 minutes.

Subsequently, the mixture was deposited into an open cardboard mold and subjected to a final degassing stage. This degassing cycle lasted 35 minutes in a vacuum chamber. It is important to note that as each minute passed, the mixture's viscosity increased progressively. Thus, a close monitoring was necessary to guarantee the manufacture of the nanocomposite.

The mixture was consistently kept in an ice bath during the time in the vacuum chamber and throughout the sonication bath and probe processes to mitigate any potential temperature-related problems. This careful temperature control aimed to prevent unwanted curing reactions and to ensure the mixture's stability throughout the various processing stages.

After the successful curing phases and the voids and uncured parts elimination, the nanocomposite board (see Figure 3.5) was divided into specimens with the exact dimensions as the pure epoxy samples. Subsequently, these nanocomposite specimens were subjected to electrical resistance measurement tests. To facilitate this process, electrodes were inserted into the samples to measure variations in electrical resistance. These electrodes were painted using a solution of silver conductive paint (RS 186-3600). The paint was applied manually to the samples with a brush, using paper tape molds fixed on the specimen surface. This method ensured the precise placement of the conductive material. The resulting electrodes were designed to be 4 mm wide and 10 mm long, with a spacing of 4 mm between them. To further enhance the accuracy of electrical resistance measurements, copper wires were attached to the electrodes using additional silver conductive paint.

The applied paint and the final arrangement of electrodes on the completed sample are visually represented in Figure 3.6. This meticulous process guaranteed the successful integration of electrodes onto the nanocomposite specimens, enabling accurate electrical resistance measurements and facilitating the evaluation of the nanocomposite's conductivity characteristics.

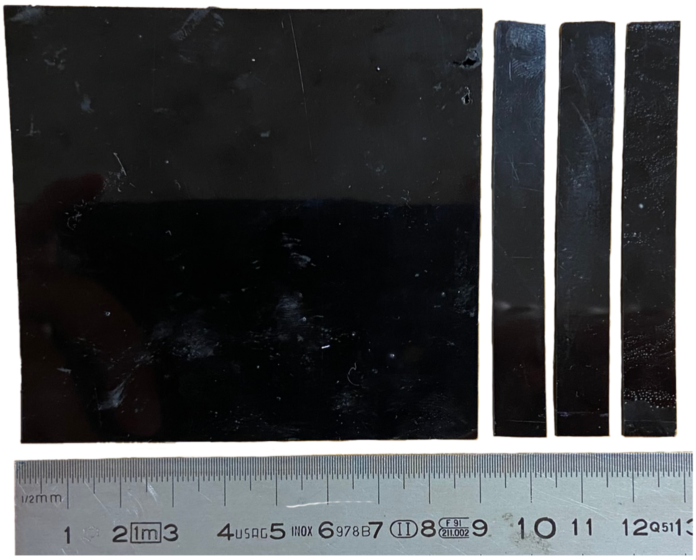

Figure 3.5: Nanocomposite board and cut samples after the curing process and demolding for 0.5 wt.% CNT loading.

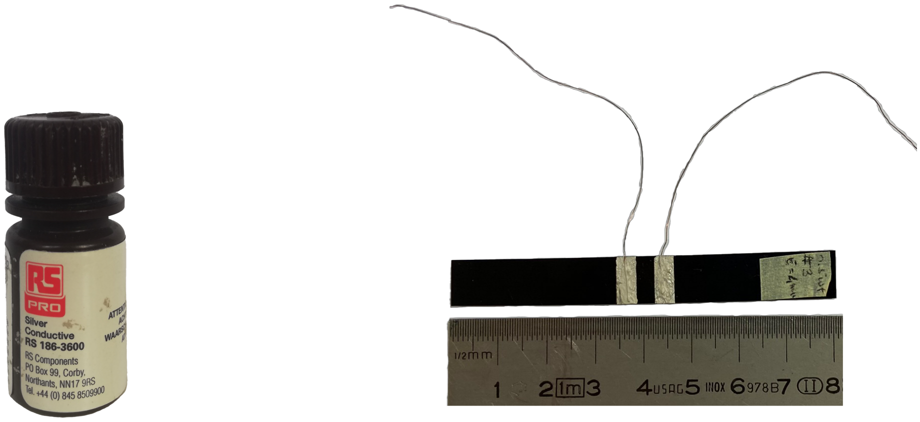

(a) (b)

Figure 3.6: (a) Silver paint used for electrode manufacturing with a volume resistivity of $0.001\ \Omega\,\mathrm{cm}$ (based on the manufacturers' datasheet (RS Pro)). (b) Final sample with the electrodes and copper wires. Sample with 0.5 wt.% of CNTs.

After completing this manufacturing process, the samples were prepared for testing. It is significant to remember that all specimens had their thickness, length, and width measured. For each sample dimension, five measurements were taken. Then, the average value was calculated and used as the reference measurement value. This rigorous approach ensures accurate and reliable data for further analysis and assessment of the samples' properties.

By systematically addressing the challenges encountered in the initial manufacturing processes, this new approach optimized the dispersion and curing of the nanocomposite to obtain bulk samples for further testing.

3.2.3 SLJ samples - manufacture of glass fiber composite adherends

In the SLJ manufacturing process, the used adherends were composite of glass fiber. The adhesives were created using glass fiber supplied by Rebelco, and the epoxy matrix was the same as that used to manufacture bulk adhesives (SR 8100/SD 8824 epoxy system).

Given the goal of studying the electrical response of these structures, it was essential to have a balance between flexibility and reliability. In line with the findings presented in Chapter 2, thinner adherends were chosen, following the approach of Ozel et al. (2014) and Song et al. (2010), who utilized thicknesses of $1.6\ \mathrm{mm}$ and $1.52\ \mathrm{mm}$, respectively. Adherends composed of 12 layers of glass fiber fabric were decided upon.

The manufacturing process for these glass fiber composites involves several steps to ensure the creation of a defect-free structure, as outlined below:

1. Cut glass fiber fabric into dimensions of $330 \times 330\ \mathrm{mm}^2$;
2. Prepare $250\,\mathrm{g}$ of epoxy resin mixed with hardener following the steps detailed in section 3.2.1 for pure epoxy samples;
3. Lay out a Teflon sheet and apply $1/13$ of the epoxy resin on it;
4. Place a layer of glass fiber fabric onto the resin and spread it using a spatula;
5. Repeat the previous two steps for successive layers until reaching 12;
6. The final layer should have the remaining $1/13$ of epoxy resin applied on top;
7. Use an absorbent material to collect excess resin and secure it with paper tape;
8. Cover the composite with another Teflon sheet;
9. Place the composite in a bagging film, insert the vacuum valve, and seal the bag;
10. Put the bagged composite in a hydraulic press at a pressure of $25\ \mathrm{bar}$;
11. Activate the vacuum pump for about 30 minutes. Once the vacuum process is complete, turn off the vacuum and allow the laminate to remain in the press for 24 hours. Following this, transfer the laminate to an oven set at $40\,^{\circ}\mathrm{C}$ for an additional 24 hours, employing the same curing procedure as for the bulk samples.

These steps ensured the creation of adherends with the desired properties and dimensions for subsequent testing.

Figure 3.7a depicts the final product of the glass fiber composite adherends after the curing process. This composite board was marked and cut into two different types of specimens to facilitate SLJ manufacturing (see Figure 3.7a). The cutting process resulted in rectangular pieces measuring $100 \times 25\ \mathrm{mm}^2$, intended for use as the adherends, and square pieces measuring $25 \times 25\ \mathrm{mm}^2$, which served as end-tabs (see Figure 3.7b).

The dimensions of these specimens were determined according to the ASTM D 3165 standard (a), which outlines procedures for evaluating the strength properties of adhesives in shear by tension loading of SLJ laminated assemblies. The average thickness of the adherends was $1.9\ \mathrm{mm}$.

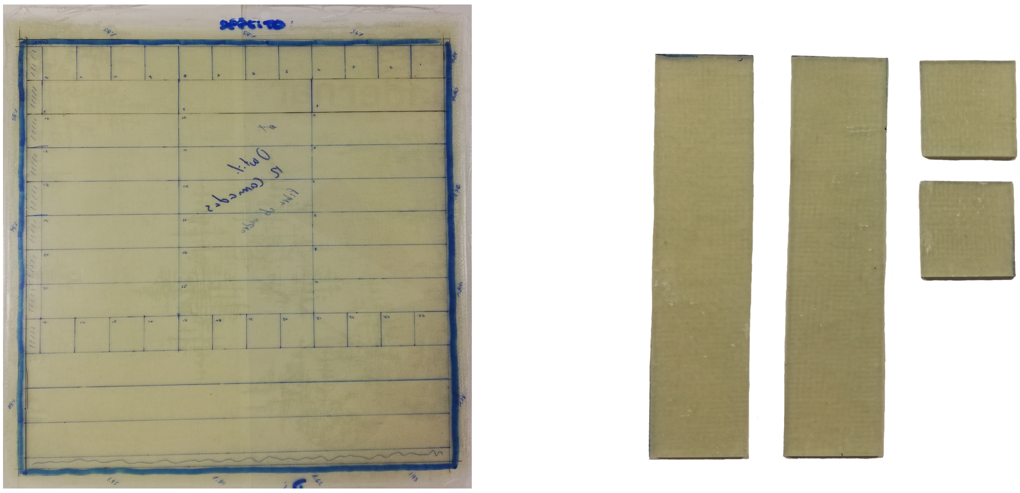
(a)

(b)

Figure 3.7: (a) Glass fiber composite marked with a pen for cutting, measuring $330 \times 330\ \mathrm{mm}^2$. (b) Pieces after cutting: two rectangles, each with $25 \times 100 \times 1.9\ \mathrm{mm}^3$, and two squares, each with $25 \times 25 \times 1.9\ \mathrm{mm}^3$ are needed for each SLJ sample.

3.2.4 SLJ samples - manufacture of SLJ with pure epoxy and epoxy-CNT nanocomposite

The manufacturing process for the SLJ samples involved pure epoxy and epoxy-reinforced nanocomposite. Thus, six specimens were fabricated for each adhesive case.

The ASTM D 3165 standard (a) states that the dimensions were the same for every joint produced. The adherends' length, width, and thickness were measured in five different places to get an average value for each dimension that was used in the mechanical tests that followed. The adherends had an average thickness of $1.9\ \mathrm{mm}$.

According to Bregar et al. (2020) findings, the sensitivity response for adhesives in SLJ was more evident for thin bonds, in their case $0.18\ \mathrm{mm}$. Based on this study and the reviewed literature in subsection 2.3.3, the studied adhesives were dimensioned for $0.2\ \mathrm{mm}$.

The previously mentioned standard outlines procedures for evaluating the strength properties of adhesives in shear by SLJ laminated assemblies tension loading. The final dimensions of the specimens are depicted in Figure 3.8.

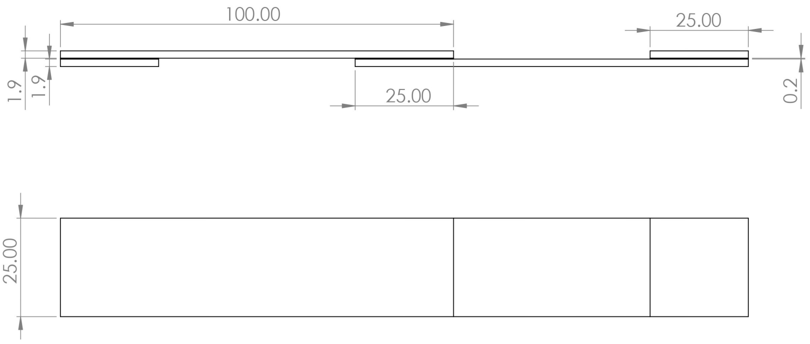

Figure 3.8: Schematic representation of the dimensions, in millimeters, of the single-lap adhesive joint specimen - side view and top view (from top to bottom).

To achieve the desired adhesive thickness, an experimental curing setup using a structure 3D-printed in PLA was developed. This setup was designed to align the adherends, end-tabs, and epoxy in the same plane, preventing specimen rotation and ensuring uniform adhesive thickness. The structure's design aimed to maintain consistency across all specimens. Figures 3.9a and 3.9b provide visual representations of the dimensions of the structure and the corresponding PLA design. For added assurance, the PLA structure was covered in a Teflon sheet to prevent the resin from adhering to the PLA structure during the curing process.

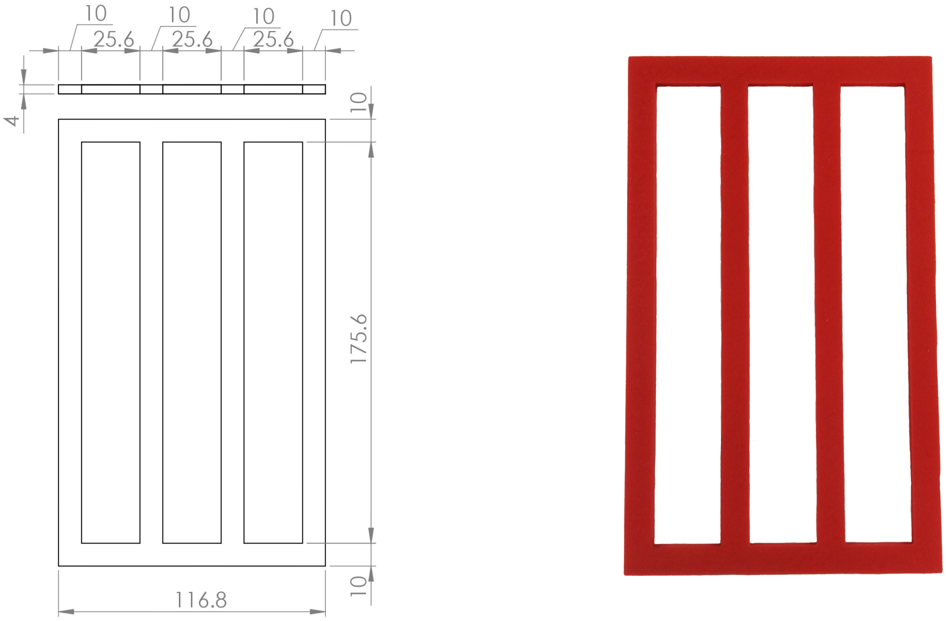

(a)

(b)

Figure 3.9: (a) Experimental curing structure for the manufacture of SLJ. Dimensions are in millimeters - front and top view (from top to bottom). (b) The final structure is PLA to support the curing of the SLJs.

The manufacturing process for the SLJs began with the preparation of the adhesives and the PLA structure. The adherends were meticulously marked with a pen to demarcate the adhesion zones between the adherends and the end-tabs to facilitate the assembly procedure. These selected regions were subjected to mechanical surface treatments to improve adhesion strength and toughness, as reviewed in subsection 2.3.4. This treatment involved manual abrasion with P100 sandpaper in random directions, followed by thorough cleaning with acetone to ensure a clean joint surface.

Following the preparation of the adherends and end-tabs, the epoxy adhesives were prepared in their pure form and with the reinforcement of CNTs. The employed bulk adhesives' manufacturing procedure was replicated for these epoxy adhesive formulations. However, an added layer of complexity emerged due to the necessity for simultaneous curing of SLJs employing distinct adhesives. Consequently, meticulous coordination was imperative to successfully carry out this stage.

The SLJ assembly process initiated by placing an adherend specimen and an end-tab specimen within the PLA structure. Using a syringe, an approximately $1\ \mathrm{mm}$ volume of epoxy resin was deposited at each joint location. Although this volume surpassed the final volume required for the expected adhesive dimensions, the experimental setup was not able to prevent adhesive leakage. The higher volume ensured that the desired adhesive area and thickness were achieved. Subsequently, the upper adherend and end-tab were slowly positioned from one edge to the other to guarantee proper bonding, avoiding residual air within the adhesion.

After assembling the adherends, end-tabs, and adhesive within the PLA structure, an acetate sheet was positioned over the structure and the joints. A load was then applied to ensure uniform pressure distribution across the joints. This final configuration is illustrated in Figure 3.10a. The curing process for the SLJs is similar to the previously described procedure for bulk adhesives. After the curing process was complete, the adhesive joints needed to be carefully removed from the PLA mold and cleaned to eliminate any epoxy leaks that may have occurred during curing.

Once the adhesive joints were cleaned and prepared, the next step involved applying silver conductive paint to create electrodes, similar to the process used for bulk adhesive samples. In this case, the electrodes were positioned at the ends of the bond line thickness. Given the irregular surface of the adhesive, there is no need for paper tape to define the electrode area. Copper wires were attached using silver paint along the adhesive length to facilitate electrical resistance measurements. Figure 3.10b shows the final product of the SLJ manufacturing process. All of the SLJs were then measured at five separate places in all dimensions. The average value in each direction yields the final dimension.

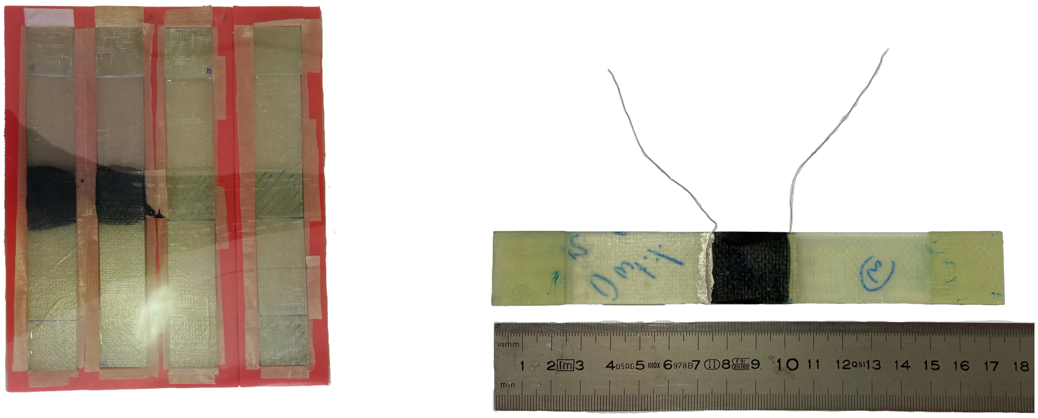

(a) (b)

Figure 3.10: (a) SLJs assembled in PLA molds during the curing process. (b) Typical SLJ specimen reinforced with CNTs. Silver electrodes and copper wires are visible and placed at the ends of the overlap joint.

Figure 3.11 provides a schematic representation of the SLJ configuration. The measurement of electrical resistance occurs between the two electrodes. Any change in electrical resistance is a result of modifications in the electrical network within the adhesive.

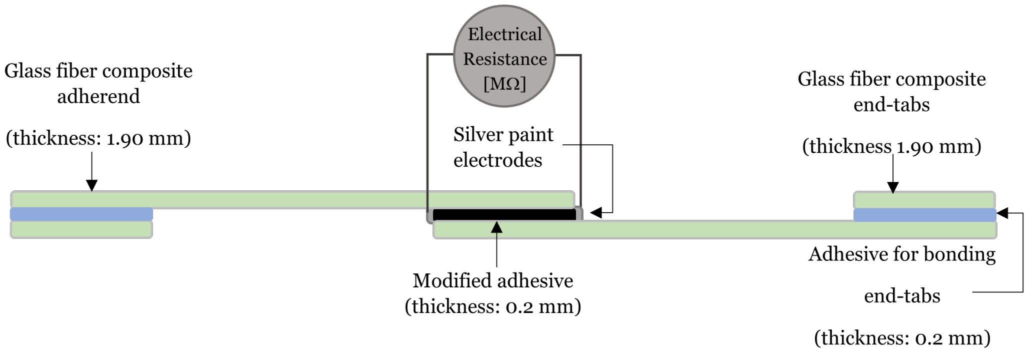

Figure 3.11: Schematic representation of a SLJ specimen and electrode arrangement for electrical resistance measurements.

3.3 Experimental procedure - sample analysis

3.3.1 Mechanical properties - flexural strength testing: bulk samples and SLJs

The three-point bending test is a mechanical assessment used to determine various properties, such as flexural strength and Young's modulus under flexural stress, by subjecting a freely supported beam (sample) to a load applied at its midpoint. The load is applied at a constant speed rate until the specimen either fractures or the deflection reaches a predetermined value. The applied force is measured throughout the test. This test procedure complies with the EN ISO 178:2003 standard (ISO (2003)). The tests were conducted at room temperature, with the span length (L_s) for the bulk adhesives determined by the standard as:

$$L_s = (16 \pm 1)\bar{h} \quad (3.1)$$

For the SLJ specimens, due to the longer length ($175\ \mathrm{mm}$) and the thicker overlap ($4\ \mathrm{mm}$), the three-point bending test was set at an average length of $150\ \mathrm{mm}$.

In the previous equation, $\bar{h}$ denotes the average specimen thickness. The test was performed with varying test speeds and maximum deflection levels to encompass a range of structural stimuli for evaluating structural sensing response. For bulk adhesive specimens, the test speeds ranged from 1 to $7\ \mathrm{mm/min}$, and the maximum deflection ranged from 0.5 to $2\ \mathrm{mm}$ at intervals of $0.5\ \mathrm{mm}$. For SLJ specimens, the test speeds ranged from 4 to $10\ \mathrm{mm/min}$, and the maximum deflections ranged from 1 to $4\ \mathrm{mm}$.

For every reinforcing loading, five specimens were examined to study the flexural strength of bulk adhesive joints. Three samples were examined for SLJs. The following formulas were used to determine flexural stress and strain, respectively, during loading:

$$\sigma_f = \frac{3FL_s}{2b\bar{h}^2}\ [\mathrm{MPa}] \quad (3.2)$$

$$\varepsilon = \frac{6s\bar{h}}{{L_s}^2} \times 100\ [\%] \quad (3.3)$$

In these equations:

where F is the applied force on the sample in N; L_s is the span length in mm; b is the sample width in mm; $\bar{h}$ is the average sample thickness in mm; s is the sample deflection in mm;

After plotting stress-strain curves, the flexural modulus, E_f, can be calculated using the following equation:

$$E_f = \frac{\sigma_{f2} - \sigma_{f1}}{\varepsilon_{f2} - \varepsilon_{f1}} \quad (3.4)$$

where

- σ_{f1} and ε_{f1}, are the flexural stress and corresponding flexural strain for a deflection s_1;
- σ_{f2} and ε_{f2}, are the flexural stress and corresponding flexural strain for a deflection s_2;

In the standard, $\varepsilon_{f1} = 0.0005$ and $\varepsilon_{f2} = 0.0025$.

The mechanical tests were conducted using a precision universal testing machine (Shimadzu, AGS-X) equipped with a $10\,\mathrm{kN}$ load cell. Data processing was facilitated through the Trapezium X software, allowing the generation of stress-strain curves, stress-time curves, and strain-time curves. The latter two are crucial for analyzing cyclic behavior and the piezoresistive response in electromechanical tests. The corresponding load was measured by the machine load cell and converted to axial stress using Equation 3.2, while the mechanical strain was calculated based on the machine's cross-head displacement.

Figure 3.12a shows the experimental setup for three-point bending tests, in this particular case for SLJs, while Figure 3.12b provides a schematic representation of the three-point bending test with corresponding components.

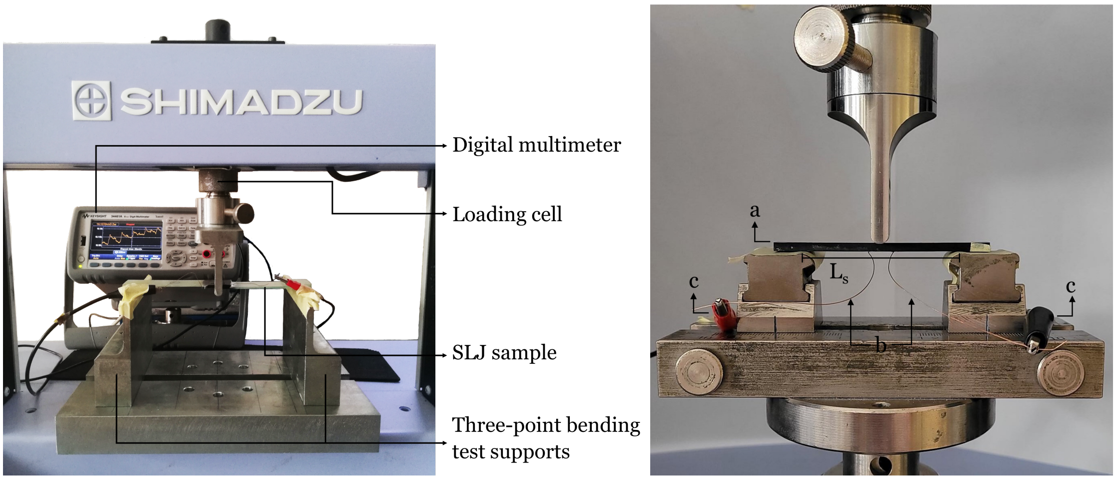

(a) (b)

Figure 3.12: (a) Three-point bending setup for SLJs specimens - $L_s = 150\ \mathrm{mm}$. (b) Schematic representation of three-point bending test for bulk adhesives: *a* - bulk adhesive sample; *b* - copper wires; *c* - crocodile clips for connecting to the multimeter; L_s - span length.

After the flexural strength test on SLJs, a visual inspection of the fracture surfaces was carried out to classify the fracture modes in the bending load condition.

3.3.2 Mechanical properties - shear strength testing: SLJs

The shear strength tests on SLJs were conducted using a precision universal testing machine (Shimadzu, AGS-X) equipped with a $50\,\mathrm{kN}$ load cell, suitable grips, and the Trapezium X software for data processing.

The experimental procedure considered was ASTM D3165 standard (a) for determining the comparative shear strengths of adhesives in large area joints. The tests were performed at a loading rate of approximately $1.3\ \mathrm{mm/min}$, ensuring compliance with the ASTM standard.

Precise alignment of the grips holding the specimens was necessary to ensure accuracy. For the specimen to remain stable throughout testing, the end-tabs had to be attached to the grips correctly. All experiments were carried out at room temperature. To improve adhesion between the specimen and the grips, P100 sandpaper was used to sand the end-tabs.

Three samples were tested to ensure the repeatability and reliability of each SLJ configuration for pure and carbon nanotube-reinforced adhesive joints. For post-testing, the software facilitated the extraction of data, enabling the generation of stress-strain curves. Subsequently, a detailed macroscopic examination of the failure surfaces was conducted to categorize the fracture modes. The tests were recorded in video using a camera, capturing multiple frames for subsequent analysis of the joint's evolution over time (refer to Figure 3.13a) to provide a comprehensive understanding of the joint's behavior. Axial stress was obtained from the load measured by the machine load cell, while mechanical strain was computed based on the machine's cross-head displacement.

The lap shear strength was determined through the following formula:

$$\tau = \frac{P}{A_0} \quad (3.5)$$

where P represents the tensile load from the cell load, and A_0 is the original overlap area. In this study, A_0 corresponded to the area resulting from the adhesive width and overlap length. τ was the shear stress to which the adhesive joint was subjected. The lap shear strength calculation used the load at the failure of the adhesive (da Silva et al. (2009)).

For calculating tensile strain in the adhesive joint, ε_t, the following formula was used:

$$\varepsilon_t = \frac{\Delta L}{L_0} = \frac{L_t - L_0}{L_0} \quad (3.6)$$

where the following terms represent:

- L_t was the distance between gage marks at any given time;
- L_0 was the original distance between gage marks;
- ΔL represented the increase in distance between gage marks (elongation).

In the case of calculating total strain at break, L_u replaces L_t, which corresponds to the distance between gage marks at the moment of rupture (based on the ASTM D638-14 standard (AST (c))).

Figure 3.13a shows the experimental setup for tensile tests, while Figure 3.13b represents a more detailed setup for the tensile test with the sample positioned in the grips.

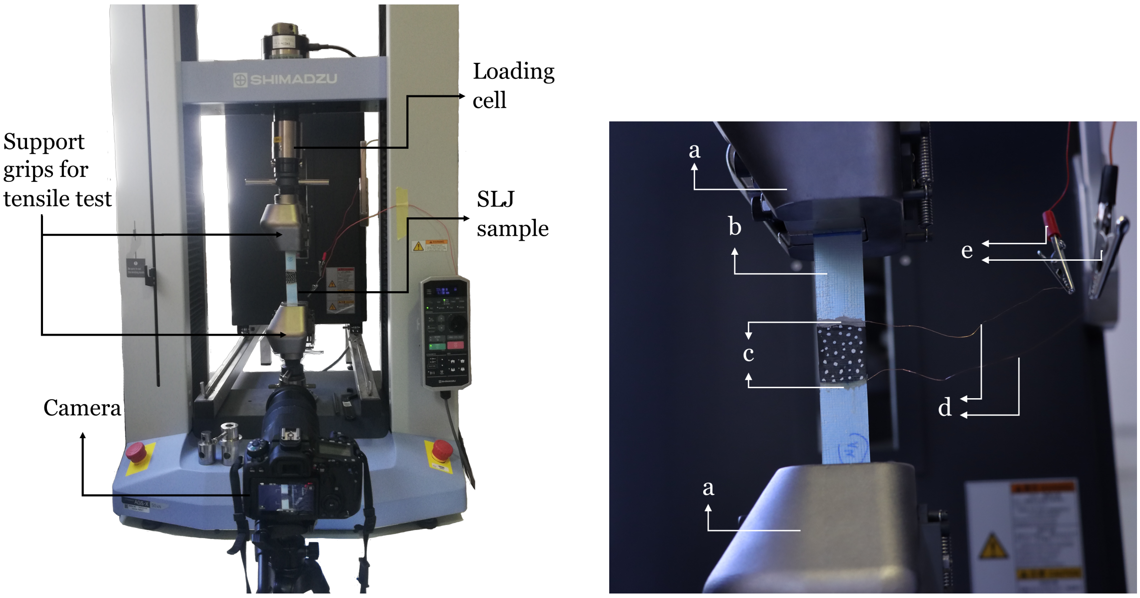

(a) (b)

Figure 3.13: (a) Tensile test setup for SLJ specimens. (b) Detailed representation of tensile test for SLJ configuration: *a* - grips; *b* - SLJ specimen; *c* - silver paint electrodes; *d* - copper wires; *e* - crocodile clips for multimeter connection.

3.3.3 Electromechanical testing - piezoresistivity study for bulk samples and SLJs

This section provides a comprehensive examination of the tests conducted to investigate electrical properties and the response of samples to mechanical stimuli. The primary objective was to optimize the loading and dispersion of CNTs within the epoxy matrix to achieve electrical resistance values in the magnitude of (MΩ).

As previously outlined in sections 3.2.1 and 3.2.3, the samples had silver paint electrodes and copper wires to facilitate electrical resistance measurements. After the fabrication of the samples, a digital multimeter (Keysight 34461A) was employed, configured to display electrical resistance values to measure the baseline electrical resistance of each specimen in the absence of any load - denoted as R_0. If these resistance values fell within the range of units to tens of MΩ, it indicated a favorable outcome and thus allowed us to progress with subsequent electromechanical testing (Chung (2016)).

The piezoresistive tests were conducted concurrently with the previously described mechanical tests to correlate mechanical and electrical responses and determine the viability of the strain sensing structure. The experimental setup included a digital multimeter for registering electrical resistance, thus enabling the piezoresistive test.

Three distinct electromechanical tests were conducted. Firstly, cyclic flexural loading tests were performed on both bulk and SLJs at diverse velocities and deflections, as outlined previously, to comprehensively evaluate the strain sensing response under a varied range of stimuli. Subsequently, load-unload cycling tests were conducted on the samples, introducing variable waiting times between the load and unload phases aiming to understand the electrical response to mechanical stimuli. Lastly, the specimens were subjected to deformation until fracture. Throughout these mechanical tests, continuous measurement and recording of electrical resistance were performed for subsequent analysis and correlation with the mechanical response.

As studied in section 2.7, piezoresistivity is an electromechanical phenomenon where a material, subjected to mechanical deformation, exhibits a change in electrical resistivity. This phenomenon arises due to variations in the electrical pathways within the epoxy matrix's electrical network.

This property is of paramount importance in the construction of the strain sensing adhesive. It aims to establish a mechanical stimulus-response relationship by inducing mechanical deformation and monitoring the corresponding change in electrical resistance. This correlation between mechanical strain and electrical resistance validates the functionality of the strain sensing adhesive.

As previously mentioned in section 3.3.1, the mechanical tests were performed using a precision universal testing machine as the source of cyclic mechanical input for inducing specimen deformations. During the mechanical tests, the digital multimeter was connected to the copper wires of the sample with crocodile clips. The specimens with CNTs were insulated at the ends with paper tape to avoid direct contact with metal supports in the three-point bending test configuration, to improve the quality of the electrical signal and eliminate interference.

Both mechanical and electrical resistance measurements were recorded on a per-second basis. The multimeter employed a two-probe method for electrical resistance acquisition. The parameter time will permit the establishment of a direct relation between electrical and mechanical measurements.

The arrangement for bulk adhesive samples and SLJ in three-point bending tests is illustrated in Figure 3.12, while the configuration for SLJ tensile tests is depicted in Figure 3.13. The specimens had their electrodes facing downward in a three-point bending test to protect them from potential damage during bending tests. Crocodile clips were connected to the copper wires of SLJ and bulk adhesive samples during the mechanical tests. These clips were then connected to the multimeter, enabling continuous tracking of electrical resistance during cyclic loading.

Consistent with the approach in mechanical testing, the aim here is to monitor electrical resistance during cyclic flexural tests conducted at various velocity rates and deflections. This comprehensive range of testing conditions aimed to assess the capacity of the piezoresistive strain sensing adhesive to respond across a variety of mechanical scenarios.

After the completion of the data acquisition process, the collected data required further processing. Electrical resistance measurements were acquired from the multimeter on a per-second basis. To evaluate the sensitivity of the sensing adhesive, the normalized electrical resistance ($\Delta R/R_0$) was calculated, where $\Delta R = R - R_0$. Subsequently, the sensitivity was determined by dividing this calculated value by the applied strain, obtaining the gauge factor (GF) value, as described in Equation 2.3.

This comprehensive analysis aimed to establish a direct correlation between the mechanical deformation and the corresponding electrical response, demonstrating the electromechanical sensing performance.

Chapter 4

Results and Discussion

4.1 CNT modified bulk adhesive's optimization

In this section, the focus is on optimizing CNT reinforcement in epoxy resin. This optimization corresponds to the improvement of the electromechanical properties compared to pure epoxy, with a specific emphasis on the GF parameter. The primary objective was to find the optimal concentration of CNT filler, balancing the nanocomposite's mechanical, electrical, and sensing capabilities. The evaluation will be based on samples subjected to flexural strength tests, followed by a study of the piezoresistive response through electromechanical tests. The most promising reinforcement loading identified in these tests will be further investigated in subsequent electromechanical tests. The obtained results will be thoroughly discussed and supported by relevant references from the literature.

4.1.1 Comparison of mechanical properties under flexural stress for different reinforcement filler loadings

A static bending test was carried out to extract key mechanical parameters, such as flexural modulus, peak load, and ultimate breaking load, to assess the impact of CNTs on adhesive samples. These parameters were identified across different filler loading concentrations (0.25 wt.% and 0.50 wt.%) and with pure epoxy resin. This approach provides a comprehensive understanding of the flexural stress behavior compared to pure epoxy. The stress-strain curves in Figure 4.1 illustrate typical three-point bending responses for different samples: pure epoxy, 0.25 wt.%, and 0.50 wt.% CNTs. The three-point bending test was executed at a velocity of $5\ \mathrm{mm/min}$ until failure. The plotted curves depict the average value of five tested samples for each filler loading, with error bars indicating the standard error calculated from the standard deviations for flexural stress at break.

Regardless of the weight content of CNTs, all the stress-strain curves exhibit a linear increase in flexural stress with strain, followed by a non-linear behavior in which the maximum flexural stress is reached. Subsequently, the bending stress decreases until the material ultimately fractures.

The findings displayed in Figure 4.1 demonstrate significant variations in the investigated samples' flexural characteristics. In comparison to the 0.50 wt.% CNT specimens, the flexural strength values of the pure epoxy and 0.25 wt.% CNTs samples are lower.

Compared to the pure epoxy samples, the stress-strain curves for the 0.25 wt.% CNT samples show similar linear behavior in the elastic regime. In contrast to the pure epoxy, the 0.25 wt.% CNT samples show decreased elongation and higher final flexural strength. In contrast to the pure epoxy, the 0.50 wt.% CNT samples exhibit a decrease in elongation at maximum stress together with an increase in maximum flexural stress and stiffness.

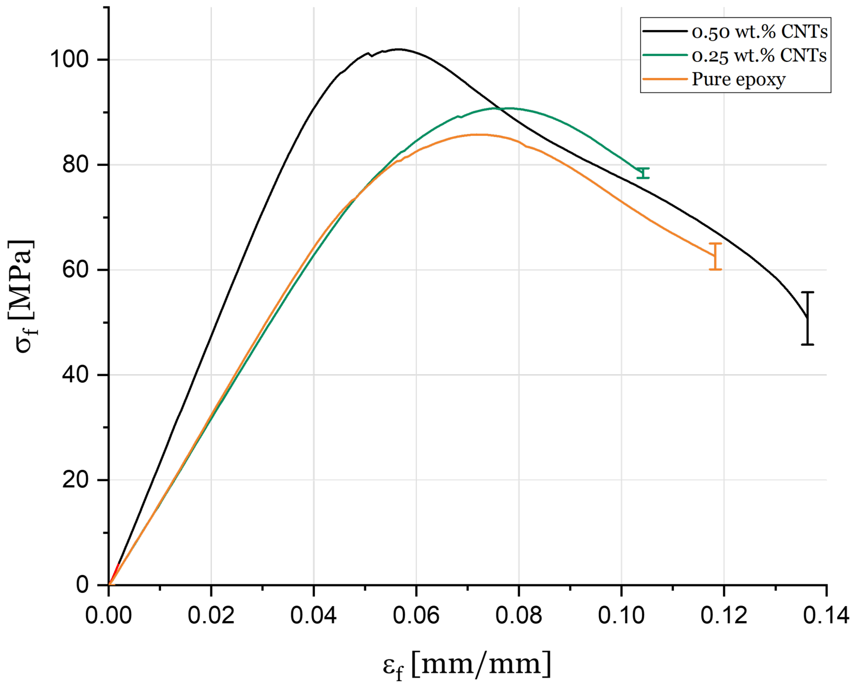

Figure 4.1: Average flexural stress-strain curves for bulk adhesive samples with varying CNT loadings.

The reinforced epoxy with CNTs enhances the plastic response of the modified adhesive with 0.50 wt.% CNTs, consequently increasing the toughness behavior of this adhesive compared to pure epoxy. The elastic limit for pure epoxy is reached at a flexural strain of approximately $\varepsilon_f = 0.048\,\mathrm{mm/mm}$ with a flexural stress of $73.4\,\mathrm{MPa}$. The 0.25 wt.% reinforced bulk adhesive shows similar elastic limit parameters. However, there is a noticeable difference in adhesives loaded with 0.50 wt.% CNTs, where the elastic limit is reached at a flexural strain of $\varepsilon_f = 0.039\ \mathrm{mm/mm}$ with a flexural stress of $89.1\ \mathrm{MPa}$. These values correspond to a decrease in elastic limit strain (elongation) and an increase in flexural limit stress compared to pure epoxy. Compared to a pure epoxy case, these data support the enhanced stiffness with the reinforcing loading.

This observation aligns with the findings in the work by Ejaz et al. (2022), which also reported that the reinforcement with CNTs increases the plastic response of the modified adhesive and consequently enhances adhesive toughness behavior. Their work also highlighted an increase in failure stress, consistent with what was observed between pure epoxy and the 0.50 wt.% loaded samples. However, the reduction in the flexural strain elastic limit, as reported in the previous work, is attributed to CNT incorporation. It is possible to observe a ductile failure response for reinforced bulk adhesive with 0.50 wt.%, similar to the results of Bregar et al. (2020). The prior author attributes this behavior to the CNT bridging mechanisms.

Figure 4.2 shows the maximum flexural stress for each filler content and pure epoxy, as well as the corresponding flexural strain. When compared to pure epoxy bulk adhesive samples (85.7 MPa), these results show an approximately 18.9 % increase in maximum flexural stress for 0.50 wt.% CNTs reinforcemnt and a 5.82 % increase for the 0.25 wt.% CNTs samples.

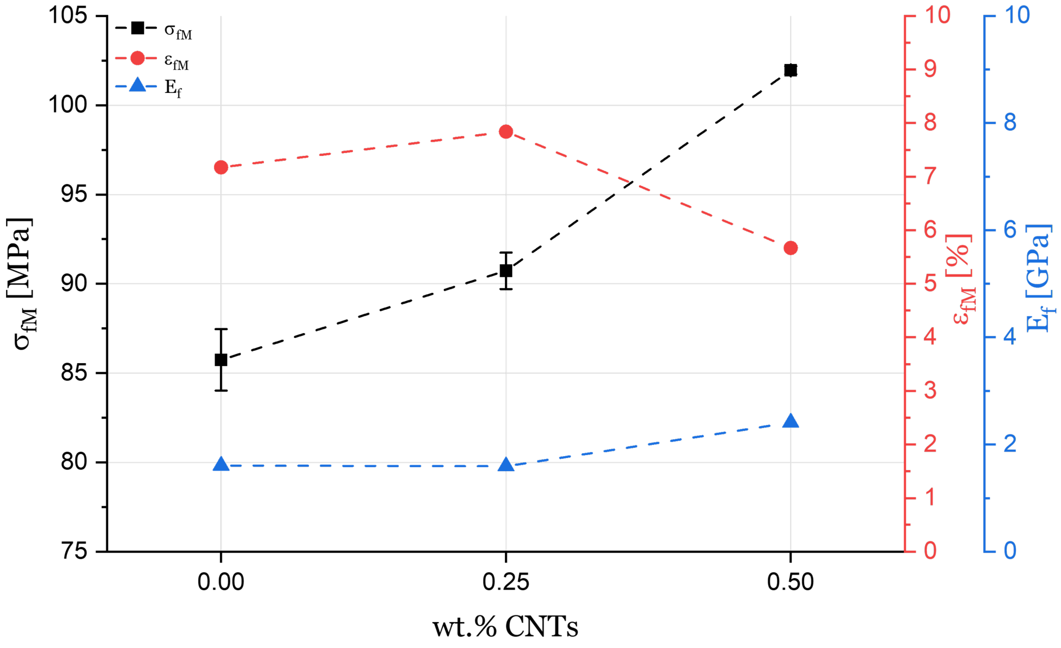

Figure 4.2: Flexural properties (strain at maximum stress (ε_{fM}), maximum stress (σ_{fM}), and flexural modulus (E_f)) are characterized by average curves as a function of CNT weight content in bulk adhesive samples.

Additionally, the flexural strain for maximum flexural stress demonstrates an increasing trend with rising filler loading, progressing from pure epoxy to 0.25 wt.% (9.27 %). However, for the 0.50 wt.% samples, the strain value for maximum stress decreases to a value lower than that for pure epoxy, approximately 21.0 % ($\varepsilon_{fM} = 5.67$ %). These findings indicate a reduction in elongation for higher-loading contents. Thus, up to 0.25 wt.% CNTs, the trend is increasing, but for higher loadings, there is a decrease in elongation. The error bars represent the standard error calculated from the standard deviations for the maximum flexural stress.

Besides, the flexural modulus (E_f) was calculated and is presented in Figure 4.2. A reduction in the flexural modulus of 0.74 % (from 1.61 GPa to 1.59 GPa) is observed between the filler content of 0.25 % of CNTs and pure epoxy. In contrast, for 0.50 wt.% CNTs, there is an increase in the flexural modulus from 1.61 GPa to 2.41 GPa compared to pure epoxy, indicating a 50 % increment. This value shows an increase in stiffness for the nanocomposite reinforced with 0.50 wt.% of CNTs compared to pure epoxy.

It is evident from a comparison of these mechanical results with those found in Santos et al. (2023) for pure epoxy that the values from this study are lower. Variations in experimental methodologies or possible defects in the manufacturing process could be the cause of this discrepancy. It is noteworthy, nevertheless, that the trend of better mechanical characteristics with CNT addition is consistent with findings from Santos et al.'s investigation. Similar results are also reported in the work by Konstantakopoulou and Kotsikos (2016), where they concluded that the dispersion process and the content of MWCNTs significantly influence mechanical properties.

A decrease in stiffness for the reinforced nanocomposite with 0.25 wt.% CNTs is observed by the lower flexural modulus compared to pure epoxy. In this case, the increase in elongation and maximum flexural stress demonstrates that the CNT particles promote a more elastic behavior with a greater propensity to bend. The less favorable outcomes for pure epoxy, in contrast to the outcomes reported by Santos et al. (2023), might be linked to variations or defects in the manufacturing process. The observed trend in the reinforced nanocomposite could also be a consequence of inefficient filler dispersion within the matrix. In such cases, filler particles may act more as defects than reinforcement agents, contributing to weaker mechanical properties. These results underscore the crucial role of achieving proper dispersion and bonding of nanofillers within the polymer matrix to fully exploit their potential for enhancing material properties. A homogeneous filler dispersion and particle alignment are essential for a piezoresistive response with improved sensitivity and linearity, as emphasized in the work of Duan et al. (2020). Konstantakopoulou and Kotsikos suggests that an extended sonication process might not be the most effective approach to achieve these desirable properties.

4.1.2 Comparative analysis of electromechanical results in flexural strength for different filler loadings

Figure 4.3 provides a clear comparison between the mechanical response (flexural stress) and the corresponding piezoresistive measurements (normalized change in electrical resistance) concerning flexural strain. This comparison is made for bulk adhesive samples containing 0.25 wt.% and 0.50 wt.% of CNT loading. The mechanical curves represent the average response of the five tested samples. For all samples, the electrical resistance during the resting condition was measured, and the conductivity was calculated, showing a value between 10^{-5} S/cm and 10^{-6} S/cm, which places the samples in the semiconductor category (Hummel (1993)). The electrical resistance graphs are representative curves for the two percentages of tested particles.

This graphical representation helps to visualize the relationship between mechanical stress and electrical resistance changes, providing valuable insights into the piezoresistive behavior of the adhesive samples with different CNT loading levels. Furthermore, the figure presents two extra linear approximations. The linear fit for the fractional change in resistance within the elastic and plastic regimes is shown for 0.50 wt.% filler loading, indicating the regions where the piezoresistive response presents the linear and non-linear mechanical behavior.

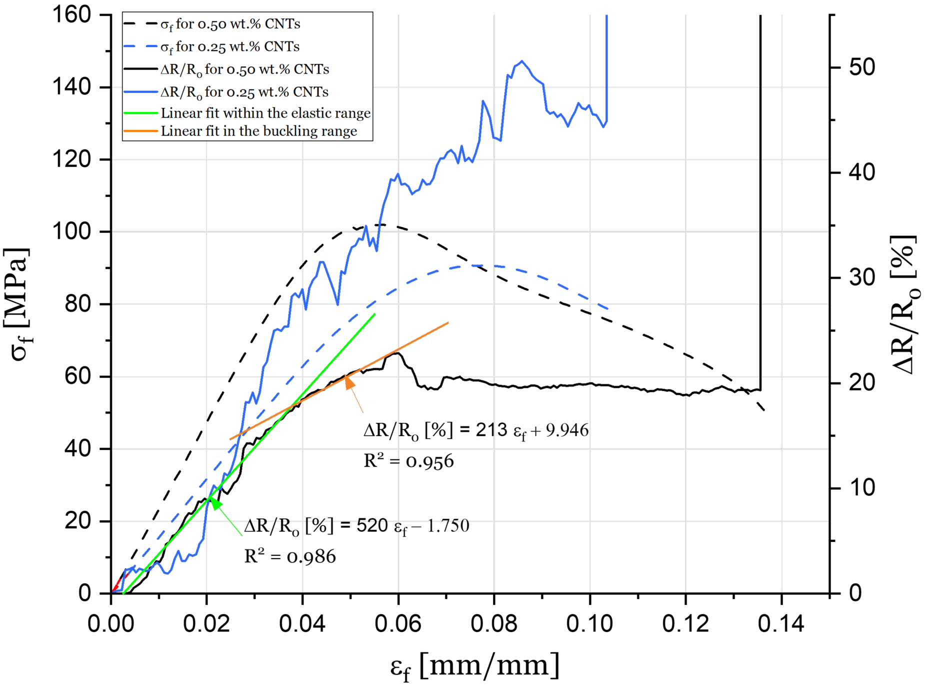

Figure 4.3: Average curve depicting mechanical response and a representative normalized curve for change in electrical resistance relative to flexural stress until failure as a function of flexural strain for bulk adhesive samples loaded with 0.25 wt.% and 0.50 wt.% of CNTs. A linear adjustment of the electrical resistance variation in two segments is shown for the elastic and the plastic regime.

In the adhesive samples with 0.50 wt.% of CNTs, the piezoresistive measurements are approximated by two linear segments, similar to the findings of Yao et al. (2017) for bending stress. The first linear segment, characterized by a steeper slope, corresponds to the elastic range, while the second, with a less steep slope, represents the plastic range. The point where these two linear segments intersect indicates the material elastic limit.

The elastic limit was determined for flexural stress of 89.1 MPa and a corresponding flexural strain of 0.039 mm/mm for the mechanical test. For the intersection of the linear approximations, the normalized resistance is $\Delta R/R_0 = 17.4$ % for a strain value of 0.038 mm/mm. Remarkably, there is only a difference of 3 % between the electrical prediction and the mechanical value for the elastic limit. This value demonstrates the potential and accuracy of the nanocomposite's sensing capabilities for structural damage.

The observation that the normalized electrical resistance remains relatively constant or even slightly decreases for deformation values above 0.060 mm/mm suggests significant structural damage within the adhesive. This result aligns with similar findings explained by Bregar et al. (2020), who attributed such results to the alignment of CNTs under extensive loading on bulk samples, leading to increased conductivity. In the specific case of this study, while the increase in conductivity is not as pronounced, the explanation provided by Bregar et al. (2020) justifies the minor reduction in electrical resistance. Beyond this strain value, piezoresistivity is not significantly affected by tunneling, as the increment in strain does not considerably impact the normalized electrical resistance. This result suggests that the electrical network is significantly affected, and the recorded electrical resistance value mainly reflects the accumulation of damage rather than variations in the electrical network due to neighboring CNTs.

Similar findings were described by Daliri et al. (2020), who reported that the abrupt increase in electrical resistance is attributed to permanent and visible damages, while the constant $\Delta R/R_0$ corresponds to the accumulation of damage caused by microcracks in the joint.

In cases of complete failure, the normalized resistance becomes infinite. This value occurs when the sample experiences breakage, preventing the passage of current flow between the two electrodes. This phenomenon is observed for the 0.25 wt.% CNTs at approximately $\varepsilon_f = 0.10$ mm/mm and for the 0.50 wt.% CNTs at a value slightly above $\varepsilon_f = 0.13$ mm/mm.

Overall, these findings highlight the potential of the adhesive with 0.50 wt.% CNT loading as a piezoresistive sensing structure for structural health monitoring, especially in detecting early-stage damage within the material since it is possible to observe the elastic limit according to the bilinear law for flexural stress described by Yao et al. (2017).

The bulk adhesive with 0.25 wt.% loading does not exhibit a clear and distinctive piezoresistive behavior, as observed in previous studies and the 0.50 wt.% CNT reinforcement. Despite showing a trend for a bilinear approximation, the electrical resistance results exhibit considerable noise. Consequently, differentiating between the various deformation regimes using this loading system poses a challenge and is more susceptible to errors. Due to the noisier signal, the GF calculation was not obtained for the 0.25 wt.% tested sample. On the other hand, the elastic regime for the 0.50 wt.% sample shows a calculated GF value of 5.20, which corresponds to flexural strain values between 0 mm/mm and 0.038 mm/mm. As highlighted in the Yao et al.'s works, the GF for the plastic regime will be lower. In this case, this corresponds to a value of 2.13, between a flexural strain of 0.038 mm/mm and 0.06 mm/mm.

To further investigate the sensing capabilities of both filler percentages, cyclic loading tests were conducted with deflections below the elastic limit for each loading percentage. This approach allows the exploration of piezoresistive behavior in the samples. The study follows the methodology outlined in Lim et al. (2011), where cyclic tests enable the examination of electrical resistance-deformation behavior with progressive damage and the differentiation between permanent and reversible electrical resistance changes.

Figure 4.4 presents data on flexural strain (shown in black on the left axis) and the corresponding normalized electrical resistance values (depicted in red on the right axis) over time for both loading percentages at different maximum strain values shown in the plot. For each loading percentage, the mechanical and normalized electrical resistance curves shown in the figure are representative curves from a single tested specimen. The testing was carried out cyclically at a speed of $5\ \mathrm{mm/min}$. For easy comparison, these strains are shown in the same figure even though they were not tested in the same experiment.

This approach provided insights into how the electrical resistance changes during cyclic loading for different strain values below the elastic limit, which clarifies the piezoresistive properties of adhesive samples at distinct levels of deformation. Cycles of increasing and decreasing flexural strain are evident in both situations. The associated variations in piezoresistivity reflect these changes in mechanical strain. However, in Figure 4.4a, despite having a trend, there is no clear pattern in these variances for the 0.25 wt.% samples.

For lower maximum deformation values (approximately $\varepsilon_f = 0.444$ %), resistance peaks are visible during the resting state. The state with maximum deformation shows the lowest value of normalized electrical resistance, implying a negative piezoresistive response. For intermediate strain levels (around $\varepsilon_f = 0.887$ %), the piezoresistive behavior response is inconclusive, marked by substantial noise. But the trend of the curve shows similarity with negative piezoresistivity. The following cyclic test with maximum deformation $\varepsilon_f = 1.330$ % for the first cycle shows a trend towards positive piezoresistivity, but the response is characterized by substantial noise.

Higher strain values (approximately $\varepsilon_f = 1.774$ %) show a reduction in the electrical resistance noise, and the electrical response becomes more aligned with the mechanical strain. For this strain level, the electrical resistance shows peaks for maximum and minimum strain values, suggesting the repeatability that follows the strain cycles.

This graph does not show linear behavior or a repeatable signal with cyclic loading at different maximum strain intervals, nor does it show an increase in normalized electrical resistance with increasing maximum bending strain, as reported in the literature, especially when comparing maximum strains of 0.887 % and 1.330 %.

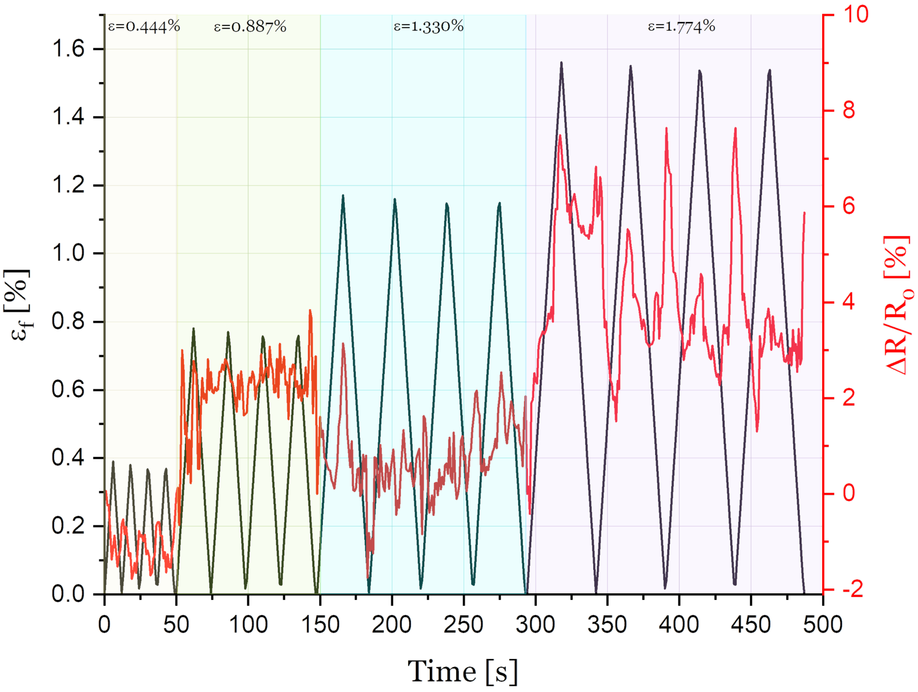

(a)

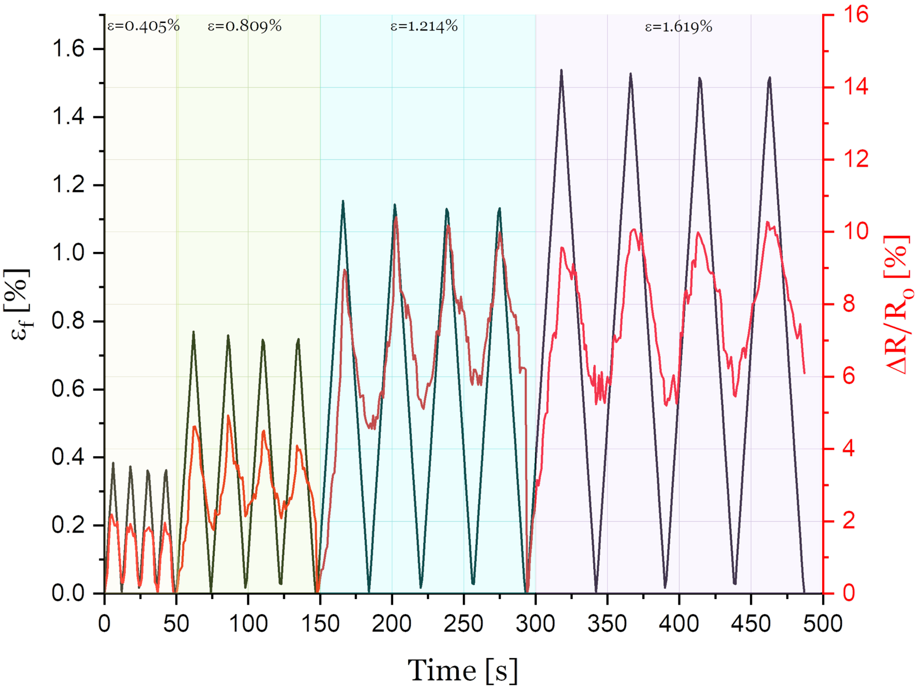

(b)

Figure 4.4: Representative curves illustrating normalized piezoresistive response during cyclical flexural loading of bulk adhesive specimens at various strain levels for (a) 0.25 wt.% CNTs loading and (b) 0.50 wt.% CNTs loading.

While these curves exhibit trends in electrical response, it is important to note that this behavior does not offer a clear outcome suitable for analysis as a piezoresistive sensing structure throughout the entire deformation range. Nevertheless, the strains corresponding to approximately 10 % and 40 % of the value of the limit deformation of the elastic regime ($\varepsilon_f = 0.444$ % and $\varepsilon_f = 1.774$ %, respectively) appear to yield better responses.

The piezoresistive response is considerably more precise for the sample containing 0.50 wt.% CNTs (refer to Figure 4.4b). It closely mirrors the fluctuations in mechanical strain, displaying a positive piezoresistive behavior for all tested maximum strains. Notably, as there are peaks in the mechanical deformation measurements, corresponding peaks in electrical resistance are also observed. This pattern is consistent for the resting state (unload condition) and the lowest electrical resistance values.

Furthermore, the normalized electrical resistance value exhibits a relationship with the maximum applied strain, particularly for the lowest examined strain level ($\varepsilon_f = 0.405$ %), where the change in the normalized electrical resistance peaks are approximately $\Delta R/R_0 = 1.9$ %. For intermediate strain levels ($\varepsilon_f = 0.809$ % and $\varepsilon_f = 1.214$ %), the piezoresistivity reaches a maximum value of approximately 5 % and 9.8 %, respectively. On the other hand, for the highest considered strain value ($\varepsilon_f = 1.619$ %), the piezoresistivity is similar to the previous strain value, with $\Delta R/R_0 = 10.0$ %. The evaluated strain values correspond to approximately 10, 20, 30, and 40 % of the limit strain value of the elastic regime.

Evaluating the previous results, the lack of increase in normalized electrical resistance variations between the flexural strains of 1.214 % and 1.619 % is likely related to the percolation network within the nanocomposite. This could be a result of specific conformations or the interplay between the destruction and reconstruction of the conductive network within the nanocomposite due to tensile stress in the longitudinal direction and compression in the transverse direction. This mechanical behavior can account for the absence of an increment in normalized electrical resistance, leading to a behavior similar to that observed at the previously tested maximum strain level. This explanation finds support in the work of Pérez et al. (2016).

Comparing these results, the 0.25 wt.% sample shows promise for detection at both lower and higher tested strain limits. However, the electrical response does not align well with the mechanical stimulus for intermediate strain values. These findings indicate that, with improvements in manufacturing processes, sample testing, data acquisition, and post-data treatment, this loading percentage could potentially yield better sensing results due to its promising characteristics. On the other hand, the prevalence of both positive and negative piezoresistive responses suggests an interplay between the creation and interruption of CNTs' conduction mechanism, enhanced by tunneling in both the longitudinal and transverse directions of the tested sample.

In contrast, the 0.50 wt.% reinforcement shows promising mechanical behavior, featuring a higher flexural modulus and ultimate flexural strength. Furthermore, it can identify both the elastic and plastic regimes under static loading using electrical measurements. When subjected to cyclic loads in the elastic regime, this load percentage showed a significant sensitivity response. It allows the identification of variations in strain for consecutive loading cycles and produces distinct electrical responses for different maximum strain values. Additionally, as observed in the study by Vertuccio et al. (2016) for flexural stress, the electrical resistance varies in intensity with the increase in strain, and the maximum value achieved for each level of deformation remains consistent across multiple cycles. On the other hand, these results also show a continuously monitoring linearity of piezoresistivity during cyclic loads similar to what is observed in Bregar et al. (2020)'s work. This result is an essential quality that could be used for bonded structures with the need for monitoring.

It is important to note that when observing the mechanical loading, the values for the unloading state do not correspond to zero strain for both cases (see Figure 4.4a and 4.4b). This discrepancy can be attributed to the need for higher initial loading at the beginning of the test to prevent small movements of the specimen within the testing setup. This residual strain value results in residual normalized electrical resistance.

The behavior of $\Delta R/R_0 = 0$ % after each loading cycle in the unloading state, as seen in works like Vertuccio et al. (2016), Spinelli et al. (2018), and Spinelli et al. (2020) for sensing structures with 0.50 wt.% MWCNTs reinforce the idea that no significant permanent deformation has occurred in the specimen. These results are also consistent with the work of Moriche et al. (2016) for self-monitoring graphene/epoxy nanocomposites, where the strain capability was reversible with no hysteresis for at least 50 cycles.

However, for the strain variation observed in Figure 4.4a and Figure 4.4b, a higher residual resistance prevails for higher strain values in the elastic regime. According to Spinelli et al. (2018), this residual value in electrical resistance fraction increases with the plastic damage accumulated in the matrix. However, this explanation is not aligned with the obtained results since the developed work is conducted in the elastic regime.

In this case, the sensitivity and linearity were ensured, but not the reversibility of the piezoresistivity, even without compromising the elastic limit obtained for the respective samples. The residual electrical resistance measurements may result from the observed residual strain mentioned earlier. Moriche et al. (2016) also points out that the differences observed in the electrical resistance ratio when the sample is fully recovered can be caused by the measuring equipment and the associated error in the recorded electrical resistance. On the other hand, some results suggest a variable electrical resistance concerning the cycle number, indicating a conformation of the material within the nanocomposite system without compromising the structure with damage. Lim et al. (2011) also verified an increase in the baseline resistance after each load cycle during the elastic limit. According to Pérez et al. (2016), the piezoresistive behavior during the first loading-unloading cycle can be hysteretic and different from that of the subsequent cycles, suggesting a reorganization of the matrix chains and MWCNT network during the first cycle. After the first loading-unloading cycle, the piezoresistive and mechanical behavior of the composites becomes repeatable, with a constant value of electrical resistance upon unloading and small hysteresis. This justification explains the first value of electrical resistance being lower than the subsequent values registered for the unload condition in the following cycles.

Given these observations and considerations, this study will primarily focus on the electromechanical analysis of nanocomposites reinforced with 0.50 wt.% CNTs for application in piezoresistive sensing adhesives.

4.1.3 Electromechanical tests for studying piezoresistivity sensing in bulk adhesive specimens

Following the selection of the filler percentage, extensive electromechanical studies were conducted to characterize the piezoresistive sensing adhesives.

In the previous section, it was observed that the adhesives with 0.50 wt.% CNTs exhibited a positive piezoresistive response in the elastic regime. Moreover, it was noticed that the piezoresistive relationship became more pronounced with higher strain values in the elastic regime, establishing a clear correlation between strain and piezoresistive response.

To delve further into the performance of these sensing structures during flexural tests, the bulk adhesive samples were subjected to varying flexural velocities to investigate the impact on the piezoresistive response. These findings would significantly influence test conditions moving forward.

For this study, a flexural strain value of $\varepsilon_f = 0.809$ % was set, corresponding to a deflection of $1\ \mathrm{mm}$ on the universal testing machine. Different loading cell velocities were tested, ranging from 1 to $7\ \mathrm{mm/min}$. These speed values were established consecutively based on the electrical results obtained in each case.

The flexural strain and piezoresistivity over time for various loading cell velocities are represented in Figure 4.5. The objective is to identify patterns or relationships between velocity and piezoresistivity behavior. For easy comparison, these velocities are shown in the same figure even though they were not tested in the same experiment.

For the piezoresistivity response, it is evident that at all tested velocities, there is a consistent correlation between electrical resistance measurements and strain variation. The strain-sensing adhesive effectively captures the cyclic behavior and corresponds to the same linear pattern during loading and unloading. Notably, a reduction in electrical signal noise with increasing velocity was observed. This reduction is attributed to the shortened time per strain cycle, resulting in fewer collected data points as the acquisition program records one point per second. Therefore, higher velocities were not tested due to the limited number of acquired data points.

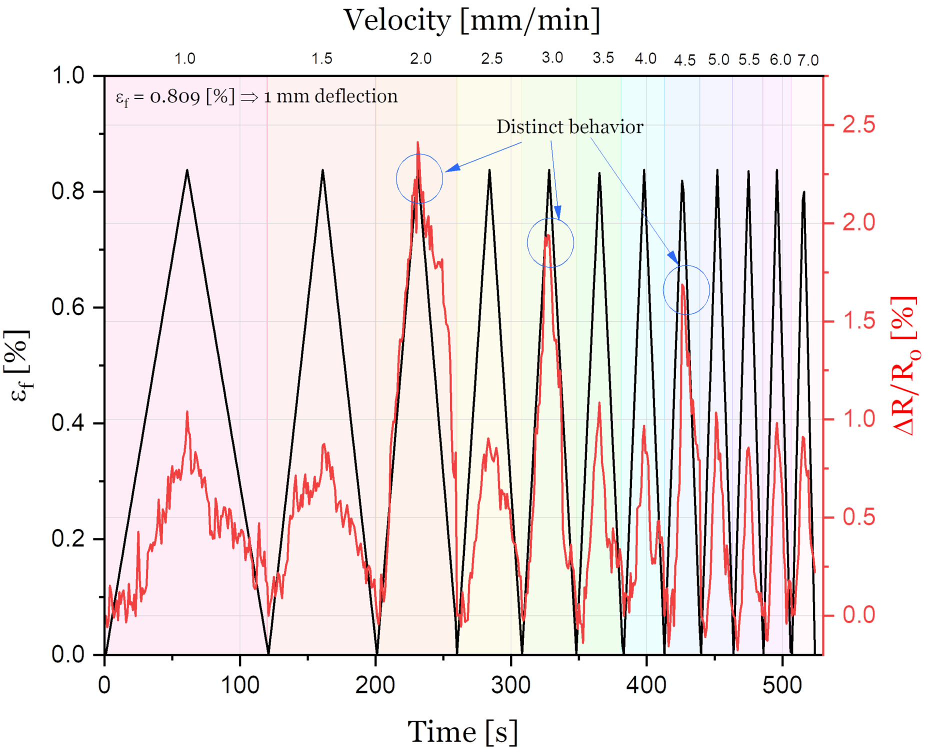

Figure 4.5: Representative curves depicting piezoresistive measurements at a fixed flexural strain ($\varepsilon_f = 0.809$ %) and variable loading cell velocity in a three-point bending test for bulk adhesive specimens reinforced with 0.50 wt.% CNTs.

Observing the plot, the normalized electrical resistance variation ($\Delta R/R_0$) remains approximately 1 % for all velocities, except for three specific values (2, 3, and 4.5 $\mathrm{mm/min}$), where the variation is slightly different, reaching ratios of 2.4 %, 1.9 %, and 1.7 %, respectively. These variations can be attributed to isolated electrical measurements influenced by small movements in the three-point bending configuration or laboratory disturbances, as these results show no other patterns or relationships between them.

It is important to note that the linearity of the piezoresistive response is notable. Even for lower velocities where the noise is higher, the curve trend still shows a linear behavior following the mechanical deformation. Additionally, these tests show recovery, not presenting residual electrical resistance between different velocities. This result could happen due to the same deformation input in the samples, which does not result in a different conformation of the matrix/filler system. Thus, for the tested velocity range, this parameter does not affect the percolation network within the nanocomposite.

In conclusion, based on these results, the experiments indicate that, for three-point bending tests, the velocity of the loading cell does not significantly impact electrical resistance measurements.

The following electromechanical tests were carried out at a velocity of $5\ \mathrm{mm/min}$ for strain monitoring. This speed was selected to achieve a balance between reducing noise and obtaining an adequate number of data points. At this velocity, the normalized electrical resistance value is around 1 %, providing a signal with minimal noise and sufficient data points to capture the electrical signal's behavior. In the subsequent test, the samples underwent 100 cycles of flexural strain below the elastic limit to observe the evolution of piezoresistive behavior over a finite number of strain cycles.

Figure 4.6 illustrates the flexural strain cycle applied within a strain range of $0 < \varepsilon_f < 8.09 \times 10^{-3}$, along with the normalized electrical resistance percentage as a function of time for a representative sample. The selected maximum flexural strain corresponds to a strain of 20 % of the elastic limit strain, chosen for its reduced noise and well-defined peaks compared to other tested strains. The signal trend for the normalized electrical resistance measurement summarizes the fundamental variations in the electrical signal and helps with signal interpretation.

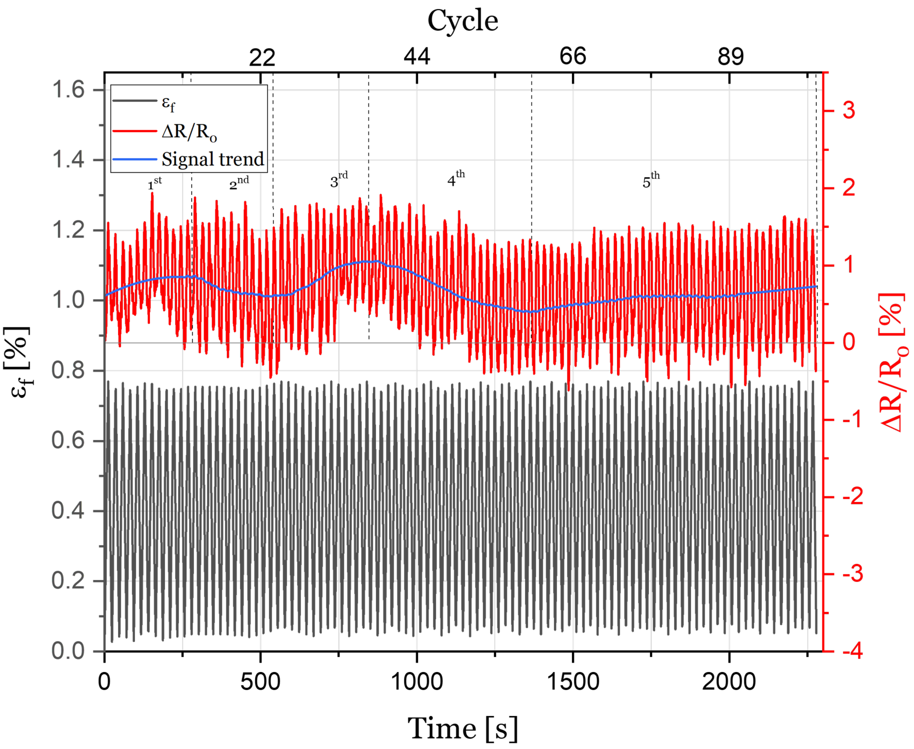

Figure 4.6: Representative curves depicting long-term stability of bulk adhesive samples with 0.50 wt.% for 100 cycles (2278 seconds) under flexural tests.

The plot is segmented into five sections, each marked by dashed lines and numbered for reference, based on variations in signal trend. The changes in electrical resistance reported below correspond to variations within the time segment referred to:

1. Cycles 1-13 (0-290 seconds): In this initial segment, lasting approximately 290 seconds, the electrical resistance trend exhibits an increasing behavior. The amplitude of the electrical signal increases by around 20 % from the first to the 13^{th} cycle. Notably, there is a noticeable residual resistance during this segment, which follows the increasing signal trend. The line representing $\Delta R/R_0 = 0$ % also evidences an increasing residual resistance.

2. Cycles 13-24 (290-535 seconds): During this period, the signal trend shifts to a decreasing pattern. The amplitude of the electrical signal decreases, albeit less significantly (2 %), relative to the 13^{th} cycle. The residual resistance during this phase exhibits a decreasing trend in alignment with the signal trend. This segment even results in null or lower values for $\Delta R/R_0$, suggesting that for higher loading cycles, the piezoresistive value at the resting state tends to be lower, leading to a negative ratio $(R - R_0)/R_0$.

3. Cycles 24-38 (535-856 seconds): The third segment shows a steeper slope than that observed in the first part of the plot, occurring between cycles 24 and 38. The amplitude of the electrical signal decreases by 42 % compared to the 24^{th} cycle. The residual resistance begins to increase, reaching a maximum value of 0.63 %. However, the maximum values of piezoresistivity do not grow at the same rate, justifying the reduction in amplitude.

4. Cycles 38-60 (856-1357 seconds): The fourth section of the plot displays a negative slope of the electrical signal trend, with a 69 % amplitude increment between cycles 38 and 60. This segment spans approximately 500 seconds.

5. Cycles 60-100 (1357-2278 seconds): The final segment is the longest-lasting, and during this phase, the electrical signal trend settles at a lower slope, showing a stabilization behavior. The signal amplitude remains relatively constant (the difference between cycle 60 and cycle 100 is less than 0.6 %). Notably, the electrical resistance value is lower than the initial R_0 value at the beginning of the test for the rest state. Consequently, the residual electrical resistance is negative, indicating that with an increase in testing cycles, the electrical resistance of the sample tends to decrease.

The varying behavior of samples during cycles, as reported in Moriche et al. (2016), is related to changes in the electrical network within the composite material. Quijano et al. (2010) explained in their work that the rotations and reorientation of CNTs within the host polymer can account for the increased network conductivity observed.

According to Sanli et al. (2017), physical aging effects and a lack of signal consistency may contribute to changes in electrical resistance over time. Furthermore, Pérez et al. (2016)

emphasizes that MWCNT slippage and disordering of the polymeric chains and MWCNTS network can result in a reduction in the number of conductive paths due to cyclic stress. These conclusions from previous studies account for the fluctuation and ensuing rise in electrical resistance.

It is worth emphasizing that when observing the mechanical plot for flexural strain over time, it is evident that the strain does not reach a null value during the resting state as expected by the literature Spinelli et al. (2020). Therefore, it is reasonable to assume that some of the residual electrical resistance for electrical measurements can be attributed to this residual strain, especially given the demonstrated correlation between deformation and piezoresistive response.

The samples were loaded and unloaded in cycles at a cell velocity of $5\ \mathrm{mm/min}$ and a maximum flexural strain of $0.809\ \%$ to evaluate electromechanical hysteresis. The results are compiled in Figure 4.7 for various load cycles. The 1^{st}, 10^{th}, 25^{th}, 50^{th}, 75^{th}, and 100^{th} cycles are represented, enabling an analysis of potential mechanical hysteresis under continuous loading and unloading.

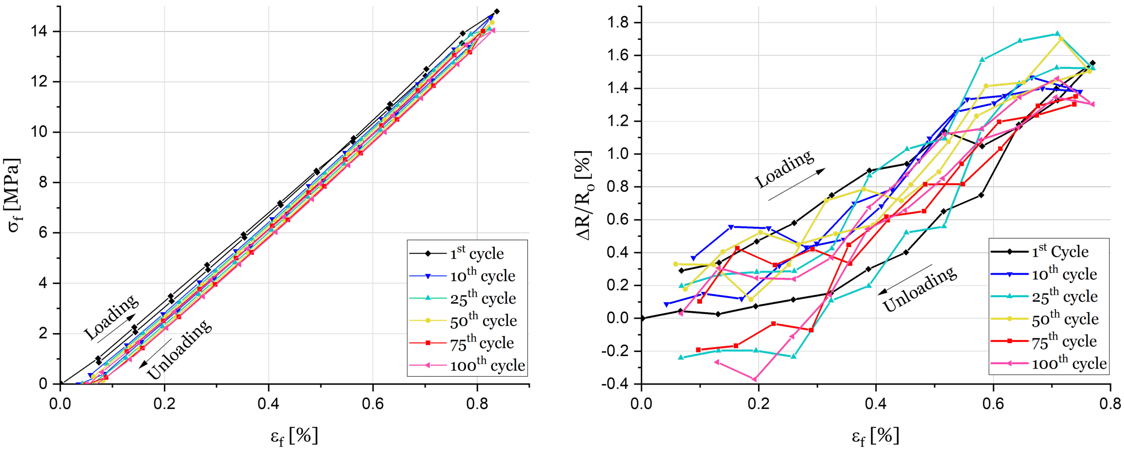

(a) (b)

Figure 4.7: (a) Average curves depicting mechanical and (b) electrical response for different cycles of loading and unloading to verify nanocomposite hysteresis.

The results indicate that mechanical hysteresis (Figure 4.7a) does not represent a significant issue for all plotted cycles. Figure 4.7b summarizes a different behavior between loading and unloading, for different cycles. 1^{st}, 25^{th} and 100^{th}, present a behavior similar to hysteresis, by identifying an area between loading and unloading. For the other cycles, the loading and unloading cases intersect. On the other hand, this does not seem to have a direct relation with the cycle number.

After studying how the loading cycles influence the electrical response, the following research goal was to investigate how cyclic loading and unloading affect the GF. The sensitivity was measured through the GF for the 1^{st}, 10^{th}, 25^{th}, 50^{th}, 75^{th}, and 100^{th} cycles during flexural stress. It is important to note that the GF is the ratio between $\Delta R/R_0$ and strain (ε), in this case, flexural strain. The test conditions included a loading cell velocity of $5\ \mathrm{mm/min}$ and a constant maximum flexural strain ($\varepsilon_f = 0.809$ %).

Figure 4.8 presents the results showing the GF as a function of the cycle for both loading and unloading conditions. The primary objective is to identify how the number of cycles and the loading and unloading phases influence the GF and if there is a relationship between parameters.

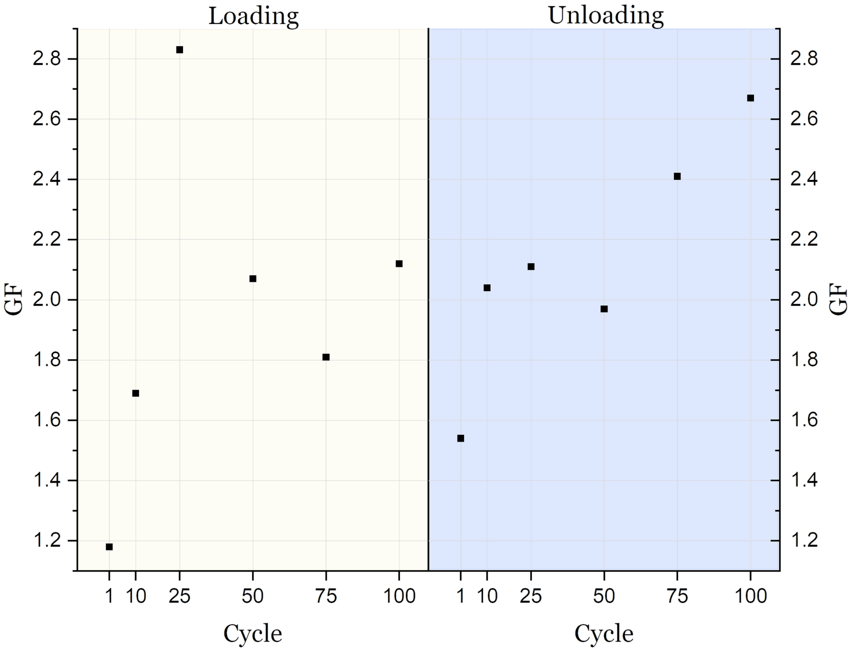

Figure 4.8: GF across various loading and unloading cycles at a consistent maximum flexural strain ($\varepsilon_f = 0.809$ %) for bulk adhesive samples.

Upon analyzing the plot, it is evident that the first cycle, both for loading and unloading, has the lowest sensitivity, with values of 1.18 for loading and 1.54 for unloading. However, as subsequent cycles are conducted, the GF increases for both loading and unloading conditions. The 25^{th} loading cycle reaches the highest GF value among the studied points. Nevertheless, this specific point does not suggest a consistent trend, as the variation between the 10^{th} cycle and the following 50^{th}, 75^{th}, and 100^{th} cycles is 22 %, 7 %, and 25 %, respectively. This observation presents that there is not a significant dispersion of data regarding piezoresistive sensitivity.

For the unloading condition, the behavior is similar, although there is a specific point with higher GF for the 100^{th} cycle. The dispersion is similar for the first point, which has a lower GF value, and the following three points present a more concentrated dispersion with GF values around 2. The last two points exhibit higher GF values (2.4 and 2.65, respectively). In this case, the variation in electrical resistance is higher than the flexural strain, resulting in a steeper slope for the electrical resistance data and, consequently, higher sensitivity.

In summary, for both loading and unloading conditions, the GF value is consistently around 2.0 for a flexural strain variation between 0 % and 0.809 %, suggesting good performance for the strain sensing adhesive. This value is comparable to what is commercially available for metallic strain gauges, which typically have values ranging from 2 to 5, as reported by Yang and Lu (2013). This observation suggests that the strain-sensing adhesive of epoxy resin reinforced with 0.50 wt.% CNTs is on par with or even exceeds the sensitivity of conventional metal strain gauges.

To delve deeper into the behavior of the reinforced nanocomposite adhesive system, the electrical response of these systems to constant flexural stress ($\varepsilon_f = 0$ % and $\varepsilon_f = 0.809$ %) was investigated. The purpose of this work was to determine whether an electrical signal is capable of identifying a structure that is permanently loaded or if it is limited to responding to instantaneous strain deformations.

The samples were subjected to cyclic loading and unloading phases for fixed time intervals ($\Delta t = 0$, 30, 120 s) to assess how the piezoresistive measurements monitor the mechanical loading/unloading phases. It is important to note that the mechanical and piezoresistive tests were conducted in separate experiments but are presented consecutively in Figure 4.9. The test conditions included a loading cell velocity of $5\ \mathrm{mm/min}$ and a constant maximum flexural strain ($\varepsilon_f = 0.809$ %).

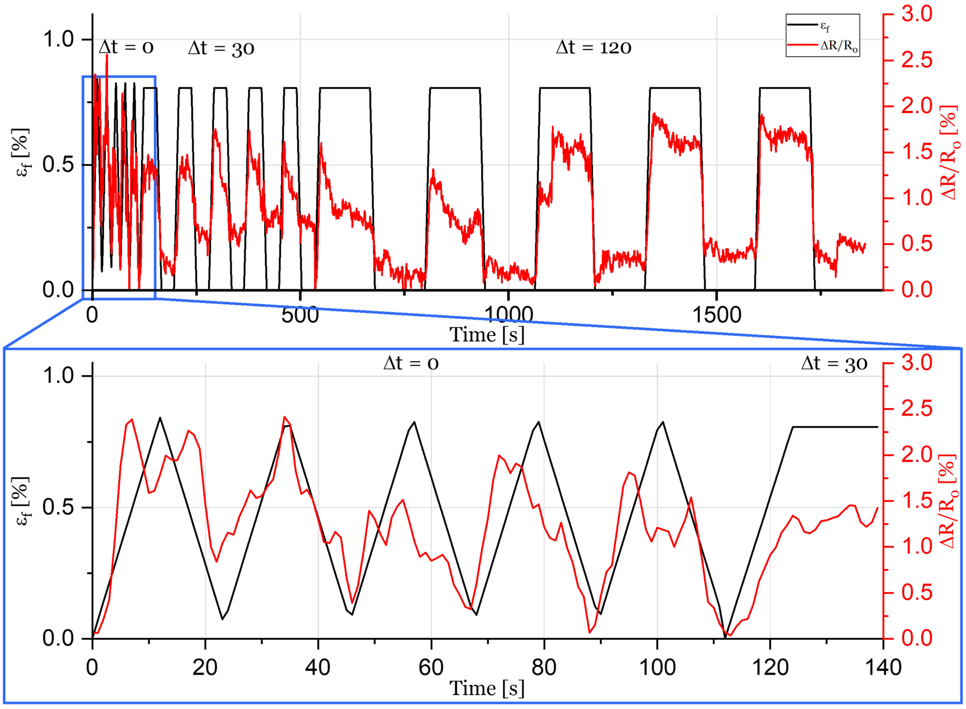

Figure 4.9: Representative curves of cyclic flexural stress under different loading and unloading time intervals, alongside corresponding electrical resistance monitoring data for bulk adhesive joints reinforced with 0.50 wt.% CNTs.

Figure 4.9 displays representative curves for electrical and mechanical behavior for different loading and unloading time intervals for bulk adhesive samples loaded with 0.50 wt.% CNTs. The nanocomposite samples exhibit corresponding behavior between flexural strain and electrical resistance measurement for all Δt plotted cases. For the examined cases, the figure illustrates a positive piezoresistive response during cyclic loading and unloading.

Considering $\Delta t = 0$ s, a strong correlation between electrical and mechanical data is observed. Additionally, during the resting state condition, where a residual flexural strain remains, there is a residual piezoresistive effect, measuring approximately 0.25 %. On the other hand, for the same velocity and flexural strain previously tested, the maximum normalized electrical resistance range values are around 2 %.

The electrical behavior still shows a correlation for $\Delta t = 30$ s. Nonetheless, during the continuous loading period, it is important to note a minor decrease in the normalized electrical resistance measurement. There is a comparable relationship between the mechanical strain and the first and second cycles. Nevertheless, the electrical resistance decreases throughout the final three cycles of the loading condition phase. Furthermore, in the unloading condition, there is a residual electrical resistance measuring 0.75 %.

In the final studied case, $\Delta t = 120$ s, the behavior is similar to that of $\Delta t = 30$ s, with a slight reduction in the constant loading condition, decreasing from approximately 1.75 % to 0.75 % for the normalized resistance between the constant phases of load. However, there is a stabilization in the final cycles, with the electrical resistance signal becoming constant during constant loading. The resting state shows a residual piezoresistive value close to 0.25 %.

For all instances where $\Delta t = 0$, 30, and 120 s, a piezoresistive peak of approximately 2.0 % under maximum load conditions is observed. Comparing these three cases, it is evident that the strain-sensing adhesive demonstrates a satisfactory sensing capacity. Specifically, for $\Delta t = 120$ s, a piezoresistive stabilization indicates that a longer loading time allows for adaptation and stabilization of the sensing adhesive. Conversely, for $\Delta t = 30$ s, a decline in piezoresistive behavior during constant loading, followed by a rapid decrease during unloading, is noticed. This result suggests that the sensing adhesive effectively monitors the load and unload slopes but requires time to adapt to the constant loading and unloading state. A slight decrease in normalized resistance, mainly during loading, is noted.

In situations where a constant load is not applied, the sensing adhesive exhibits a noisier response. However, as previously observed in this study, it performs effectively when monitoring minimum and maximum load conditions. In all scenarios, a quicker recovery and a more stable response are identified during the unloading constant stage. This outcome can be attributed to the rapid reorganization of the CNT network within the polymeric matrix during the unloading condition (Sanli et al. (2017)).

Similar to what was observed in Sanli et al. (2017), the destruction of nanotube-nanotube contacts can be neglected by working within a small range of strain values (≈ 0.809 %) within the elastic limit. Thus, the tunneling effect is predominant. These results demonstrate the promise of the sensing adhesive, even under constant loaded conditions. These results imply that the percolative network within the material does not present considerable changes for constant load conditions, and the predominance of the tunneling effect, even during loading, highlights its potential for practical sensing applications.

4.2 Enhanced SLJ utilizing multifunctional adhesive reinforced with 0.50 wt.% CNTs

4.2.1 Mechanical properties under flexural stress

This section investigates the mechanical and electromechanical performance of SLJs using an adhesive with improved capabilities. The main objective is to find an optimal balance between sensing capabilities and bending resistance, also testing the samples under various speeds and bending stresses within the elastic range to check the sensitivity regime.

The initial mechanical assessment involved a static bending test until failure, aiming to determine key mechanical parameters in flexure, including flexural modulus, peak load, and ultimate failure load. These parameters serve as a foundation for comparing the performance of pure epoxy and the reinforced adhesive.

Utilizing Equation 3.1, the recommended span length for SLJs is $64\ \mathrm{mm}$. However, for these experiments, two samples were prepared, one with pure epoxy and another with reinforced adhesive, and tested over a span length of $60\ \mathrm{mm}$. The summarized results are presented in Figure 4.10a, distinguished by dashed lines. The tests were carried out at a load cell velocity of $6\ \mathrm{mm/min}$ until failure. This velocity was chosen to accommodate the increased span length compared to previous tests on bulk adhesive samples. However, the influence of velocity on the tested joints is explored later in this study. The curves shown are representative of a span length of $60\mathrm{mm}$. To reduce the concentration of transverse stress in the bonding area and guarantee the adhesive rupture, the span was extended to $150\ \mathrm{mm}$ to assess the influence of span length on the mechanical properties of the adhesive joints. These results are also represented in Figure 4.10a.

As observed, the representative curves for each case exhibit steeper slopes, indicating a higher flexural modulus and greater material stiffness. For the dashed curves, red circles represent zones where the adherends separated due to peel stresses, as illustrated in Figure 4.10b. The red lines evidence the angle between both adherends due to peeling stresses. Peel failure results in irreversible damage. Therefore, for a span length of $60\ \mathrm{mm}$, the maximum load failure for the first detachment, a consequence of peel stresses, corresponds to the elastic load limit. However, this occurs at a bending strain of $0.202\ \%$, and $0.259\ \%$ for pure and reinforced adhesive, respectively. In both cases, ultimate failure occurs after the initial peeling event, which occurs at a flexural strain below $0.01\ \mathrm{mm/mm}$.

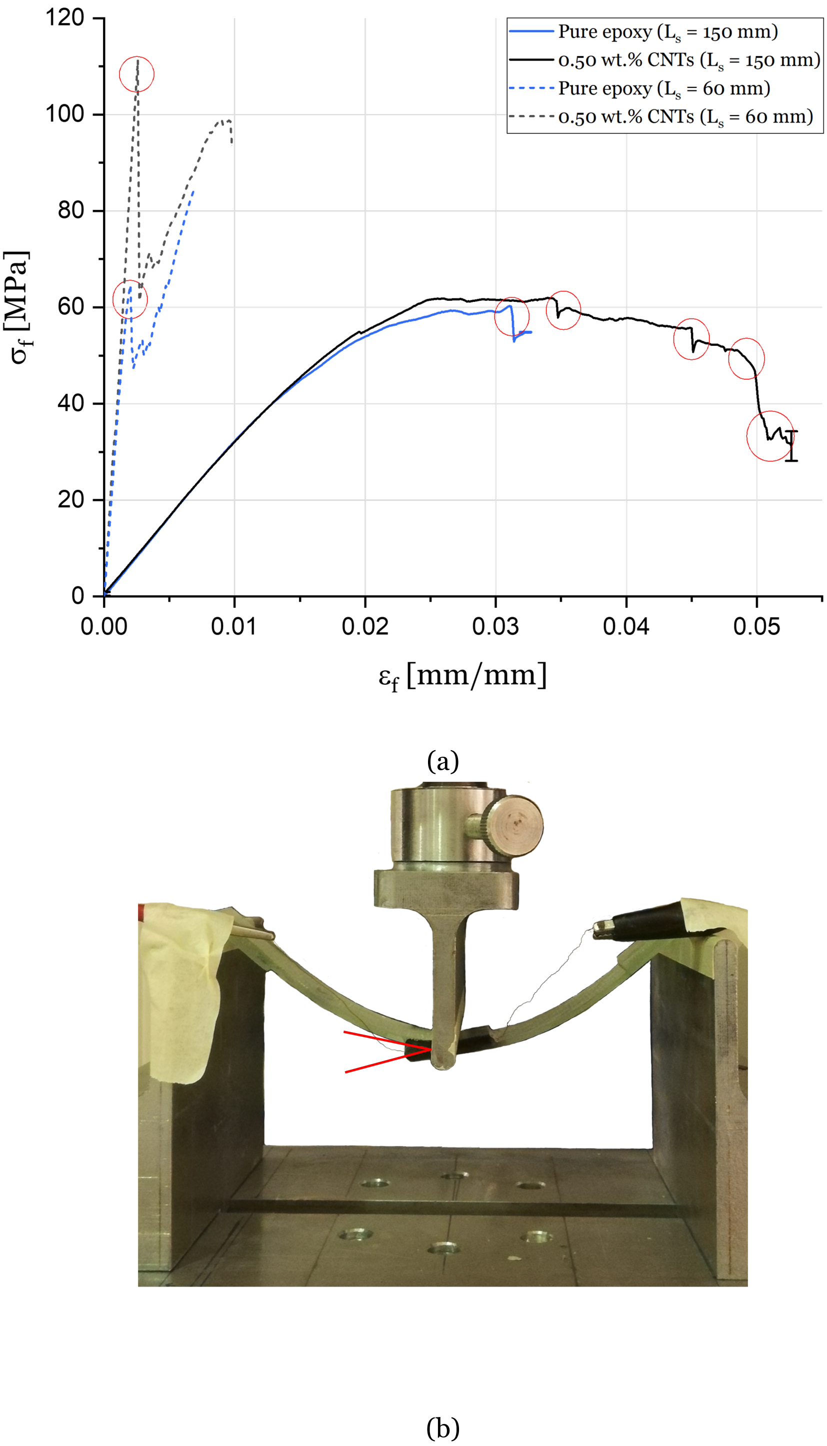

Figure 4.10: (a) Comparison of flexural stress-strain curves between SLJs with an adhesive reinforced with 0.50 wt.% CNTs: across different testing spans of 60 mm and 150 mm. (b) Representative image of peel failure in an adhesive joint during a flexural test until fracture ($Ls = 150$ mm).

A comprehensive investigation into the failure surfaces of the adhesive joints was performed. This analysis involved a visual examination of the fracture surfaces, depicted in Figure 4.11, similar to the methodologies applied in previous studies such as those by Lim et al. (2011); Daliri et al. (2020); Ejaz et al. (2022).

For the pure epoxy case (see Figure 4.11a), the fracture surface indicates a substrate or adherend failure, due to the visible fibers and a small area that experienced a cohesive failure mode (at the center).

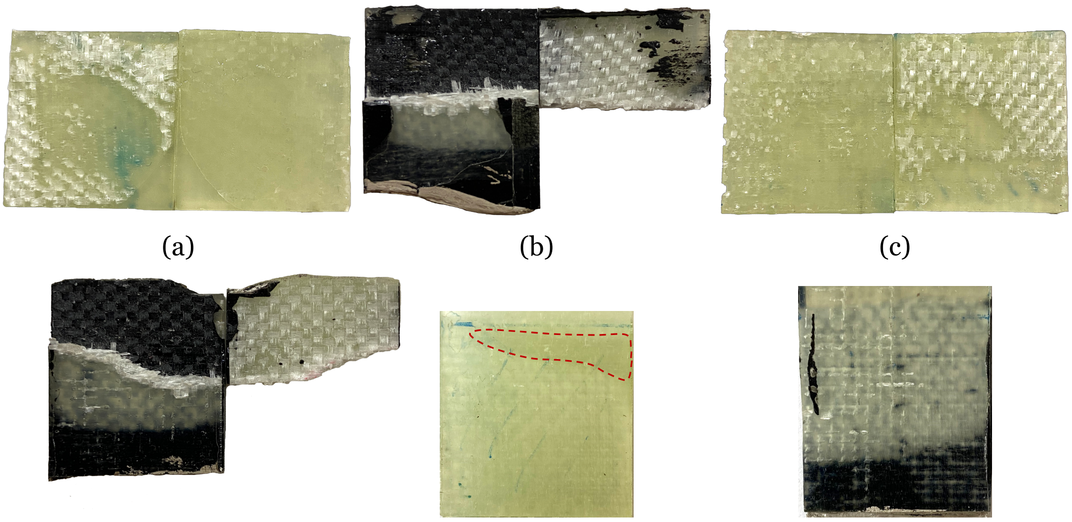
(a) (b) (c)

(d) (e) (f)

Figure 4.11: Characteristic fracture surfaces of the SLJ bending test specimens tested under identical conditions. (a) Pure epoxy sample ($L_s = 60$ mm). (b) Adhesive reinforced with 0.50 % CNTs sample ($L_s = 60$ mm). (c) Pure epoxy sample ($L_s = 150$ mm). (d) Adhesive reinforced with 0.50 % CNTs sample ($L_s = 150$ mm). (e) Pure epoxy sample ($L_s = 150$ mm) without complete detachment (the joined area is highlighted in red). (f) Adhesive reinforced with 0.50 % CNTs sample ($L_s = 150$ mm) without complete detachment.

For the reinforced adhesive (see Figure 4.11b), there is a combination of substrate or adherend failure and a small area of adhesive failure. The peeling forces detach half of the adhesion joint, with the final fracture taking place within the adherend system. A noticeable lighter area in the overlap joint corresponds to the debonded area without the total detachment of the joint.

This outcome is clarified by considering the mechanical strength of the adherend, which is comparatively lower than that of the adhesive. As a result, complete detachment does not occur, and the joint ultimately fails within the adherend component.

This observation is explained by the stress distribution over the overlap area. At the end of the overlap, the through-thickness stresses are high (Banea and da Silva (2009a)), and the adhesive fails first rather than the adherent. When the first detachments happen due to the peel stresses, the adherend fails with substrate failure within the overlap area, causing fiber delamination. The final failure happens in the adherend due to the increased transverse stresses leading to adherend failure. In summary, the reinforced adhesive showed a different failure mode, compared to the pure epoxy case, showing a much stiffer material, being the adherends the cause for SLJ rupture.

To reduce the concentration of transverse stress in the bonding area and promote adhesive rupture, the span was extended to $150\ \mathrm{mm}$ to assess the influence of span length on the mechanical properties of the adhesive joints. With reduced shear and compression forces in the application region, the adhesive is expected to experience rupture within the bonding area. Solid lines in Figure 4.10a represent pure epoxy and reinforced adhesives displaying the average results with error bars indicating the standard error calculated from the standard deviations for flexural stress at break. Red circles highlight stress/strain points where detachment occurred before the ultimate joint failure.

In pure epoxy, initial detachment occurs, leading to ultimate joint rupture at approximately $0.03\ \mathrm{mm/mm}$ of flexural strain with a failure load of $54\ \mathrm{MPa}$. For the reinforced adhesive, the mechanical curve shows four detachment events before the final joint failure. These events happen at a flexural strain of 0.035, 0.045, 0.050, and $0.051\ \mathrm{mm/mm}$. These events are marked by a sudden change in stress (red circles in Figure 4.10a). At a flexural strain of $0.052\ \mathrm{mm/mm}$, the SLJ failed under a load of $30\ \mathrm{MPa}$.

Comparing both adhesives, the reinforcement with CNTs results in increased plastic response and higher flexural strength. This outcome is consistent with enhanced toughness behavior, as reported in the work of Ejaz et al. (2022). However, it is essential to note that the elastic properties do not follow the same pattern observed in bulk adhesive joints, as the elastic limit increases for the reinforced adhesive. These findings emphasize the effects of CNT incorporation on material properties, which vary depending on the specific application and structural configuration.

However, the actual failure modes were different from what was anticipated. In Figure 4.11c, complete detachment occurred, and the fracture surface primarily showed substrate or adherend failure. There were also small areas displaying adhesive and cohesive failures within the overlap region, indicating a mixed failure mode. In the nanocomposite case (Figure 4.11d), the fracture surface resembled that of the $60\ \mathrm{mm}$ length span, with the principal failure mode being substrate or adherend failure, followed by a small area of adhesive failure (in overlap length). In the reinforced adhesive, the upper adherend experienced effective failure with a lighter area indicating detachment between adherends, driven by increasing transversal stresses causing adherent breakage.

Distinct failure modes are depicted in Figures 4.11e and 4.11f for pure and reinforced adhesives. Unlike cases where complete detachment occurred, these specimens exhibited regions of debonding but without reaching the final joint failure. This outcome enabled the joint to escape from the universal testing machine supports due to increased deformation and span length. However, data from these specimens were still considered up to this point, as the mechanical curve consistently displayed behavior across specimens.

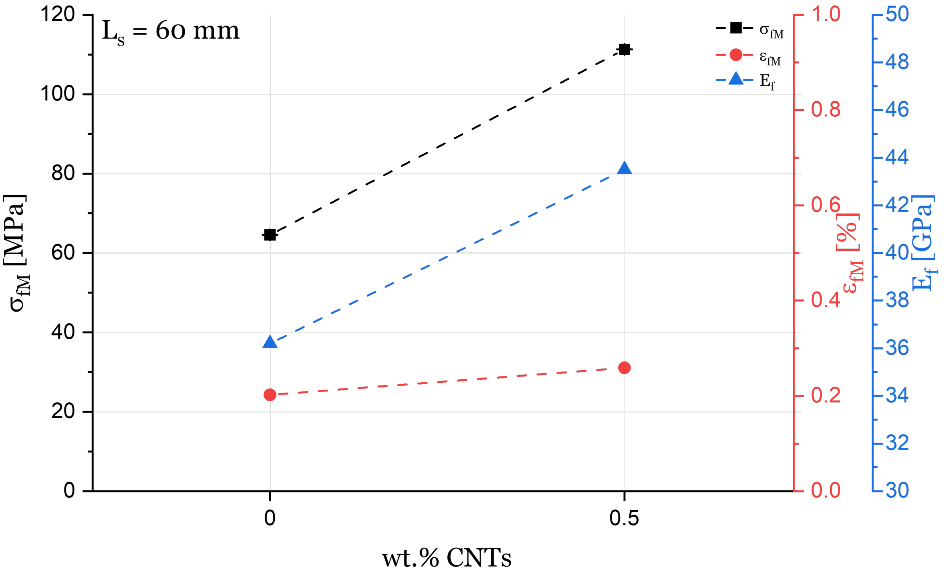

Figure 4.12: Flexural properties (strain at maximum stress (ε_{fM}), maximum stress (σ_{fM}), and flexural modulus (E_f)) of representative samples in SLJs, for pure and reinforced adhesives, tested at 60 mm span length.

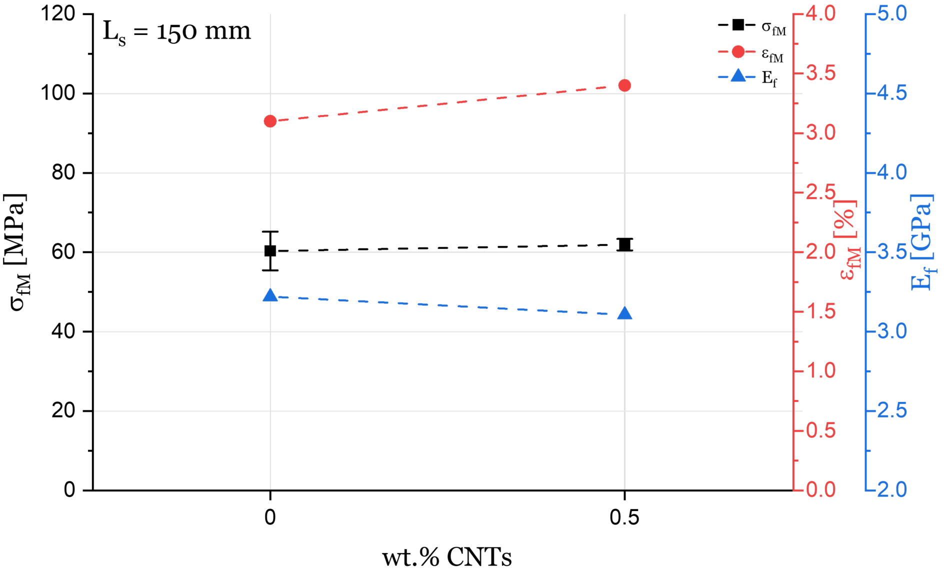

Figure 4.13: Flexural properties (strain at maximum stress (ε_{fM}), maximum stress (σ_{fM}), and flexural modulus (E_f)) of representative samples in SLJs, for pure and reinforced adhesives, tested at 150 mm span length.

The maximum flexural stress and corresponding strain were evaluated to explore the impact of span length on the mechanical characteristics of the adhesive joints, as depicted in Figures 4.12 and 4.13. Additionally, the flexural modulus for each case was examined. The error bars represent the standard error calculated from the standard deviations for the maximum flexural stress.

Analyzing each span individually reveals variations in mechanical properties between the pure epoxy and the nanocomposite material. For $L_s = 60$ mm (refer to Figure 4.12), pure epoxy exhibits a maximum flexural stress of 64.6 MPa at a flexural strain of 0.20 %. In contrast, the reinforced adhesive achieves maximum flexural stress of approximately 111.3 MPa, which is 72.3 % higher, at a flexural strain value of $e_f = 0.26$ %. The flexural modulus also follows this increasing trend, measuring 36.2 GPa for pure epoxy and 43.5 GPa for the nanocomposite. These enhanced properties align with previous findings for bulk adhesive samples reinforced with 0.50 wt.% CNTs, which experienced improvements in mechanical properties. The elastic limit coincides, in particular, with the point of maximum bending stress since the adhesive joint peels off once this threshold has been exceeded.

In the case of $L_s = 150$ mm, mechanical properties exhibit differences compared to the previous span length. The flexural modulus slightly decreased, with a reduction of approximately 3.5 % (from 3.22 GPa to 3.11 GPa). On the other hand, the maximum flexural stress increased from 60.3 MPa to 61.9 MPa, marking a 2.65 % increment. The flexural strain for maximum flexural stress shows an increase from 0.031 to 0.034, representing an increment of 9.7 %.

The most notable difference for the longer span under study is the elastic limit. In this scenario, there is a marked increase of approximately 10 % in stress and 16.7 % in strain compared to pure epoxy. This value indicates an enhancement in elongation, signifying that the adhesive joint can withstand higher stress and deformation without undergoing permanent damage and entering into plastic deformation.

Conversely, in the case of the reinforced adhesive with a span of 150 mm, there is an evident improvement in the plastic regime. This improvement contributes to enhanced adhesive toughness.

4.2.2 Electromechanical tests in flexural strength for reinforced SLJs

After thoroughly analyzing the mechanical responses, it is essential to assess whether the observed electrical characteristics in adhesive joints hold potential for multifunctional materials and, consequently, for structural health monitoring. Electrical resistance measurements are carried out during loading until the specimen breaks at span lengths of $L_s = 60$ mm and $L_s = 150$ mm.

The results are illustrated in Figure 4.14. This figure displays the relationship between flexural stress and normalized electrical resistance concerning flexural strain for a span of 60 mm. The aim is to observe both curves to identify potential correlations, paving the way for using these joints as multifunctional materials. The electromechanical tests were performed at a loading cell velocity of 6 mm/min. Dashed lines facilitate observations, outline significant changes in the mechanical curve, and establish a direct link with the electrical plot. Two linear approximations are provided for normalized electrical resistance within the elastic and plastic regimes.

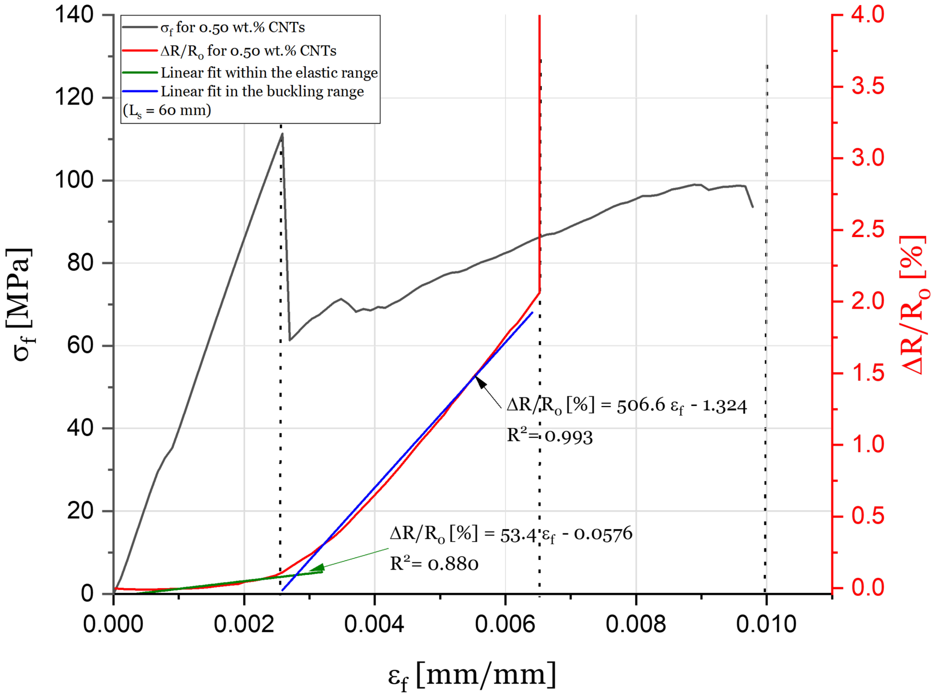

Figure 4.14: Representative curves illustrating the mechanical response and normalized change in electrical resistance relative to flexural stress as a function of flexural strain for SLJs with reinforced adhesive containing 0.50 wt.% CNTs, tested with a 60 mm span.

According to the figure, when reaching the elastic limit and at the point of initial detachment for the 0.50 wt.% CNTs joint, a perceptible alteration in the slope of the electrical resistance curve is noticed. In the first segment, which corresponds to the elastic range of the joint, the electrical resistance measurements show a more gradual curve. This behavior resembles what was observed in prior works by Vertuccio et al. (2016) and Bregar et al. (2020), characterized by an exponential increase. An attempt was made to calculate the GF for this elastic range, yielding a value of 0.53 (from a strain value between 0 and 0.26 %). However, the equation presents a lower coefficient of determination (R^2) due to a decrease of electrical resistance for lower values of flexural strain (from 0 to 5.62×10^{-4} mm/mm).

When comparing these results with adhesive bulk material for the elastic region, it is apparent that the GF is significantly lower, reduced by 90 %. In the plastic range, electrical resistance measurements align with a linear behavior, consistent with the findings of Yao et al. (2017) and in agreement with these work observations for bulk adhesive joint specimens. The determined GF was 5.07 for a strain range of 0.26 % to 0.65 %. This sensitivity value closely aligns with those obtained for bulk adhesive joints, increasing significantly from the elastic to plastic region.

A point emerges at approximately a flexural strain of $0.0065\ \mathrm{mm/mm}$ where the normalized electrical resistance experiences an infinite peak. Notably, this does not correspond to the final mechanical failure of the specimen, as evidenced by the mechanical curve. Instead, it arises from the detachment of copper wires from the silver-painted electrodes.

An important parameter to highlight is the achieved normalized electrical resistance. Up to the linear limit within the elastic range, the electrical resistance experiences a variation of 0.1 %. In contrast, for the plastic region, the electrical resistance undergoes a more significant variation, ranging from 0.1 % to 2.0 %. This change is noticeably smaller compared to bulk adhesive joints, where variations of up to 20 % were observed from the plastic limit to fracture.

Another notable observation relates to the curve behavior. In bulk adhesive joints, the curve shows a logarithmic pattern, while in SLJ flexural tests, the curve displays an exponential trend similar to that observed in Bregar et al. (2020)'s work for tensile loading. It is important to emphasize that, at this point, the behavior of the SLJ's internal electrical network during loading cannot be definitively understood. However, the presence of linear behavior is evident in both types of samples, particularly within the elastic and plastic ranges, albeit with distinct characteristics. This intriguing observation is left open for future in-depth exploration.

When examining the results for $L_s = 150\ \mathrm{mm}$ (refer to Figure 4.15), a clear correlation appears in the electromechanical curves. The flexural strength was determined at a loading cell velocity of $6\ \mathrm{mm/min}$, and representative curves are depicted. The linear range extends up to a flexural strain of approximately $0.02\ \mathrm{mm/mm}$.

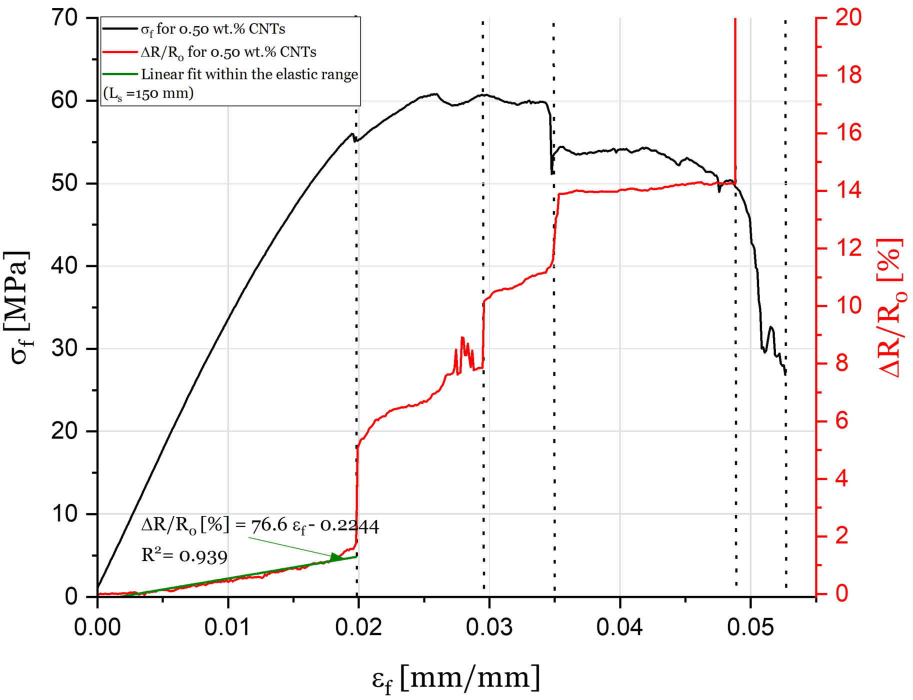

Figure 4.15: Representative curves illustrating the mechanical response and normalized change in electrical resistance relative to flexural stress as a function of flexural strain for SLJs with reinforced adhesive containing 0.50 wt.% CNTs, tested with a 150 mm span.

The electrical resistance plot shows a linear phase in the elastic region ($0\ \% < \varepsilon_f < 2\ \%$), from which a GF of 0.77 was obtained using a linear approximation. The sensitivity within the linear range is slightly lower compared to bulk adhesive joints but is similar to that calculated for the 60 mm span within the same range. At the elastic limit, the normalized electrical resistance measurement exhibits a variation on the order of 1.6 %.

Beyond the elastic limit ($\varepsilon_f = 0.020$ mm/mm at a flexural stress of $\sigma_f = 54.8$ MPa), a significant change in electrical resistance, up to 5 %, occurs. This variation corresponds to a notable alteration in the slope of the mechanical curve, likely attributable to a significant crack in the adhesive system, resulting in the debonding of the joint.

In the plastic regime, moments of flexural stress alteration are highlighted with dashed lines, depicting the relationship between flexural strain and normalized electrical resistance. Below a strain value of 0.03 mm/mm, there is a region with a noisy signal resulting from damage accumulation in the adhesion system. This higher stress level results in a substantial alteration in the electrical resistance plot, up to 10.2 %. It further increases to 11.5 %, followed by another abrupt change in the electrical resistance plot and the mechanical stress curve at a strain value of approximately 0.035 mm/mm. Beyond this point, the electrical resistance plot remains almost constant, at 14 %, eventually approaching infinity below a flexural strain of 0.05 mm/mm due to the disconnection of the copper wires from the electrodes.

Once the elastic limit is surpassed, alterations in the mechanical curve indicate cracks or significant separations in the adhesive system. However, minor variations correspond to the gradual accumulation of damage caused by microcracks. These findings closely align with the observations of Daliri et al. (2020).

This multifunctional adhesive effectively follows the mechanical trend, even indicating the corresponding flexural strain for detachment. However, the adhesive does not have the sensitivity to detect minor changes in the mechanical curve above a flexural strain of 0.035 mm/mm, maintaining an almost constant behavior. Additionally, the electrodes experience rupture, as evidenced by the absence of electrical resistance values beyond 0.049 mm/mm.

Similar to the previous case, the calculated GF is ten times lower than that determined for bulk adhesive joints. However, the linear behavior up to the elastic limit corresponds to lower values of normalized electrical resistance (1.6 %) compared to bulk adhesive joints (17 %). In this instance, GF is not calculated for the plastic regime due to varying levels of deformation and subsequent electrical resistance variations. Throughout the entire testing until failure, the adhesive consistently demonstrates a robust response in structural monitoring, effectively identifying cracks and detachment within the adhesion area.

Based on the previous observations, the upcoming study will employ a span length of 150 mm. This choice aims to explore higher strain and stress limits and delve into the electromechanical properties of the functionalized adhesives. The objective is to analyze their sensitivity and detection capabilities.

To better understand their performance, the multifunctional adhesives in a SLJ configuration were exposed to cyclic loading under different strain levels and incremental velocities, similar to the bulk adhesive joints case. These tests aimed to compare the results with those obtained in the initial phase of this study. These tests were conducted with a 150 mm span, as it allows for a broader range of flexural deformations resembling the conditions experienced by bulk adhesive joints. The loading velocity was set at 6 mm/min.

Figure 4.16 illustrates the data for strain and normalized electrical resistance as functions of time and maximum flexural strain. In this study, the black curve represents the flexural strain as a function of time, while the red curve denotes the normalized electrical resistance. It is important to note that these tests were not conducted simultaneously for various strain levels, but the results are presented in a single plot to facilitate data interpretation. The figures display representative curves derived from three consecutive cycles of each tested flexural strain value.

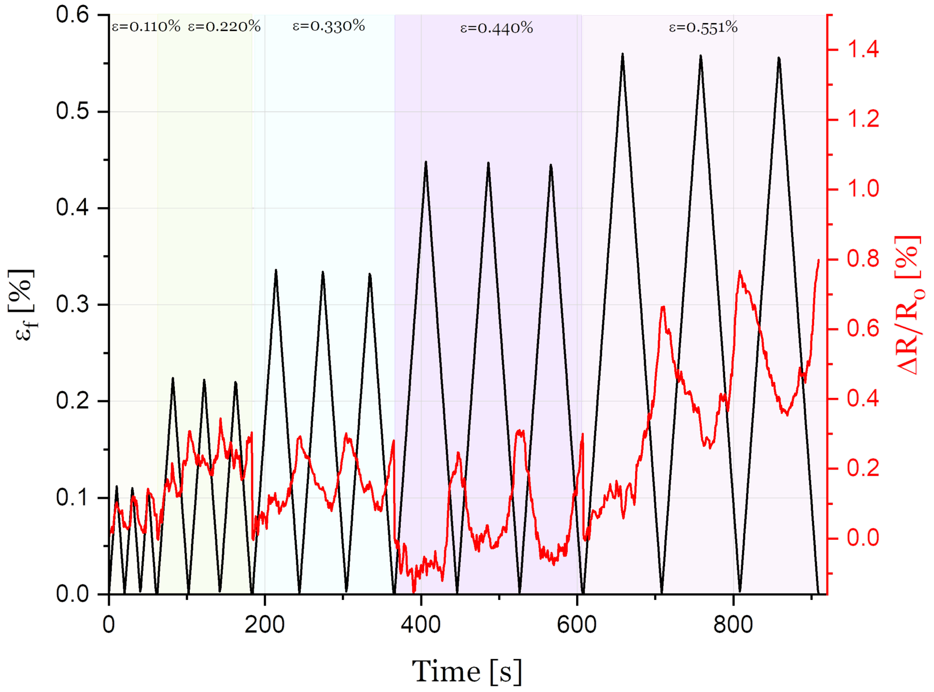

Figure 4.16: Representative curves of the normalized piezoresistive response during cyclic bending loading of SLJ specimens at various strain levels for 0.50 wt.% CNTs adhesive reinforcement.

Five different strain values were tested within the elastic limit for a span of 150 mm, corresponding to flexural stress levels from 5 % to approximately 30 % of the elastic limit for adhesive joints.

Two distinct piezoresistive behaviors are observed. At a flexural strain of $\varepsilon_f = 0.110$ %, the piezoresistive response is positive, indicating that the electrical particles separate during sample loading, leading to an increase in electrical resistance. However, for the subsequent tested flexural strains ($\varepsilon_f = 0.220\ \%, 0.330\ \%, 0.440\ \%, 0.551\ \%$), a negative piezoresistivity is observed. This occurs as the transversal network undergoes reconstruction due to tensile forces generated by Poisson's effect, thereby increasing electrical conduction in the joint when subjected to flexural stresses. This behavior suggests that tunneling increases as the specimens are loaded. Similar results were found in studies by Pérez et al. (2016) and Doshi et al. (2020), justifying the negative piezoresistivity as a consequence of shrinkage in the transverse directions due to the Poisson's effect. This effect creates a competition between the breakdown and reconstruction of the percolative network in the longitudinal and transversal directions, respectively.

As indicated in the studies by Hu et al. (2008), Bregar et al. (2020), and Spinelli et al. (2020), tunneling is particularly sensitive to changes in the filler's distance, occurring on the order of a few angstroms. Within the range of the elastic limit, as observed in Figure

4.16, tunneling is affected more significantly in the transverse direction of the load rather than in the longitudinal direction. This phenomenon is similar to compression, having a more pronounced effect than tension in the overlap area, primarily due to Poisson's effect.

When evaluating each flexural strain value individually in the plot, it becomes evident that the multifunctional adhesive accurately reflects mechanical changes in its behavior. For the first case, with a flexural strain of 0.110 %, piezoresistivity is positive, signifying that tensile forces dominate over compressive forces for small strain values, with the CNT particles moving apart with load. However, within this range, the results show a clear response with minimal noise in the electrical resistance data. The normalized electrical resistance reaches a maximum value of 0.1 % and approaches 0 % for the resting state condition.

For subsequent strains within this range, the piezoresistivity remains negative. The results exhibit a noisier response, but there is a noticeable delay in achieving minimum electrical resistance values, as this point does not align directly with the maximum flexural strain. With an increase in maximum flexural strain ($\varepsilon_f = 0.220$ %), the normalized electrical resistance also increases, ranging from 0.12 % at maximum strain to 0.31 % at minimum strain values.

In the following case, with a flexural strain of $\varepsilon_f = 0.330$ %, the electrical response exhibits a wider range, with a minimum of 0.079 % and a maximum of 0.29 % for normalized electrical resistance. These results are notably smoother without the noise observed in the previous case. Although there is a slight delay, meaning that the maximum strain value does not directly correspond to the minimum in normalized electrical resistance, the trend is evident, making these results highly promising. In the cyclic tests at $\varepsilon_f = 0.440$ %, a more pronounced variation between the maximum and minimum values of normalized electrical resistance is observed. This range extends from -0.063 % at maximum strain to 0.29 % at minimum strain values. Unlike the previous tests, a stabilization instead of a clear peak for loading conditions is observed. Thus, the adhesive is sensitive to variations between the resting state and the load condition, highlighting the point of change, but most of the time, the load condition signifies stabilization rather than a peak.

In the last studied case, $\varepsilon_f = 0.551$ %, the negative piezoresistivity response follows a similar pattern to the previously observed. However, the results do not exhibit the same range of variation between consecutive cycles, showing an increase in both maximum and minimum values of normalized electrical resistance.

These observations suggest that the sensing adhesive does not fully recover between consecutive cycles. The electrical network does not have sufficient time to adapt, leading to an accumulation of electrical connections due to tunneling persisting between cycles within the time considered between flexural strain peaks. This behavior was not observed for lower values of flexural strain, indicating that it results from higher deformation and a reduced capacity to restore the electrical network. Similar results are described by Pérez et al. (2016), suggesting that the CNT network (and the polymer chains) reorganize during the first charge-discharge cycle due to the applied stress and the release of residual stresses. Thus, due to deformation-induced changes in the microstructure of the composite, MWCNT reorganization occurs not only along the loading direction but also along the transverse one. For the last deformation value and after the first charge-discharge cycle, the competitive behavior between the destruction and reformation of the conductive networks has not yet stabilized due to the higher deformation.

Compared to bulk adhesive joints with similar strain ranges ($\varepsilon_f = 0.405$ %), the strain ranges obtained for the strain sensing adhesives in SLJs range from 0 % to approximately 2.00 %. These values are ten times greater than those observed for adhesive joints, as shown in Figure 4.16. However, despite these observations, it is evident that the multifunctional adhesive effectively detects strain deformation in various ranges, offering a promising solution for structural monitoring.

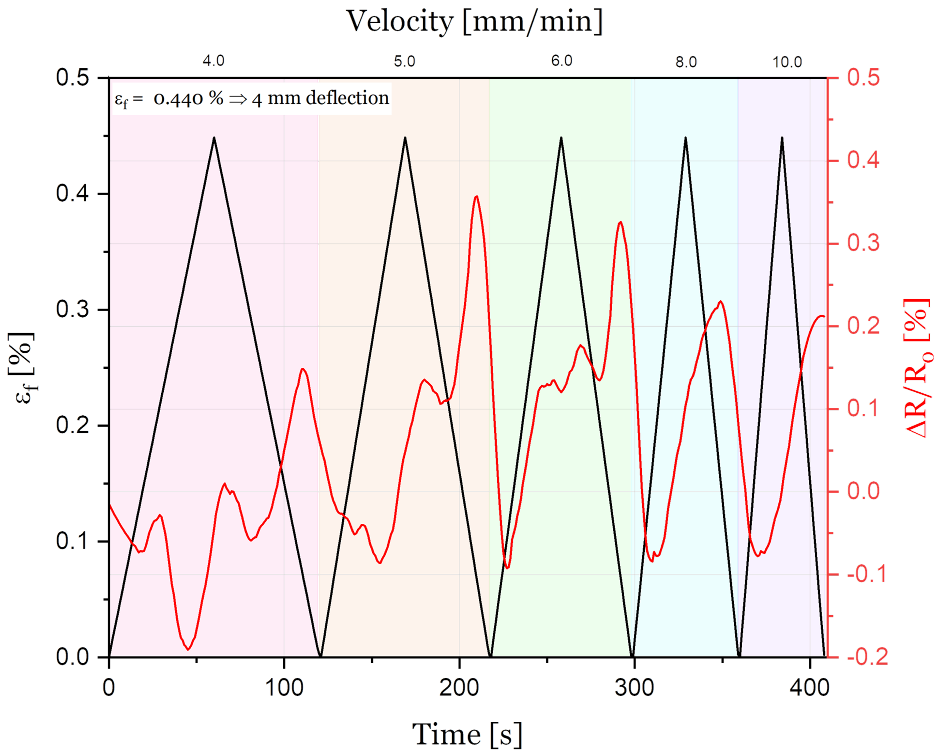

Figure 4.17: Representative curves depicting piezoresistive measurements at a fixed flexural strain ($\varepsilon_f = 0.440$ %) and variable loading cell velocity in a three-point bending test for SLJ specimens for 0.50 wt.% CNTs adhesive reinforcement.

For the subsequent tests, a maximum flexural strain of $\varepsilon_f = 0.440$ % was selected, as it provides a stable signal with a broader range of values between maximum and minimum electrical resistance measurement. The influence of loading cell velocity on sample sensitivity was examined and it was compared to the results obtained for bulk adhesive joints, evaluating the independence of results from the test velocity. Figure 4.17 illustrates these findings. It is important to note that these tests were not conducted simultaneously for various strain levels, but the results are presented in a single plot to facilitate data interpretation. The figures display representative curves derived from three consecutive cycles of each tested flexural strain value.

In this case, the data underwent signal processing using a Savitzky-Golay filter to clean the signal by removing noise without losing relevant information about the plot shape. The tested velocities were 4.0, 5.0, 6.0, 8.0, and $10.0\ \mathrm{mm/min}$. Similar to the approach taken for bulk adhesive joints, higher velocities were not tested to avoid potential data loss due to the one-second measurement interval.

Across all tested velocities, the electrical response consistently shows a negative trend. This result indicates that, under loading conditions, the nanocomposite experiences an increase in electrical conduction due to the closer proximity of filler particles within the epoxy matrix. The maximum recorded value for normalized resistance tends to be closer to the unloaded condition, typically around 0.2 %. However, at a cell velocity of $5.0\ \mathrm{mm/min}$, it reaches 0.35 %, and at $6.0\ \mathrm{mm/min}$, it exceeds 0.3 % for normalized electrical resistance.

As expected, higher velocities ($8.0\ \mathrm{mm/min}$ and $10.0\ \mathrm{mm/min}$) result in smoother curves due to fewer data points (one point per second). On the other hand, lower velocities, such as $4.0\ \mathrm{mm/min}$ and $5.0\ \mathrm{mm/min}$, exhibit more signal perturbations compared to the higher velocities. A velocity of $6.0\ \mathrm{mm/min}$ strikes a balance between data acquisition and signal disturbances. Notably, in all cases, a small delay exists between the maximum registered strain and the electrical signal. Similar to the observations of Pérez et al. (2016), the nanocomposite adhesive exhibited both positive and negative piezoresistive effects during the loading-unloading cycles. This behavior was attributed to a piezoresistive mechanism based on the bi-dimensional motion of the MWCNT network driven by the potential Poison's ratio, as well as competition between breakdown and reconstruction of the percolated network in both directions.

In comparison to bulk adhesive joints, which recorded an average value of approximately 1.0 % for maximum load conditions, SLJs display an average value of 0.25 % for normalized electrical resistance. SLJs demonstrate a lower variation in electrical resistance compared to bulk adhesive joint samples. The minimum electrical measurement remains relatively constant, approaching -0.08 %, which indicates consistency in the results of this study for velocities above $5\ \mathrm{mm/min}$. Considering the analyzed data, the upcoming electromechanical tests will be conducted at a loading cell velocity of $6\ \mathrm{mm/min}$.

Figure 4.18 depicts the piezoresistive behavior of SLJs when subjected to flexural stress below the elastic limit for 100 cycles. As mentioned previously, the goal is to evaluate the electrical response of the adhesive in SLJs under cyclic loading, with a finite flexural strain range, and to assess the stability of the electrical signal during these cyclic loading and unloading conditions. The curves represent a strain range of $0 < \varepsilon_f < 0.440$ % and the normalized electrical resistance measurements over time for a span length of $150\ \mathrm{mm}$.

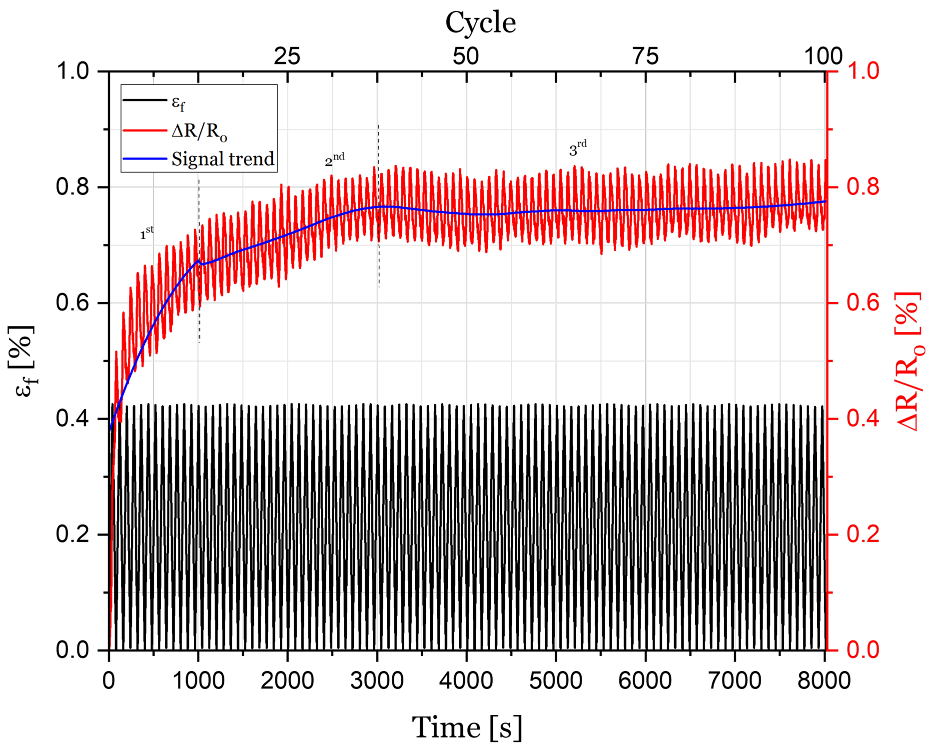

Figure 4.18: Representative curves describing the long-term stability of SLJ samples with adhesive reinforced with 0.50 wt.% CNTs for 100 cycles (8015 seconds) in flexural tests.

The signal trend is in blue, and the electrical resistance plot is divided into three main segments, which will be analyzed in more detail based on the variations in the signal trend, each identified by dashed lines and corresponding numbers for reference. The changes in electrical resistance reported below correspond to variations within the time segment referred to:

1. Cycles 1-13 (0 to 1018 seconds): This segment shows an abrupt change in the plot's trend, with a steep slope. However, there is a residual electrical resistance (0.6 % for the 13^{th} cycle), and the overall amplitude between cycles remains relatively constant.

2. Cycles 13-38 (1018 to 3020 seconds): For this sector, the slope exhibits a smaller increment. The amplitude between the maximum and minimum values for electrical resistance is reduced. For the 13^{th} cycle, the amplitude between the maximum and minimum is measured at 0.14, and for the 38^{th} cycle, it is 0.12 between the percentage change in resistance.

3. Cycles 38-100 (3020 to 8015 seconds): The signal trend stabilizes during the third part. The average value is approximately 0.77 % of normalized resistance. The residual electrical resistance tends to vary from cycle to cycle, being lower for the cycles with higher numbers (above the 50^{th} cycle) and higher after the 93^{rd} cycle, up to the 100^{th} cycle.

The SLJ adhesive required particle adaptation within the matrix, with no consistent behavior observed before the 38^{th} cycle. Signal stability was achieved afterward. Similar behavior was noted for all SLJ-tested samples in this work, suggesting a range of adaptations for a finite number of cycles. Operating below the elastic limit implies a lack of cracks or detachments in the joint, though a physical aging effect, as mentioned by Sanli et al. (2017), might occur. Concurrently, Pérez et al. (2016) reported that, after the initial loading-unloading cycle, competitive behavior between the destruction and reformation of conductive networks tends to stabilize with an increased number of cycles. This stabilization may lead to an increase in residual electrical resistance linked to the electrical resistance measurement before the test. Consequently, due to conformation and electrical network adaptation, the value of R_0 could increase.

In this study, it is crucial to note that changes in electrical resistance are smaller than those in bulk adhesive joints despite testing different strain values (0.809 % for bulk adhesive joints and 0.440 % for SLJ joints). The results of this study align with Mactabi et al. (2013), who found in fatigue tests on SLJs that the electrical resistance response remains relatively stable for a significant portion of the fatigue life, showing minor fluctuations in electrical resistance (less than 10 %) until approaching final failure. This region, often termed the ”safe zone”, exhibits minimal variations. In the case of this work, the normalized electrical resistance only minimally varied by 0.8 % during flexural testing. This value, well below the 10 % threshold observed in shear testing, suggests a predictable pattern in the increase of electrical resistance in flexural tests, ensuring the structural reliability of the joints.

After thoroughly investigating the electromechanical properties through a cyclic loading/unloading regime, a study of electromechanical hysteresis was performed. The previous examination revealed an increased electrical resistance ratio, which could be attributed to either mechanical hysteresis, causing variations in the electrical network due to different evolutions within the adhesive system, or electrical hysteresis, even in the absence of mechanical hysteresis. The results for mechanical and electrical hysteresis are presented in Figure 4.19, for a loading cell velocity of 6 mm/min, a maximum strain of 0.440 %, and a span of 150 mm.

Figure 4.19a summarizes the mechanical cycles, indicating no significant hysteresis. Regarding electrical hysteresis (see Figure 4.19b), only the first cycle displays a completely hysterical result. However, in subsequent cycles, the initial point aligns with the final point. Between cycles the plots do not coincide, leading to an increase in electrical resistance with the cycle number increment. As the cycle number increases, the energy loss diminishes, as evidenced by the decreasing area between the loading and unloading range.

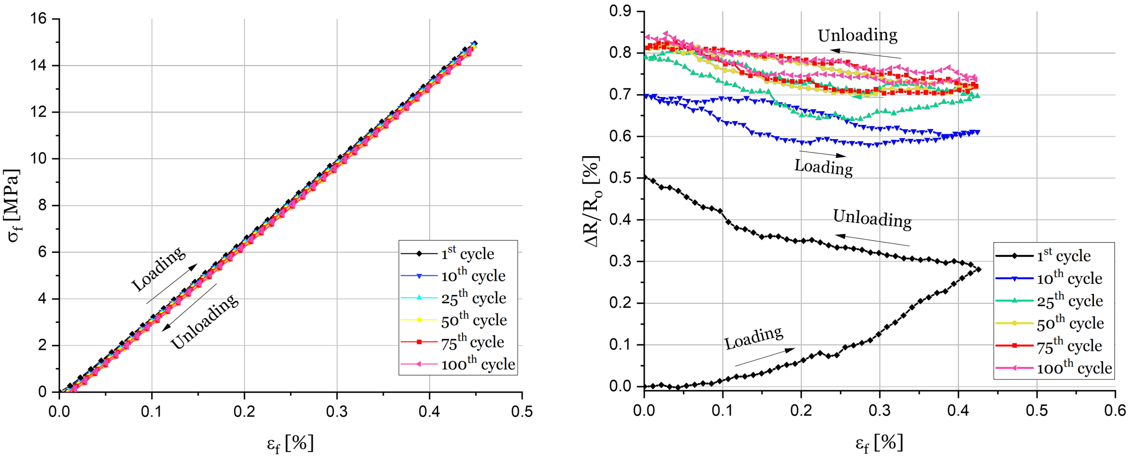

(a) (b)

Figure 4.19: (a) Curves depicting mechanical and (b) electrical response for different cycles of loading and unloading to verify nanocomposite hysteresis.

The GF was assessed regarding the number of load cycles to assess the adhesive's sensitivity degradation with time. The results are summarized in Figure 4.20, which shows how the GF varies with loading and unloading cycles. The primary goal was to comprehend how cycle count and loading/unloading phases affected GF.

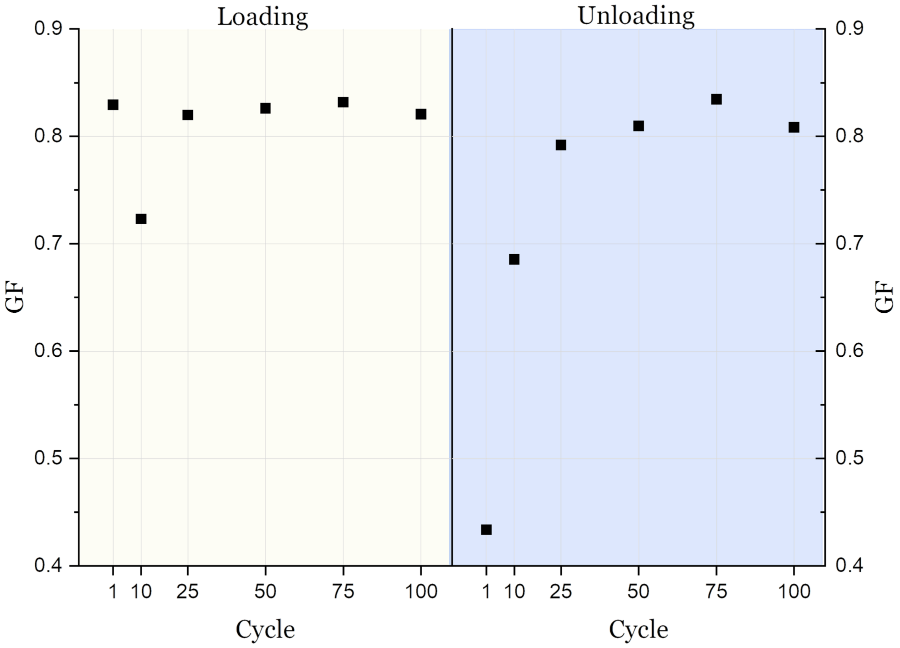

Figure 4.20: GF for different representative loading and unloading cycles at a constant maximum flexural strain ($\varepsilon_f = 0.440$ %) for SLJ samples.

The results obtained from tests conducted with a $150\ \mathrm{mm}$ span, constant maximum flexural strain of $\varepsilon_f = 0.440$ % and a loading cell velocity of $6\ \mathrm{mm/min}$ reveal consistent data with minimal dispersion. In the case of SLJs, there is minimal data dispersion except for three points. GF is consistently above 0.8, except for the 10^{th} cycle, for loading conditions. In the unloading condition, the initial two cycles (1^{st} and 10^{th}) exhibit lower values of 0.43 and 0.69, respectively. Subsequently, the remaining cycles stabilize around 0.8, mirroring the pattern observed for loading conditions. In comparison, bulk adhesive joints displayed higher GF dispersion, with an average value below 2.

The consistent and stable results are promising for the multifunctional adhesive. It reinforces the prior observations presented in the plot, indicating minimal amplitude variations between cycles and maintaining a constant GF. These findings remain consistent regardless of the variations observed in electrical resistance values between cycles. The results exhibit similar linearity and slope about strain.

As bulk adhesive joints exhibited the ability to withstand loading and unloading states, similar tests were performed for SLJs at a constant maximum flexural stress ($\varepsilon_f = 0.440$ %) and a loading cell velocity of $6\ \mathrm{mm/min}$. The samples underwent cyclic loading and unloading for fixed time intervals ($\Delta t = 0$, 30, and 120 seconds) to assess the piezoresistive response during these phases. It is important to note that although the mechanical and piezoresistive tests for each time interval were conducted separately, the results are presented consecutively in Figure 4.21.

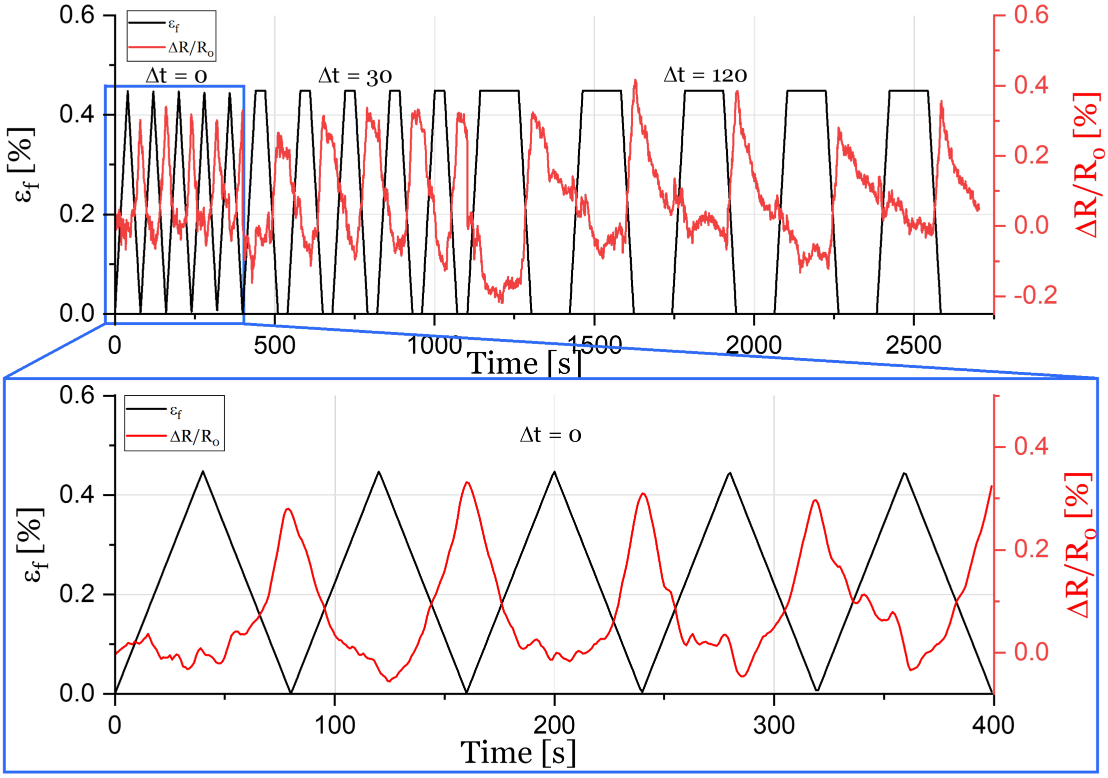

Figure 4.21: Cyclic flexural stress curves under various loading and unloading time intervals, accompanied by corresponding electrical resistance monitoring data for SLJs with adhesive reinforced with 0.50 wt.% CNTs.

The representative curves for $\Delta t = 0$ seconds revealed the previously reported negative piezoresistive behavior. Signal processing with a Savitzky-Golay filter was applied to extract the trend while preserving essential information. The signal is stable, with the maximum mechanical points corresponding to the minimums in the electrical curve. This pattern resulted in no variation in the electrical resistance for five consecutive cycles, presenting a value of approximately 0.3 % for resting state conditions. These results demonstrated a consistent behavior. However, the piezoresistivity did not mimic the mechanical curve exactly. When the mechanical plot reached its maximum strain, the piezoresistivity started to stabilize around 0 % rather than exhibiting a peak as seen in the mechanical curve.

For $\Delta t = 30$ seconds, the electrical resistance plot displayed a stable signal at fixed strains (0 % and 0.440 %). In the resting state, the piezoresistivity maintained a value of approximately 0.3 %, similar to what was observed for $\Delta t = 0$ seconds, and for the loading state, the value approached -0.1 %. In the loading and unloading conditions, the piezoresistive response is parallel to the mechanical curve and exhibits a consistent behavior over time.

Lastly, for $\Delta t = 120$ seconds, the normalized resistance showed a different trend. During loading, the normalized electrical resistance decreased, as expected, and subsequently remained approximately constant during the loading interval. In the unloading and resting state, the electrical resistance is permanently decreasing, deviating from the previously constant value near 0.3 %. This behavior persisted over the five cycles in the same conditions.

4.2.3 Mechanical properties under shear stress for SLJs with reinforced adhesive

The adhesive joints will undergo tensile stress testing to assess their shear strength characteristics. This test aims to determine whether the reinforced adhesive exhibits increased shear strength under tensile stresses.

The shear stress-strain plot in Figure 4.22 displays the average curves for adhesives, comparing pure epoxy with 0.50 wt.% CNT-reinforced adhesives applied in the SLJ configuration. The tensile strain was determined using loading cell displacement data, and shear stress in the adhesion area was calculated by dividing the applied tensile force by the overlapping area of the SLJ specimens. This calculation follows the methodology outlined in the works of da Silva et al. (2009) and Romate et al. (2018), as detailed in Chapter 3. The plotted curves depict the average value of three tested samples for each filler loading, with error bars indicating the standard error calculated from the standard deviations for lap-shear strength.

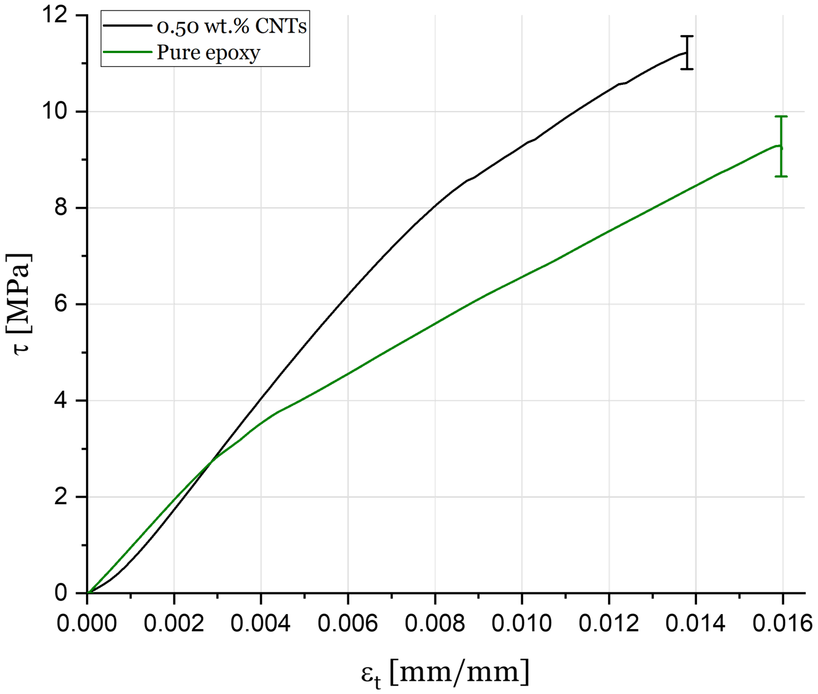

Figure 4.22: Average shear stress-strain curves up to failure for SLJs with adhesives reinforced with 0.50 wt.% CNTs and for pure epoxy samples.

The lap shear strength significantly improves from 9.27 MPa to 11.2 MPa with the addition of CNTs, representing an approximate 20.1 % enhancement. This result aligns with studies such as Shokrian et al. (2019), indicating that well-dispersed CNTs contribute to increased shear strength by activating an effective crack growth dissipation mechanism. Similar observations were made in studies like Razavi et al. (2018) and Ayatollahi et al. (2016), reporting enhancements of 15.4 % and 15.42 %, respectively, in 0.50 wt.% CNT-reinforced epoxy adhesives on aluminum adherends, contributing to the overall toughness of single-lap joints.

In contrast, the tensile strain at break, relative to pure epoxy samples, decreases by about 13.6 %. However, the linear behavior of the curve is more pronounced for the nanocomposite adhesive than for pure epoxy. The elastic limit for the nanocomposite reaches a shear strength of 9.64 MPa and a tensile strain of 0.011 mm/mm. For pure epoxy adhesive, this value is considerably lower, with the elastic limit reaching a stress of 5.43 MPa and a tensile strain of 0.008 mm/mm. This result indicates that the nanocomposite adhesive can withstand higher shear stress without permanent deformation compared to pure epoxy adhesive samples, and experiences an increase in the elastic range.

The increase in elastic modulus and lap shear strength is related to the addition of CNTs, based on the conclusions of Ejaz et al. (2022). The addition of CNTs increases the elastic response and the lap shear strength, being higher for reinforced adhesive specimens compared to pure epoxy SLJs. However, the tensile strain decreases for reinforced adhesive at break.

According to Jojibabu et al. (2016), the high tensile strength and modulus characteristic of CNTs significantly enhance the shear strength of adhesive joints. In this work, with a lower fraction of fillers, the dispersion enables robust interfacial bonding between the matrix and the reinforcements, ensuring efficient load distribution between them.

However, the decrease in elongation did not align with expectations. This result is attributed to the observed failure mode in these adhesive joints. To understand the fracture of the adhesive joints, the adhesion surfaces of three samples were visually inspected for each type of adhesive—pure epoxy and nanocomposite adhesive reinforced with 0.50 wt.% CNTs. This inspection followed the methodology outlined in Lim et al. (2011) and Daliri et al. (2020). Figure 4.23 summarizes these cases, where (a), (b), and (c) depict pure epoxy samples, and (d), (e), and (f) represent nanocomposite adhesives.

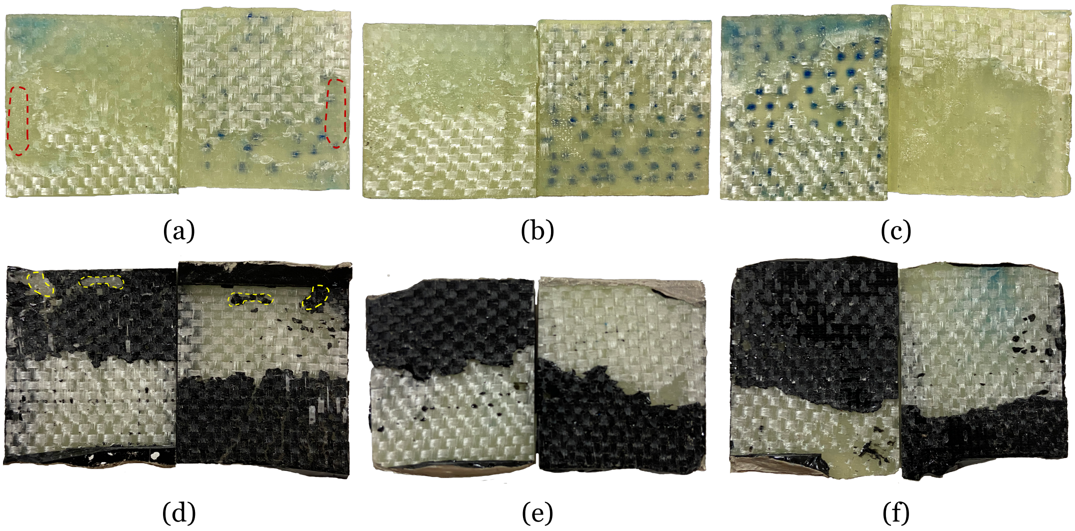
(a) (b) (c)

(d) (e) (f)

Figure 4.23: Analysis of adhesion surfaces for the study of typical failure modes in SLJ tensile test specimens under uniform conditions. Cases (a), (b), and (c) refer to SLJs with pure epoxy adhesive, while cases (d), (e), and (f) represent SLJs with nanocomposite adhesive. The colored dashed lines highlight specific regions discussed in the text.

In each image both sides of the adhesive joint are displayed, offering a comprehensive view of both adhering surfaces. In all cases, clear signs of substrate or adherend failure are evident on both sides of the joint. Similar results were obtained by Ahmed et al. (2018) with interfacial failure, where fibers were pulled out from the adherend. In this work, adherend failure is indicated by the lighter areas on both sides, corresponding to the exposed glass fibers.

In cases involving pure epoxy (Figures 4.23a and 4.23c), the tear distribution on each side of the joint is approximately 75 % and 25 %. In case (Figure 4.23b), adherend failure reaches 50 % on both sides. In case 4.23a, a small area experiences cohesive failure highlighted with a red dashed line on both sides. This specific area is in the center of the adhesive joint and bears less stress during tensile loading, primarily due to the load distribution characteristics in SLJs, as documented in studies by Banea and da Silva (2009a) and Romate et al. (2018). Thus, the adhesive failed and not the adherent, as reported in the other areas of the overlap area.

The fracture pattern for reinforced adhesive specimens is similar to that of pure epoxy, with substrate failure observed on both adhesion surfaces. In samples of Figures 4.23d and 4.23e, adherend breakage accounts for approximately 50 % on each side. However, in the specimen represented in Figure 4.23f, the ratio is about 75 % and 25 % for each adhesion surface breakage. In SLJ of Figure 4.23d, there is a mixed failure mode with a small adhesive failure highlighted with a yellow dashed line. These results are consistent with the stress distribution in the adhesion area during tensile stress testing. As reported in the literature, Shokrian et al. (2019) observed stress transfer within the overlap area during shear testing, resulting in distinct areas of failure in the adhesion zone.

These findings indicate that the adhesive exhibits excellent performance, with the primary points of failure occurring within the adherends under tensile loads. In all tested cases, the primary failures are within the adherends, involving both the epoxy and the glass fiber composite used as the adherends. These observations deviate from typical adhesive failure mechanisms documented in the literature, mainly for aluminum adherends.

For instance, Razavi et al. (2018) found that pure epoxy samples predominantly exhibited adhesive failure, particularly on aluminum adherends, and this trend continued even for reinforced samples with CNTs. On the other hand, Konstantakopoulou and Kotsikos (2016) reported a similar behavior for reinforced adhesives that experience an adhesive failure but experience a cohesive failure mode for pure epoxy samples.

Collectively, the reviewed studies reveal a consistent trend of cohesive failure in adhesive joints, both for pure and reinforced adhesives, emphasizing the crucial role of adhesion and force distribution within the adhesive layer in determining the failure mode (Jakubinek et al.; Jojibabu et al.; Romate et al.; Shokrian et al.; Ejaz et al.). In some instances, this adhesion was so effective that the adherend failed before the adhesive, underscoring the strength of the bond. However, it is important to note that Shokrian et al.'s work introduced an observation of stress transfer during shear testing, leading to distinct areas of failure due to the redistribution of forces within the overlap area as a result of adhesive joint debonding.

These differences between studies could be due to variations in adhesive formulations, test conditions, or characteristics of the adherends. This result emphasizes the complexity of adhesive behavior and the necessity to consider specific material properties and testing parameters in each study. Consequently, this failure mode influences the elongation of the SLJ subjected to tensile stresses.

4.2.4 Electromechanical testing of shear strength in single-lap joints with reinforced adhesives

The relationship between mechanical stress and electrical resistance of the adhesive joints is examined during the tensile test to assess the acceptability of manufactured samples for structural health monitoring and the effects of non-visible defects in the joints.

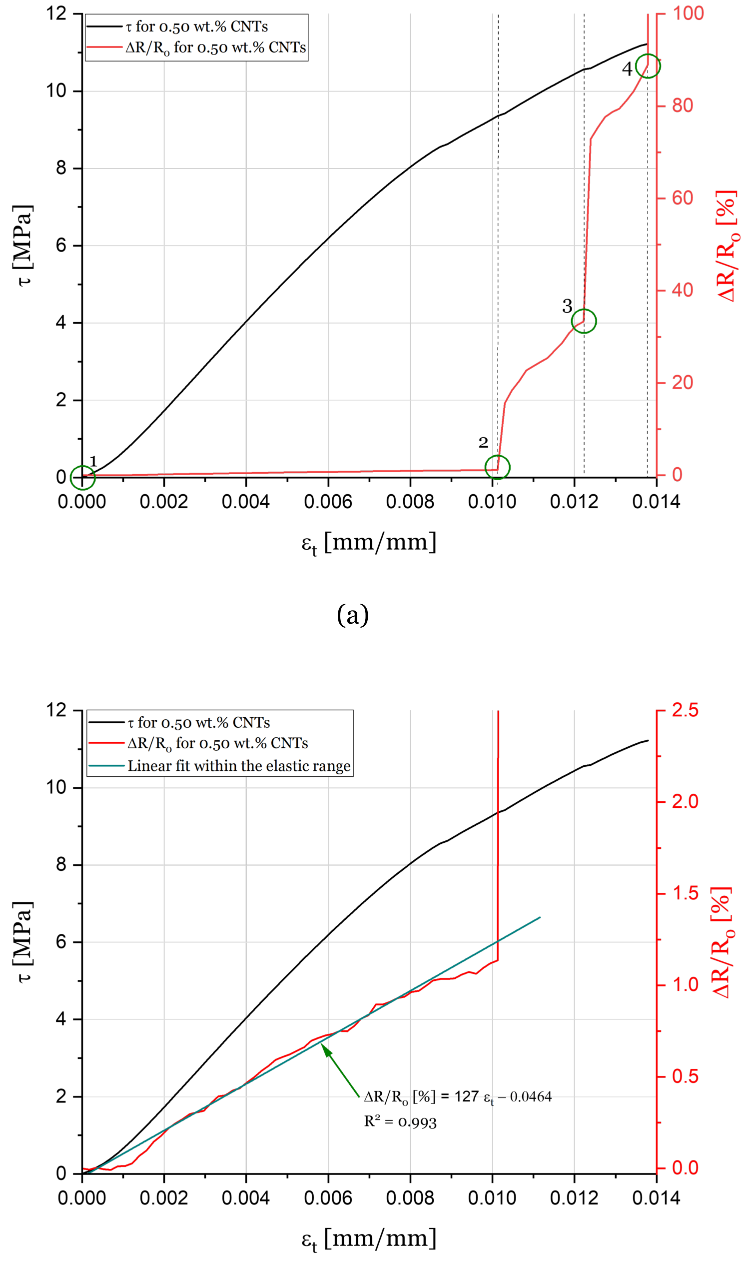

(a)

(b)

Figure 4.24: Average curve illustrating mechanical response and a representative normalized curve depicting the change in electrical resistance relative to shear stress until failure as a function of tensile strain for SLJ with an adhesive reinforced with 0.50 wt.% CNTs. (a) Complete curve. (b) Detail with a linear approximation for normalized electrical resistance curve.

The plot in Figure 4.24 shows mechanical and electrical measurements during a tensile stress test at a loading cell velocity of 1.3 mm/min until failure. The electrodes were connected to a multimeter for real-time electrical resistance measurements. The curve was normalized by calculating the electrical resistance ratio ($\Delta R/R_0$) for each second. Four distinct moments are identified, and Figure 4.24b details the first segment (1 to 2). The red line represents normalized electrical resistance, and the green line is a linear approximation within the tensile strain range of 0 mm/mm to 0.010 mm/mm. This linear behavior corresponds to the elastic range of the adhesive joint, with an elastic limit identified at a shear stress of 9.64 MPa and a tensile strain of 0.010 mm/mm. The piezoresistive curve shows a significant increase in electrical resistance within this stress and strain range, and to calculate the GF, the slope of the linear approximation, divided by a factor of 100 is used, since electrical resistance is in percentage in the displayed equation. The GF is 1.27 for a tensile strain until 0.010 mm/mm.

Returning to Figure 4.24a, three more changes in the slope are identified. The first is related to the transition between the elastic and plastic regime, while the others are associated with defects created in the adhesion area due to loading conditions. After the tensile strain of 0.010 mm/mm, the slope change in the electrical resistance plot is much more pronounced. Dashed lines are provided to correlate the electrical curve with the mechanical deformation. At a slightly higher tensile strain of 0.012 mm/mm, another peak in the electrical resistance plot indicates a crack in the adhesion system at a shear stress exceeding 10.6 MPa. The normalized electrical resistance varies between 72 % and 89 % in the final phase before complete failure, at which point the normalized electrical resistance becomes infinite. The lap shear strength was registered for a shear stress of 11.2 MPa.

The image frames were captured during the testing, and were synchronized with the corresponding events in the mechanical and electrical plots. These segments, as identified in Figure 4.24, correspond to sequential images displayed in Figure 4.25. Thanks to the alignment of frames and measurements on the same time scale, it is possible to accurately correlate all these cases, facilitating the visual inspection and analysis.

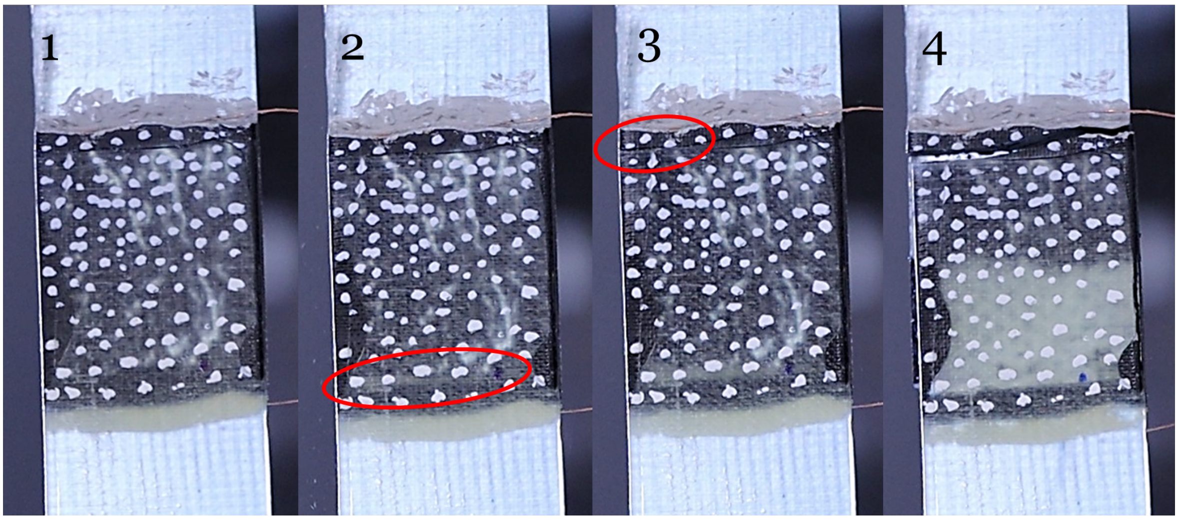

Figure 4.25: Sequential images of tensile stress testing leading to failure in a SLJ sample. These images correspond to the data points presented in Figure 4.24a. 1 - Initial undamaged sample; 2 - First failure point marked with a red circle within the overlap area; 3 - Second failure, with a visible crack; 4 - Ultimate failure.

In image 1 of Figure 4.25, the sample is undamaged and unloaded. Image 2, corresponding to point 2 in Figure 4.24a, represents a tensile load of 9.36 MPa. This moment, captured in the video, shows the formation of debonding zones highlighted by the red circle. It is responsible for the sudden change in electrical resistance from 1 % to a variation between 15 % and 35 %. This debonding occurs within the adhesive overlap.

Image 3 of Figure 4.25 corresponds to the third phase indicated in the preceding figure. The crack is more extensive and appears at the end of the overlap area in the fillet region (nanocomposite leakage outside the adhesion area). This structural damage resulted in a change in the normalized electrical resistance from 35 % to a range between 72 % and 89 %. After this point, the fourth image, 4, corresponds to the ultimate failure, where the adhesive joint experienced detachment between the glass fiber and epoxy adherends. Notably, before the complete separation of both adherends, the detachment process initiated from below and progressed until it reached the midpoint, at which the final fracture became inevitable.

For these sequential images, it is evident that, firstly, due to peel stresses, the adherend fixed in the universal machine experiences the initial fiber breakage. Following this occurrence, the loading stresses concentrate in the bonded area of the adhesive being pulled, and fiber breakage initiates on the other adherend surface.

These outcomes, coupled with the corresponding figures, facilitate clear monitoring of the joints with the functionalized adhesive. Mechanical properties are generally enhanced, primarily with the increased adhesive stiffness. Additionally, the adhesive gains sensing capabilities that enable structural monitoring.

Chapter 5

Conclusions

This chapter presents the conclusions of this work and is divided into two distinct sections. Section 5.1 shows the final remarks of this study and summarizes what was achieved. Section 5.2 gives an insight into the future work considering the remarks that were presented and the state-of-the-art.

5.1 Final remarks

This study aimed to enhance structural health monitoring in aerospace and aviation by exploring piezoresistive sensing in adhesive joints. The focus was on functionalizing epoxy adhesives with carbon nanotubes (CNTs) to develop a practical alternative to mechanical joining. This approach becomes crucial when using fiber composites, as mechanical joining introduces holes that degrades their mechanical properties. The research included a thorough review of adhesion concepts and piezoresistive phenomena to optimize epoxy-based adhesives filled with CNTs to improve sensitivity. The ultimate objective was to create a multifunctional material for glass fiber composites, enabling adhesive joints with self-sensing properties.

The investigation involved comparing two filler loading percentages in electromechanical tests on bulk adhesive samples undergoing bending tests. The electrical resistance variations were monitored using a two-probe method, and data on both mechanical and electrical resistance were collected at a rate of one measurement per second for effective correlation. Following optimization to strike a balance between sensing and mechanical reliability, the enhanced adhesive was applied in practical scenarios involving single-lap joints. These joints underwent bending tests for comparison with bulk adhesive joints. Additionally, tensile tests were conducted to assess the lap shear strength of the reinforced composite and its sensing capabilities under this loading condition.

The study concluded that a 0.5 wt.% filler loading exhibited superior electromechanical behavior, enhancing both the sensing capability and structural reliability of the adhesive compared to pure epoxy. In contrast, the electromechanical tests for 0.25 wt.% were less conclusive, with lower flexural strength than pure epoxy, indicating that the reinforcement at this loading may act as defects. The functionalized adhesive at 0.5 wt.% filler demonstrated the ability to identify both elastic and plastic regimes independently of test velocity and strain range, achieving a gauge factor (GF) of 5.2 in the elastic limit, surpassing that of metal strain gauges. In three-point bending tests for bulk-reinforced adhesive, the loading cell's velocity had a negligible impact on sensing properties, and the multifunctional adhesive exhibited a broad range of strains in which it could operate. Within the tested range of flexural strains (0 to 0.809 %), the gauge factor obtained was close to 2.

The adhesive effectively detected damages in practical applications, demonstrating capabilities for accurately identifying fixed loading conditions in flexural stress for adhesive joints. The GF for the elastic range was found to be 0.77, lower than that for bulk adhesive joints. Under tensile stress in single-lap joints, the functionalized adhesive efficiently detected abrupt damage and tracked damage accumulation through a gradual increase in resistance. For the elastic limit, the calculated GF was 1.27. Additionally, the primary failure mode for the joints was substrate failure, attributed to peel stresses within the adhesion area.

The correlation between strain and electrical resistance emphasizes the potential of multifunctional nanocomposites for structural health monitoring, particularly in single-lap joints. The study contributes valuable insights into the correlation between mechanical and conductive electrical networks, clearing the way for innovative applications. Despite promising results, there is a need for further studies on system reliability, durability, and lifecycle extension to comprehensively understand multifunctional adhesive systems.

In conclusion, the dissertation successfully achieved its objectives. The functionalization of epoxy adhesives proved effective in enhancing both mechanical and electrical properties, making it a multifunctional material. This functionalization made it possible to monitor adhesive joins under flexural and tensile loads in a real structure application. These findings showcase its potential in overcoming technological and engineering challenges, especially in advancing multifunctional nanocomposites with improved mechanical and sensing capabilities.

5.2 Future work

In light of the extensive research conducted in this dissertation, several opportunities for future studies have emerged to further explore multifunctional adhesives with piezoresistive sensing for aerospace applications. The following research directions are suggested:

- Optimization of filler dispersion: Optimize the manufacturing process of the adhesive for more effective dispersion. This may involve CNT functionalization, the use of dispersion solutions, or alternative mixing processes.

- Improvement of SLJ manufacturing method: Enhance the method for constructing single-lap joints to control the formation of fillets at the ends of the overlap length or achieve controlled fillets with desired dimensions.

- Optimization of electrodes: Optimize electrodes by using copper foil tape to prevent electrode breakage during mechanical tests, addressing brittleness issues with silver paint.

- Development of AC system with four probes: Design a system that operates with alternating current and utilizes four probes to enhance the accuracy and reliability of electrical characterization for multifunctional materials. This system should allow work within specific voltage ranges, thereby improving the sensitivity of the multifunctional material.

- Optimization of filler percentages: Further exploration of lower filler percentages to determine their proximity to the electrical percolation threshold.

- Cyclic loading in tensile stress: Extension of the study to investigate single-lap joints under cyclic loading in tensile stress, considering different strain ranges to evaluate piezoresistive sensing.

- Temperature influence study: Evaluation of the influence of temperature on sensing properties to understand the material's behavior under varying environmental conditions.

- Investigation of different nanocomposite functionalization: This involves trying out different combinations of carbon fillers alongside CNTs in the polymeric matrix to create diverse nanocomposite configurations. The aim could include experimenting with various functionalizations of CNTs in the composite material to improve electrical properties.

Recommendations for ongoing research efforts include comprehensive performance studies, system reliability assessments, and evaluations of durability and lifecycle extension. In conclusion, this dissertation has successfully achieved its goals, laying the groundwork for future advancements in multifunctional adhesive systems. The study highlights the significance of material science in developing innovative solutions for structural health monitoring, making valuable contributions to the broader fields of aerospace and aviation applications.

Bibliography

ASTM D3165-07 (2014), Test Method for Strength Properties of Adhesives in Shear by Tension Loading of Single-Lap-Joint Laminated Assemblies, a. ASTM International. doi: 10.1520/d3165-07r14. 70, 76

ASTM D5573-99 (2019), Practice for Classifying Failure Modes in Fiber-Reinforced-Plastic (FRP) Joints, b. ASTM International. doi: 10.1520/d5573-99r19. xiii, 28, 29

ASTM D638-14, Test Method for Tensile Properties of Plastics, c. ASTM International. doi: 10.1520/d0638-14. 77

ISO 178:2003, Plastics - Determination of flexural properties, 2003. ISO. 64, 73

Sustainable Development Goals: Goal 13 Climate Action. United Nations, 2022. URL `https://sdgs.un.org/goals/goal13`. Accessed on April 21, 2023. 1

S. Ahmed, T. Schumacher, J. McConnell, and E. T. Thostenson. Experimental and numerical investigation on the bond strength of self-sensing composite joints. *International Journal of Adhesion and Adhesives*, 84:227–237, aug 2018. doi: 10.1016/j.ijadhadh.2018.03.014. 23, 121

S. Akpinar and R. Sahin. The fracture load analysis of different material thickness in adhesively bonded joints subjected to fully reversed bending fatigue load. *Theoretical and Applied Fracture Mechanics*, 114:102984, aug 2021. doi: 10.1016/j.tafmec.2021.102984. 24, 26

Alamusi, N. Hu, H. Fukunaga, S. Atobe, Y. Liu, and J. Li. Piezoresistive Strain Sensors Made from Carbon Nanotubes Based Polymer Nanocomposites. *Sensors*, 11(11):10691–10723, nov 2011. doi: 10.3390/s111110691. 37

G. L. Anderson and D. J. Macon. 5 - Properties of adhesives. In Robert D. Adams, editor, *Adhesive Bonding (Second Edition)*, Woodhead Publishing Series in Welding and Other Joining Technologies, pages 133–155. Woodhead Publishing, second edition edition, 2021. ISBN 978-0-12-819954-1. doi: 10.1016/b978-0-12-819954-1.00002-2. 36

R. Aradhana, S. Mohanty, and S. K. Nayak. High performance epoxy nanocomposite adhesive: Effect of nanofillers on adhesive strength, curing and degradation kinetics. *International Journal of Adhesion and Adhesives*, 84:238–249, aug 2018. doi: 10.1016/j.ijadhadh.2018.03.013. 33, 34, 35

R. Aradhana, S. Mohanty, and S. K. Nayak. A review on epoxy-based electrically conductive adhesives. *International Journal of Adhesion and Adhesives*, 99:102596, jun 2020. doi:

10.1016/j.ijadhadh.2020.102596. 31, 32, 36

F. Avilés, A. I. O. Avilés, and M. C.-Puc. Piezoresistivity, Strain, and Damage Self-Sensing of Polymer Composites Filled with Carbon Nanostructures. *Advanced Engineering Materials*, 20(7):1701159, mar 2018. doi: 10.1002/adem.201701159. 7, 43, 46

M. R. Ayatollahi, S. Shadlou, M. M. Shokrieh, and M. Chitsazzadeh. Effect of multi-walled carbon nanotube aspect ratio on mechanical and electrical properties of epoxy-based nanocomposites. *Polymer Testing*, 30(5):548–556, aug 2011. doi: 10.1016/j.polymertesting.2011.04.008. 40

M. R. Ayatollahi, A. N. Giv, N. Razavi, and H. Khoramishad. Mechanical properties of adhesively single lap-bonded joints reinforced with multi-walled carbon nanotubes and silica nanoparticles. *The Journal of Adhesion*, 93(11):896–913, aug 2016. doi: 10.1080/00218464.2016.1187069. 33, 34, 120

J. B. Bai and A. Allaoui. Effect of the length and the aggregate size of MWNTs on the improvement efficiency of the mechanical and electrical properties of nanocomposites—experimental investigation. *Composites Part A: Applied Science and Manufacturing*, 34 (8):689–694, aug 2003. doi: 10.1016/s1359-835x(03)00140-4. 40

D. Balageas, C. P. Fritzen, and A. Güemes, editors. *Structural Health Monitoring*. Wiley, jan 2006. ISBN 9781905209019. doi: 10.1002/9780470612071. xiii, 6, 41, 42

M. D. Banea and L. F. M. da Silva. Adhesively bonded joints in composite materials: An overview. *Proceedings of the Institution of Mechanical Engineers, Part L: Journal of Materials: Design and Applications*, 223(1):1–18, jan 2009a. doi: 10.1243/14644207jmda219. xiii, xix, 5, 11, 13, 15, 16, 17, 18, 19, 25, 28, 61, 102, 121

M. D. Banea and L. F. M. da Silva. Mechanical Characterization of Flexible Adhesives. *The Journal of Adhesion*, 85(4-5):261–285, may 2009b. doi: 10.1080/00218460902881808. 22, 24, 26

N. G. C. Barbosa, R. D. S. G. Campilho, F. J. G. Silva, and R. D. F. Moreira. Comparison of different adhesively-bonded joint types for mechanical structures. *Applied Adhesion Science*, 6(1), dec 2018. doi: 10.1186/s40563-018-0116-1. 18, 19, 24

C. Barile, C. Casavola, V. Moramarco, C. Pappalettere, and P. K. Vimalathithan. Bonding Characteristics of Single- and Joggled-Lap CFRP Specimens: Mechanical and Acoustic Investigations. *Applied Sciences*, 10(5):1782, mar 2020. doi: 10.3390/app10051782. 19

W. Bauhofer and J. Z. Kovacs. A review and analysis of electrical percolation in carbon nanotube polymer composites. *Composites Science and Technology*, 69(10):1486–1498, aug 2009. doi: 10.1016/j.compscitech.2008.06.018. xix, 38, 39, 40

A. Bechikh, O. Klinkova, Y. Maalej, I. Tawfiq, and R. Nasri. Effect of dry abrasion treatments on composite surface quality and bonded joints shear strength. *International Journal of Adhesion and Adhesives*, 113:103058, mar 2022. doi: 10.1016/j.ijadhadh.2021.103058. 28

J. Bishopp. Chapter 5 Aerospace: A pioneer in structural adhesive bonding. In Philippe Cognard, editor, *Adhesives and Sealants*, volume 1 of *Handbook of Adhesives and Sealants*, pages 215–347. Elsevier Science Ltd, 2005. doi: 10.1016/S1874-5695(02)80006-9. xix, 4, 11, 13, 14

T. Bregar, D. An, S. Gharavian, M. Burda, I. D. Cardenas, V. K. Thakur, D. Ayre, M. Słoma, M. Hardiman, C. McCarthy, and H. Y. Nezhad. Carbon nanotube embedded adhesives for real-time monitoring of adhesion failure in high performance adhesively bonded joints. *Scientific Reports*, 10(1), oct 2020. doi: 10.1038/s41598-020-74076-y. xiii, xiv, 45, 47, 48, 50, 56, 57, 58, 70, 83, 86, 90, 106, 107, 110

S. Budhe, M. D. Banea, S. de Barros, and L. F. M. da Silva. An updated review of adhesively bonded joints in composite materials. *International Journal of Adhesion and Adhesives*, 72:30–42, jan 2017. doi: 10.1016/j.ijadhadh.2016.10.010. xiii, 19, 21, 25

S. Budhe, M. D. Banea, and S. de Barros. Bonded repair of composite structures in aerospace application: a review on environmental issues. *Applied Adhesion Science*, 6(1), aug 2018. doi: 10.1186/s40563-018-0104-5. 22

C-MAST. Centre for Mechanical and Aerospace Science and Technologies, 2023. URL `https://aerospace.ubi.pt/`. Accessed on December 28, 2023. v

J. V. Cardoso, P. V. Gamboa, and A. P. Silva. Effect of surface pre-treatment on the behaviour of adhesively-bonded CFRP T-joints. *Engineering Failure Analysis*, 104:1188–1202, October 2019. ISSN 1350-6307. doi: 10.1016/j.engfailanal.2019.05.043. 17, 27

H. M. Chong, S. J. Hinder, and A. C. Taylor. Graphene nanoplatelet-modified epoxy: effect of aspect ratio and surface functionality on mechanical properties and toughening mechanisms. *Journal of Materials Science*, 51(19):8764–8790, jul 2016. doi: 10.1007/s10853-016-0160-9. 34

D. D. L. Chung. 10 - Self-sensing structural composites in aerospace engineering. In S. Rana and R. Fangueiro, editors, *Advanced Composite Materials for Aerospace Engineering*, pages 295–331. Woodhead Publishing, 2016. ISBN 978-0-08-100939-0. doi: 10.1016/b978-0-08-100037-3.00010-9. 78

R. L. Crane, J. H. Smith, and J. Newman. Nondestructive inspection of adhesive bonded joints. In *Adhesive Bonding*, pages 215–256. Elsevier, 2021. doi: 10.1016/b978-0-12-819954-1.00008-3. 5

S. Cui, R. Canet, A. Derre, M. Couzi, and P. Delhaes. Characterization of multiwall carbon nanotubes and influence of surfactant in the nanocomposite processing. *Carbon*, 41(4): 797–809, 2003. doi: 10.1016/s0008-6223(02)00405-0. 40

L. F. M. da Silva, R. J. C. Carbas, G. W. Critchlow, M. A. V. Figueiredo, and K. Brown. Effect of material, geometry, surface treatment and environment on the shear strength of single lap joints. *International Journal of Adhesion and Adhesives*, 29(6):621–632, sep 2009. doi: 10.1016/j.ijadhadh.2009.02.012. 22, 23, 24, 26, 76, 119

L. F. M. da Silva, A. Öchsner, and R. D. Adams. *Introduction to Adhesive Bonding Technology*, pages 1–7. Springer Berlin Heidelberg, Berlin, Heidelberg, 2011. ISBN 978-3-642-01169-6. doi: 10.1007/978-3-642-01169-6_1. xiii, 13

O. S. Daliri, L.-M. Faller, M. Farahani, A. Roshanghias, A. Araee, M. Baniassadi, H. Oberlercher, and H. Zangl. Impedance analysis for condition monitoring of single lap CNT-epoxy adhesive joint. *International Journal of Adhesion and Adhesives*, 88:59–65, jan 2019. doi: 10.1016/j.ijadhadh.2018.11.003. 58

O. S. Daliri, M. Farahani, L. Faller, and H. Zangl. Structural health monitoring of defective single lap adhesive joints using graphene nanoplatelets. *Journal of Manufacturing Processes*, 55:119–130, jul 2020. doi: 10.1016/j.jmapro.2020.03.063. 58, 86, 102, 109, 120

P. Davies. 16 - Adhesive bonding of composites. In R. D. Adams, editor, *Adhesive Bonding (Second Edition)*, Woodhead Publishing Series in Welding and Other Joining Technologies, pages 499–524. Woodhead Publishing, second edition edition, 2021. ISBN 978-0-12-819954-1. doi: 10.1016/b978-0-12-819954-1.00007-1. 27

K. L. Devries and D. O. Adams. Mechanical testing of adhesive joints. In *Adhesion Science and Engineering*, pages 193–234. Elsevier, 2002. doi: 10.1016/b978-0-444-51140-9.50033-0. 18

S. M. Doshi, M. Coatney, M. Weiss, A. Chaudhari, D. H. Sung, E. T. Thostenson, and A. Hall. Characterizing the effect of transverse strain on carbon nanotube based sensing skins for structural health monitoring. In *SAMPE 2020 | Virtual Series*, volume 2020-June. The Society for the Advancement of Material and Process Engineering (SAMPE), 2020. doi: 10.33599/382/s.20.0011. 55, 110

D. Driver. Adhesive bonding for aerospace applications. In *High Performance*

Materials in Aerospace, pages 318–339. Springer Netherlands, 1995. doi: 10.1007/978-94-011-0685-6_11. xiii, 5, 11, 13, 14

L. Duan, D. R. D'hooge, and L. Cardon. Recent progress on flexible and stretchable piezoresistive strain sensors: From design to application. *Progress in Materials Science*, 114:100617, oct 2020. doi: 10.1016/j.pmatsci.2019.100617. 43, 46, 58, 84

S. Ebnesajjad. 8 - Characteristics of Adhesive Materials. In S. Ebnesajjad, editor, *Handbook of Adhesives and Surface Preparation*, Plastics Design Library, pages 137–183. William Andrew Publishing, Oxford, 2011. ISBN 978-1-4377-4461-3. doi: 10.1016/b978-1-4377-4461-3.10008-2. xix, 15, 16, 29

H. Ejaz, A. Mubashar, E. Uddin, Z. Ali, and N. Arif. Influence of MWCNTs on strength properties of high viscous epoxy adhesive and fracture behavior of adhesively bonded joints. *Theoretical and Applied Fracture Mechanics*, 120:103412, aug 2022. doi: 10.1016/j.tafmec.2022.103412. 4, 35, 82, 102, 103, 120, 122

L. M. Fernández-Cañadas, I. Ivañez, S. S. Saez, and E. J. Barbero. Effect of adhesive thickness and overlap on the behavior of composite single-lap joints. *Mechanics of Advanced Materials and Structures*, 28(11):1111–1120, jul 2019. doi: 10.1080/15376494.2019.1639086. 23, 24

G. Georgousis, C. Pandis, A. Kalamiotis, P. Georgiopoulos, A. Kyritsis, E. Kontou, P. Pissis, M. Micusik, K. Czanikova, J. Kulicek, and M. Omastova. Strain sensing in polymer/carbon nanotube composites by electrical resistance measurement. *Composites Part B: Engineering*, 68:162–169, jan 2015. doi: 10.1016/j.compositesb.2014.08.027. 44, 48, 53

V. Giurgiutiu. *Chapter 1. Introduction*, pages 1–23. Elsevier, December 2016. doi: 10.1016/b978-0-12-409605-9.00001-5. 1

G. Gkikas, D. Sioulas, A. Lekatou, N. M. Barkoula, and A. S. Paipetis. Enhanced bonded aircraft repair using nano-modified adhesives. *Materials Design*, 41:394–402, oct 2012. ISSN 0261-3069. doi: 10.1016/j.matdes.2012.04.052. 32

F. A. M. M. Gonçalves, M. Santos, T. Cernadas, P. Alves, and P. Ferreira. Influence of fillers on epoxy resins properties: a review. *Journal of Materials Science*, 57(32):15183–15212, aug 2022. doi: 10.1007/s10853-022-07573-2. xiii, 30, 31, 36

H. Gu, S. Tadakamalla, X. Zhang, Y. Huang, Y. Jiang, H. A. Colorado, Z. Luo, S. Wei, and Z. Guo. Epoxy resin nanosuspensions and reinforced nanocomposites from polyaniline stabilized multi-walled carbon nanotubes. *J. Mater. Chem. C*, 1(4):729–743, 2013. doi: 10.1039/c2tc00379a. 30, 36

L. J. Hart-Smith. *Adhesively Bonded Joints in Aircraft Structures*, pages 1101–1147. Springer Berlin Heidelberg, Berlin, Heidelberg, 2011. ISBN 978-3-642-01169-6. doi: 10.1007/978-3-642-01169-6_44. 12

N. Hu, Y. Karube, C. Yan, Z. Masuda, and H. Fukunaga. Tunneling effect in a polymer/carbon nanotube nanocomposite strain sensor. *Acta Materialia*, 56(13):2929–2936, aug 2008. doi: 10.1016/j.actamat.2008.02.030. xiv, 45, 52, 53, 54, 110

R. E. Hummel. *Electronic Properties of Materials*. Springer Berlin Heidelberg, 1993. ISBN 9783662029541. doi: 10.1007/978-3-662-02954-1. 84

M. S. Irfan, T. Khan, T. Hussain, K. Liao, and R. Umer. Carbon coated piezoresistive fiber sensors: From process monitoring to structural health monitoring of composites – A review. *Composites Part A: Applied Science and Manufacturing*, 141:106236, feb 2021. doi: 10.1016/j.compositesa.2020.106236. 1, 46

M. B. Jakubinek, B. Ashrafi, Y. Zhang, Y. M. Rubi, C. T. Kingston, A. Johnston, and B. Simard. Single-walled carbon nanotube–epoxy composites for structural and conductive aerospace adhesives. *Composites Part B: Engineering*, 69:87–93, feb 2015. doi: 10.1016/j.compositesb.2014.09.022. 122

R. E. Jensen, D. C. DeSchepper, and D. P. Flanagan. Multivariate analysis of high throughput adhesively bonded single lap joints. *International Journal of Adhesion and Adhesives*, 89:1–10, mar 2019. doi: 10.1016/j.ijadhadh.2018.11.004. 23

P. Jojibabu, M. Jagannatham, P. Haridoss, G. D. J. Ram, A. P. Deshpande, and S. R. Bakshi. Effect of different carbon nano-fillers on rheological properties and lap shear strength of epoxy adhesive joints. *Composites Part A: Applied Science and Manufacturing*, 82:53–64, mar 2016. doi: 10.1016/j.compositesa.2015.12.003. 33, 34, 120, 122

I. Kang, M. J. Schulz, J. H. Kim, V. Shanov, and D. Shi. A carbon nanotube strain sensor for structural health monitoring. *Smart Materials and Structures*, 15(3):737–748, apr 2006. doi: 10.1088/0964-1726/15/3/009. 42

T. Khan, M. S. Irfan, M. Ali, Y. Dong, S. Ramakrishna, and R. Umer. Insights to low electrical percolation thresholds of carbon-based polypropylene nanocomposites. *Carbon*, 176: 602–631, may 2021. doi: 10.1016/j.carbon.2021.01.158. xiii, xix, 31, 37, 38, 41

K. Kim, J. Yoo, Y. Yi, and C. Kim. Failure mode and strength of uni-directional composite single lap bonded joints with different bonding methods. *Composite Structures*, 72(4): 477–485, apr 2006. doi: 10.1016/j.compstruct.2005.01.023. 20, 22, 26

A. J. Kinloch. Introduction. In *Adhesion and Adhesives*, pages 1–17. Springer Netherlands,

1987. doi: 10.1007/978-94-015-7764-9_1. 13

M. Konstantakopoulou and G. Kotsikos. Effect of MWCNT filled epoxy adhesives on the quality of adhesively bonded joints. *Plastics, Rubber and Composites*, 45(4):166–172, apr 2016. doi: 10.1080/14658011.2016.1165788. 84, 122

J. Z. Kovacs, B. S. Velagala, K. Schulte, and W. Bauhofer. Two percolation thresholds in carbon nanotube epoxy composites. *Composites Science and Technology*, 67(5):922–928, apr 2007. doi: 10.1016/j.compscitech.2006.02.037. 40

J. Li, P. C. Ma, W. S. Chow, C. K. To, B. Z. Tang, and J.-K. Kim. Correlations between Percolation Threshold, Dispersion State, and Aspect Ratio of Carbon Nanotubes. *Advanced Functional Materials*, 17(16):3207–3215, sep 2007. doi: 10.1002/adfm.200700065. 40

J. Li, Y. Yan, T. Zhang, and Z. Liang. Experimental study of adhesively bonded CFRP joints subjected to tensile loads. *International Journal of Adhesion and Adhesives*, 57:95–104, mar 2015. doi: 10.1016/j.ijadhadh.2014.11.001. 24

A. S. Lim, Z. R. Melrose, E. T. Thostenson, and T.-W. Chou. Damage sensing of adhesively-bonded hybrid composite/steel joints using carbon nanotubes. *Composites Science and Technology*, 71(9):1183–1189, jun 2011. doi: 10.1016/j.compscitech.2010.10.009. 47, 48, 56, 87, 90, 102, 120

S. Liu, V. S. Chevali, Z. Xu, D. Hui, and H. Wang. A review of extending performance of epoxy resins using carbon nanomaterials. *Composites Part B: Engineering*, 136:197–214, mar 2018. ISSN 1359-8368. doi: 10.1016/j.compositesb.2017.08.020. xix, 30, 31

S. Luo, W. Obitayo, and T. Liu. SWCNT-thin-film-enabled fiber sensors for lifelong structural health monitoring of polymeric composites - From manufacturing to utilization to failure. *Carbon*, 76:321–329, sep 2014. doi: 10.1016/j.carbon.2014.04.083. xiv, 54, 55

R. Mactabi, I. D. Rosca, and S. V. Hoa. Monitoring the integrity of adhesive joints during fatigue loading using carbon nanotubes. *Composites Science and Technology*, 78:1–9, apr 2013. doi: 10.1016/j.compscitech.2013.01.020. 115

D. N. Markatos, K. I. Tserpes, E. Rau, S. Markus, B. Ehrhart, and S. Pantelakis. The effects of manufacturing-induced and in-service related bonding quality reduction on the mode-I fracture toughness of composite bonded joints for aeronautical use. *Composites Part B: Engineering*, 45(1):556–564, feb 2013. doi: 10.1016/j.compositesb.2012.05.052. 4, 12, 13

C. A. Martin, J. K. W. Sandler, M. S. P. Shaffer, M.-K. Schwarz, W. Bauhofer, K. Schulte, and A. H. Windle. Formation of percolating networks in multi-wall carbon-nanotube–

epoxy composites. *Composites Science and Technology*, 64(15):2309–2316, nov 2004. doi: 10.1016/j.compscitech.2004.01.025. 40

M. May, H. M. Wang, and R. Akid. Effects of the addition of inorganic nanoparticles on the adhesive strength of a hybrid sol–gel epoxy system. *International Journal of Adhesion and Adhesives*, 30(6):505–512, sep 2010. doi: 10.1016/j.ijadhadh.2010.05.002. 32

J. Mohan, A. Ivanković, and N. Murphy. Mode I fracture toughness of co-cured and secondary bonded composite joints. *International Journal of Adhesion and Adhesives*, 51:13–22, jun 2014. doi: 10.1016/j.ijadhadh.2014.02.008. 22

J. Mohan, A. Ivanković, and N. Murphy. Mixed-mode fracture toughness of co-cured and secondary bonded composite joints. *Engineering Fracture Mechanics*, 134:148–167, jan 2015. doi: 10.1016/j.engfracmech.2014.12.005. 22

R. Moriche, M. Sánchez, S. G. Prolongo, A. J. Suárez, and A. Ureña. Reversible phenomena and failure localization in self-monitoring GNP/epoxy nanocomposites. *Composite Structures*, 136:101–105, feb 2016. doi: 10.1016/j.compstruct.2015.10.006. 90, 94

R. Moriche, A. J. Suárez, M. Sánchez, S. G. Prolongo, and A. Ureña. Sensitivity, influence of the strain rate and reversibility of GNPs based multiscale composite materials for high sensitive strain sensors. *Composites Science and Technology*, 155:100–107, feb 2018. doi: 10.1016/j.compscitech.2017.12.002. 65

C.-W. Nan, Y. Shen, and J. Ma. Physical Properties of Composites Near Percolation. *Annual Review of Materials Research*, 40(1):131–151, jun 2010. doi: 10.1146/annurev-matsci-070909-104529. 38

NANOCYL®. Technical Data Sheet: NC7000™ Multiwall carbon nanotubes. 2016. xiv, xix, 62

S. Nauman. Piezoresistive Sensing Approaches for Structural Health Monitoring of Polymer Composites—A Review. *Eng*, 2(2):197–226, may 2021. ISSN 2673-4117. doi: 10.3390/eng2020013. 42

W. Obitayo and T. Liu. A Review: Carbon Nanotube-Based Piezoresistive Strain Sensors. *Journal of Sensors*, 2012:1–15, 2012. doi: 10.1155/2012/652438. 39, 44

S. Omairey, N. Jayasree, and M. Kazilas. Defects and uncertainties of adhesively bonded composite joints. *SN Applied Sciences*, 3(9):769, aug 2021. doi: 10.1007/s42452-021-04753-8. xiii, xix, 3, 12, 13, 14, 23

A. Ozel, B. Yazici, S. Akpinar, M. D. Aydin, and Ş. Temiz. A study on the strength of adhesively bonded joints with different adherends. *Composites Part B: Engineering*, 62:167–174, 2014. ISSN 1359-8368. doi: 10.1016/j.compositesb.2014.03.001. 24, 25, 26, 69

S. Pantelakis. *Historical Development of Aeronautical Materials*, pages 1–19. Springer International Publishing, March 2020. ISBN 978-3-030-35345-2. doi: 10.1007/978-3-030-35346-9_1. 12

Y.-B. Park, M.-G. Song, J.-J. Kim, J.-H. Kweon, and J.-H. Choi. Strength of carbon/epoxy composite single-lap bonded joints in various environmental conditions. *Composite Structures*, 92(9):2173–2180, aug 2010. doi: 10.1016/j.compstruct.2009.09.009. 21

C. L. Pérez, J. V. C. Rodríguez, and F. Avilés. Influence of rigid segment and carbon nanotube concentration on the cyclic piezoresistive and hysteretic behavior of multiwall carbon nanotube/segmented polyurethane composites. *Composites Science and Technology*, 128: 25–32, may 2016. doi: 10.1016/j.compscitech.2016.03.010. 89, 91, 94, 110, 111, 113, 115

X. P. Qing, H.-L. Chan, S. J. Beard, and A. Kumar. An Active Diagnostic System for Structural Health Monitoring of Rocket Engines. *Journal of Intelligent Material Systems and Structures*, 17(7):619–628, jul 2006. doi: 10.1177/1045389x06059956. 42

J. R. B. Quijano, F. Avilés, J. O. Aguilar, and A. Tapia. Strain sensing capabilities of a piezoresistive MWCNT-polysulfone film. *Sensors and Actuators A: Physical*, 159(2):135–140, may 2010. doi: 10.1016/j.sna.2010.03.005. 94

S. Rana and R. Fangueiro. Advanced composites in aerospace engineering. In *Advanced Composite Materials for Aerospace Engineering*, pages 1–15. Elsevier, 2016. doi: 10.1016/b978-0-08-100037-3.00001-8. 41, 44

S. N. A. Razak and A. R. Othman. A Review on the Performance of Adhesive Bonding in Polymer Composite Joints. volume 471 of *Key Engineering Materials*, pages 610–615. Trans Tech Publications Ltd, June 2011. doi: 10.4028/www.scientific.net/kem.471-472.610. 12

S. M. J. Razavi, M. R. Ayatollahi, A. N. Giv, and H. Khoramishad. Single lap joints bonded with structural adhesives reinforced with a mixture of silica nanoparticles and multi walled carbon nanotubes. *International Journal of Adhesion and Adhesives*, 80:76–86, jan 2018. doi: 10.1016/j.ijadhadh.2017.10.007. 120, 122

Rebelco. Ficha Técnica -Tecido de Vidro. xix, 63

H. Rocha, C. Semprimoschnig, and J. P. Nunes. Sensors for process and structural health monitoring of aerospace composites: A review. *Engineering Structures*, 237:112231, jun 2021. doi: 10.1016/j.engstruct.2021.112231. 43

X. F. S. Romate, A. J. Suárez, J. Molinero, M. Sánchez, A. Güemes, and A. Ureña. Development of bonded joints using novel CNT doped adhesive films: Mechanical and electrical properties. *International Journal of Adhesion and Adhesives*, 86:98–104, nov 2018. doi: 10.1016/j.ijadhadh.2018.09.001. 34, 119, 121, 122

RS Pro. Silver Conductive RS 186-3600. URL `https://int.rsdelivers.com/product/rs-pro/rs-pro-conductive-lacquer/1863600`. xiv, 68

R. Sahin and S. Akpinar. The effects of adherend thickness on the fatigue strength of adhesively bonded single-lap joints. *International Journal of Adhesion and Adhesives*, 107:102845, jun 2021. doi: 10.1016/j.ijadhadh.2021.102845. 23

E. Sancaktar and L. Bai. Electrically Conductive Epoxy Adhesives. *Polymers*, 3(1):427–466, feb 2011. doi: 10.3390/polym3010427. 36

J. Sandler, M. S. P. Shaffer, T. Prasse, W. Bauhofer, K. Schulte, and A. H. Windle. Development of a dispersion process for carbon nanotubes in an epoxy matrix and the resulting electrical properties. *Polymer*, 40(21):5967–5971, oct 1999. doi: 10.1016/s0032-3861(99)00166-4. 40

A. Sanli, C. Müller, O. Kanoun, C. Elibol, and M. F.-X. Wagner. Piezoresistive characterization of multi-walled carbon nanotube-epoxy based flexible strain sensitive films by impedance spectroscopy. *Composites Science and Technology*, 122:18–26, January 2016. ISSN 0266-3538. doi: 10.1016/j.compscitech.2015.11.012. 53

A. Sanli, A. Benchirouf, C. Müller, and O. Kanoun. Piezoresistive performance characterization of strain sensitive multi-walled carbon nanotube-epoxy nanocomposites. *Sensors and Actuators A: Physical*, 254:61–68, feb 2017. doi: 10.1016/j.sna.2016.12.011. 53, 94, 99, 115

A. Santamaria, M. E. Muñoz, M. Fernández, and M. Landa. Electrically conductive adhesives with a focus on adhesives that contain carbon nanotubes. *Journal of Applied Polymer Science*, 129(4):1643–1652, mar 2013. doi: 10.1002/app.39137. 32, 36

R. Di Sante. Fibre Optic Sensors for Structural Health Monitoring of Aircraft Composite Structures: Recent Advances and Applications. *Sensors*, 15(8):18666–18713, jul 2015. doi: 10.3390/s150818666. xiii, 2

P. Santos, A. Maceiras, and P. N. B. Reis. Influence of manufacturing parameters on the mechanical properties of nano-reinforced CFRP by carbon nanofibers. *IOP Conference Series: Materials Science and Engineering*, 1126(1):012012, mar 2021. doi: 10.1088/1757-899x/1126/1/012012. 63, 64

P. Santos, A. P. Silva, and P. N. B. Reis. Effect of Carbon Nanofibers on the Viscoelastic Response of Epoxy Resins. *Polymers*, 15(4):821, feb 2023. doi: 10.3390/polym15040821. 63, 64, 84

W. Seneviratne, J. Tomblin, and M. Kittur. Durability and residual strength of adhesively-bonded composite joints. In *Fatigue and Fracture of Adhesively-Bonded Composite Joints*, pages 289–320. Elsevier, 2015. doi: 10.1016/b978-0-85709-806-1.00010-0. xiii, 5

M. Shishesaz and M. Hosseini. Effects of joint geometry and material on stress distribution, strength and failure of bonded composite joints: an overview. *The Journal of Adhesion*, 96(12):1053–1121, dec 2018. doi: 10.1080/00218464.2018.1554483. xiii, 17, 18

M. D. Shokrian, K. S. Nezhad, and R. Najjar. Effect of CNT dispersion methods on the strength and fracture mechanism of interface in epoxy adhesive/Al joints. *Journal of Adhesion Science and Technology*, 33(13):1394–1409, apr 2019. doi: 10.1080/01694243.2019.1595304. 35, 120, 121, 122

Epoxy Systems Sicomin. SR 8100 / SD 882X Infusion System. 2019. xix, 61, 63

C. H. Simmons, D. E. Maguire, and N. Phelps. *Engineering adhesives*, pages 547–560. Elsevier, January 2020. ISBN 9780128184820. doi: 10.1016/b978-0-12-818482-0.00036-0. 23

J. H. Smith. 23 - Aerospace industry applications of adhesive bonding. In R. D. Adams, editor, *Adhesive Bonding (Second Edition)*, Woodhead Publishing Series in Welding and Other Joining Technologies, pages 763–800. Woodhead Publishing, second edition edition, 2021. ISBN 978-0-12-819954-1. doi: 10.1016/b978-0-12-819954-1.00001-0. 15

M. G. Song, J. H. Kweon, J. H. Choi, J. H. Byun, M. H. Song, S. J. Shin, and T. J. Lee. Effect of manufacturing methods on the shear strength of composite single-lap bonded joints. *Composite Structures*, 92(9):2194–2202, aug 2010. doi: 10.1016/j.compstruct.2009.08.041. 13, 20, 21, 26, 69

L. Sorrentino, W. Polini, C. Bellini, and G. Parodo. Surface treatment of CFRP: influence on single lap joint performances. *International Journal of Adhesion and Adhesives*, 85: 225–233, oct 2018. doi: 10.1016/j.ijadhadh.2018.06.008. 25, 27

G. Spinelli, P. Lamberti, V. Tucci, L. Vertuccio, and L. Guadagno. Experimental and theoretical study on piezoresistive properties of a structural resin reinforced with carbon nanotubes for strain sensing and damage monitoring. *Composites Part B: Engineering*, 145:90–99, jul 2018. doi: 10.1016/j.compositesb.2018.03.025. 47, 48, 51, 90

G. Spinelli, P. Lamberti, V. Tucci, L. Guadagno, and L. Vertuccio. Damage Monitoring of Structural Resins Loaded with Carbon Fillers: Experimental and Theoretical Study. *Nanomaterials*, 10(3):434, feb 2020. doi: 10.3390/nano10030434. xiv, 38, 42, 45, 46, 50, 51, 67, 90, 95, 110

F. Taheri. *Improvement of the Performance of Structural Adhesive Joints with Nanoparticles and Numerical Prediction of Their Response*, pages 35–78. Wiley, August 2020. ISBN 9781119737322. doi: 10.1002/9781119737322.ch2. 29

R. Taherian. Development of an Equation to Model Electrical Conductivity of Polymer-Based Carbon Nanocomposites. *ECS Journal of Solid State Science and Technology*, 3(6):M26, May 2014. doi: 10.1149/2.023406jss. xiii, 37, 38

A. A. Taib, R. Boukhili, S. Achiou, S. Gordon, and H. Boukehili. Bonded joints with composite adherends. Part I. Effect of specimen configuration, adhesive thickness, spew fillet and adherend stiffness on fracture. *International Journal of Adhesion and Adhesives*, 26(4): 226–236, 2006. ISSN 0143-7496. doi: 10.1016/j.ijadhadh.2005.03.015. 3, 20, 29

E. T. Thostenson and T.-W. Chou. Carbon Nanotube Networks: Sensing of Distributed Strain and Damage for Life Prediction and Self Healing. *Advanced Materials*, 18(21):2837–2841, nov 2006. doi: 10.1002/adma.200600977. xiii, 7

K. Tserpes. Adhesive Bonding of Aircraft Structures. In *Revolutionizing Aircraft Materials and Processes*, pages 337–357. Springer International Publishing, 2020. doi: 10.1007/978-3-030-35346-9_12. xix, 4, 14, 15, 16

L. Vertuccio, L. Guadagno, G. Spinelli, P. Lamberti, V. Tucci, and S. Russo. Piezoresistive properties of resin reinforced with carbon nanotubes for health-monitoring of aircraft primary structures. *Composites Part B: Engineering*, 107:192–202, dec 2016. doi: 10.1016/j.compositesb.2016.09.061. xiv, 8, 38, 42, 45, 46, 49, 50, 65, 90, 106

D. Wang and D. D. L. Chung. Through-thickness piezoresistivity in a carbon fiber polymer-matrix structural composite for electrical-resistance-based through-thickness strain sensing. *Carbon*, 60:129–138, aug 2013. doi: 10.1016/j.carbon.2013.04.005. 39

S. Wang and D. D. L. Chung. Self-sensing of flexural strain and damage in carbon fiber polymer-matrix composite by electrical resistance measurement. *Carbon*, 44(13):2739–2751, nov 2006. doi: 10.1016/j.carbon.2006.03.034. 42, 43, 47, 48, 49

Y. Wang, Y. Wang, B. Wan, B. Han, G. Cai, and Z. Li. Properties and mechanisms of self-sensing carbon nanofibers/epoxy composites for structural health monitoring. *Composite Structures*, 200:669–678, sep 2018. doi: 10.1016/j.compstruct.2018.05.151. 47

J. M. Wernik and S. A. Meguid. On the mechanical characterization of carbon nanotube reinforced epoxy adhesives. *Materials Design*, 59:19–32, jul 2014. ISSN 0261-3069. doi: 10.1016/j.matdes.2014.02.034. 32, 33, 34, 35

G. Yang, T. Yang, W. Yuan, and Y. Du. The influence of surface treatment on the tensile properties of carbon fiber-reinforced epoxy composites-bonded joints. *Composites Part B: Engineering*, 160:446–456, mar 2019. doi: 10.1016/j.compositesb.2018.12.095. 28

S. Yang and N. Lu. Gauge Factor and Stretchability of Silicon-on-Polymer Strain Gauges. *Sensors*, 13(7):8577–8594, jul 2013. doi: 10.3390/s130708577. 97

X. Yao, C. Luan, D. Zhang, L. Lan, and J. Fu. Evaluation of carbon fiber-embedded 3D printed structures for strengthening and structural-health monitoring. *Materials &amp Design*, 114:424–432, jan 2017. doi: 10.1016/j.matdes.2016.10.078. xiv, 52, 85, 86, 107

T. Yusaf, L. Fernandes, A. R. A. Talib, Y. S. M. Altarazi, W. Alrefae, K. Kadirgama, D. Ramasamy, A. Jayasuriya, G. Brown, R. Mamat, H. Al Dhahad, F. Benedict, and M. Laimon. Sustainable Aviation—Hydrogen Is the Future. *Sustainability*, 14(1):548, jan 2022. doi: 10.3390/su14010548. 1

Y. Zhao and E. V. Barrera. Asymmmetric Diamino Functionalization of Nanotubes Assisted by BOC Protection and Their Epoxy Nanocomposites. *Advanced Functional Materials*, 20 (18):3039–3044, sep 2010. doi: 10.1002/adfm.201000942. 31

W. Zielecki, A. Kubit, T. Trzepieciński, U. Narkiewicz, and Z. Czech. Impact of multiwall carbon nanotubes on the fatigue strength of adhesive joints. *International Journal of Adhesion and Adhesives*, 73:16–21, mar 2017. doi: 10.1016/j.ijadhadh.2016.11.005. 34